Physisorption and ortho-para conversion of molecular hydrogen on solid surfaces

K. Fukutani, T. Sugimoto

[a]*Institute of Industrial Science, The University of Tokyo, Komaba, Meguro-ku, Tokyo 153-8505, Japan*
[b]*Department of Chemistry, School of Science, Kyoto University, Oiwake-cho, Sakyo-ku, Kyoto 606-8502, Japan*

Abstract

Molecular hydrogen exists in nuclear-spin isomers of ortho and para species according to the total nuclear spin. These species are correlated to the rotational states with even and odd rotational quantum numbers because of the symmetry of the total wavefunction with respect to the permutation of the two nuclei. Although interconversion between the ortho and para states is slow in an isolated state, the conversion is promoted in a physisorption state via interaction with surfaces of not only magnetic but also diamagnetic materials. In a physisorption state, the rotational motion of hydrogen molecules is modified due to the potential anisotropy. The physisorption properties and interconversion rate of the ortho and para hydrogen have recently been investigated on well-defined surfaces, which allow detailed comparison with theory. Furthermore, relative abundance of the ortho and para hydrogen in astronomical circumstances has been reported in recent years, which often shows a value out of equilibrium with the environment temperature. Physisorption and ortho-para conversion on the surfaces of interstellar media are expected to enable deeper understanding of astronomical phenomena. In this article, we review recent progress of experimental and theoretical studies on the physisorption and ortho-para conversion of molecular hydrogen and its relevance to the recent astronomical observation.

Keywords: Molecular hydrogen, ortho-para conversion, physisorption

Email addresses: fukutani@iis.u-tokyo.ac.jp (K. Fukutani), toshiki@kuchem.kyoto-u.ac.jp (T. Sugimoto)

1. Introduction

Hydrogen is the most abundant element in the universe, and ubiquitous in our society. While atomic hydrogen is chemically reactive because of the unpaired electron, molecular hydrogen is rather inert due to its closed shell nature. A remarkable feature of molecular hydrogen is that it is classified into nuclear-spin isomers designated as ortho and para species according to the total nuclear spin [1, 2, 3]. The nuclear spins of proton and deuteron are 1/2 and 1, respectively. Since the indistinguishability of identical nuclei dictates that the total wave function be antisymmetric or symmetric with respect to the exchange of the two nuclei depending on their spins, the ortho and para species are correlated with the rotational states with odd and even quantum numbers. This was first pointed out theoretically [4, 5, 6] and confirmed experimentally in late 1920's [7, 8]. Presence of nuclear-spin isomers is manifestation of the quantum mechanics, and therefore has gained much attention in both physics and chemistry.

In an isolated state, the transition between the ortho and para species is strictly forbidden, the theoretical time scale being 10^{20} s, which is longer than the age of the universe. Interaction with other substances, however, brings about a perturbation, which promotes the conversion between the ortho and para species. The ortho-para (o-p) conversion is, on one hand, of fundamental interest because it includes nuclear-spin flip and rotational-state transition, on the other hand technologically important in hydrogen liquefaction. Hydrogen is an efficient energy source as used in fuel cells and rocket fuel, and storing hydrogen in a liquid form is a high-density storage method. When normal hydrogen with the o-p ratio of 3 is liquefied, about 40 % of the originally stored hydrogen evaporates within 100 h because of rotational-energy release originating from the o-p conversion slowly occurring in liquid hydrogen [9]. This boil-off problem is circumvented with a use of proper catalysts such as iron hydroxides and chromium oxides that enhance o-p conversion during liquefaction and allow for storing hydrogen in the para form.

When molecular hydrogen interacts with solid surfaces, the molecule is adsorbed on surfaces either molecularly or dissociatively. While the molecular adsorption occurs through the van der Waals interaction and electric multipole interaction induced by the surface electric field, which is referred to as physisorption, dissociative adsorption is realized via orbital hybridization, which is called chemisorption. The o-p conversion occurs via both

schemes of adsorption: Once H_2 is dissociatively chemisorbed on a solid surface and associatively desorbs from the surface, the relative nuclear-spin direction can be changed implying interchange between the ortho and para states. In a physisorption state, on the other hand, the o-p transition is promoted through magnetic interaction with surfaces. The former mechanism is sometimes referred to as a chemical process, while the latter is called a physical process. Since the adsorption energy for physisorption and chemisorption is typically around 30 meV and 1 eV, respectively, the physical and chemical mechanisms are important at low and high temperatures, respectively. In the present review, we focus on the physical o-p conversion process, in particular the progress made after the previous review article by Ilisca [10].

In the physical conversion, the first step is physisorption in the potential well. Important factors include the sticking probability and residence time on the surface. It is noted that the energy scale of the physisorption is similar to that of the rotational motion of hydrogen molecules. Since the rotational energy of hydrogen molecules is relatively large compared with those of heavier molecules, the rotational motion is retained in the physisorption as recognized as the quantum rotor. Upon physisorption, furthermore, the rotational levels are modified by the anisotropic potential. Since the rotational states are different between the ortho and para species, the transition between the two species is accompanied by rotational-energy dissipation or excitation. In this regard, the energy level in both the center of mass motion and rotational motion is of importance for the physical o-p conversion. The physisorption properties of hydrogen molecules are described in Sec. 2.2.

The second point in the physical conversion is the nuclear-spin flip that changes the nuclear-spin multiplicity of hydrogen molecules. This requires a perturbation that includes magnetic interaction. The magnetic interaction originates from either the spin or orbital motion of electrons and nuclei. The fundamental concept of the nuclear-spin flip is described in Sec. 3.2.

From the experimental point of view, how to probe the nuclear spin of hydrogen and distinguish the ortho and para species was not a trivial problem. Since the ortho and para hydrogen has different rotational energies, two experimental approaches are to measure the nuclear-spin state directly and probe the rotational state. The former is nuclear magnetic resonance, and the latter includes the thermal-conductivity measurement originating from the specific-heat difference of the ortho and para species and the rotational spectroscopy using light, neutrons and electrons, which is reviewed in Sec. 4.

Since the discovery of the ortho and para species of molecular hydro-

gen, the adsorption properties and interconversion of ortho and para hydrogen were thoroughly investigated on a variety of surfaces by employing the thermal-conductivity measurement. Whereas the physisorption energy of the ortho and para hydrogen was found to be different [11, 12, 13], the o-p conversion rate was measured on surfaces of magnetic materials including magnetically dilute and dense systems in 1950's – 1960's, which are reviewed in [10]. The o-p conversion process was interpreted on the basis of the Wigner model where the inhomogeneous magnetic field on magnetic surfaces induces the nuclear-spin flip as shown in Sec. 3.2. The o-p conversion rate was furthermore found to be appreciably affected by external magnetic fields and magnetic phase transition, which also acquired much attention [14, 15, 16]. Although basic understanding of the o-p conversion was developed and many interesting findings were reported in this period, molecular-level understanding was not satisfactory mainly because most of the experiments were performed for powder and porous samples, of which surfaces were neither well-defined nor well-characterized. It should be pointed out that most metal surfaces are readily oxidized with O_2 and/or H_2O even though the experiments were intended on clean metal surfaces, and that oxide surfaces might be partially reduced as a result of interaction with hydrogen even if oxide surfaces were initially prepared.

In early 1980's, new experimental results suggesting o-p conversion on diamagnetic metals were reported using sophisticated electron energy loss spectroscopy (EELS) experiments [17, 18, 19, 20]. This was actually the beginning of a new era for hydrogen o-p conversion studies, in that the experiments were performed on well-defined single-crystal surfaces in an ultra-high vacuum (UHV) condition. Stimulated by these papers, theoretical efforts were made [21], and a new conversion model was constructed [22]. The progress in this period as well as historical survey is given in a comprehensive review by Ilisca [10].

Along with this theoretical advance, the effects of molecular orientation on the o-p conversion were theoretically investigated in detail, and a new proposal to control the conversion was presented [23]. While the theory provides a solid basis for the o-p conversion on metal surfaces, experimental data were not satisfactory because of the difficulty to detect the spin state of hydrogen molecules on well-defined solid surfaces. In 2000's, a new experimental technique probing the ortho and para hydrogen on surfaces was developed by combining the resonance-enhanced multiphoton ionization (REMPI) with desorption techniques [24, 25, 26]. With this technique, the adsorption prop-

erties of ortho and para hydrogen and the o-p conversion time have been measured on solid surfaces.

In recent years, the o-p ratio of molecular hydrogen in space and planetary environments has been experimentally observed, which has acquired much attention and is believed to provide us with information on astrochemistry, astrophysics and planetary science [27, 28, 29, 30, 31, 32]. In astrochemistry, possible o-p conversion on surfaces of interstellar media is of considerable interest and importance. In this regard, the o-p conversion has been investigated on ice surfaces, which are dominant interstellar media, in laboratory experiments, and a new conversion model has been proposed [33]. Related to this o-p conversion work, the o-p ratio upon H_2 formation on surfaces has been investigated both experimentally and theoretically, which are described in Sec. 6 along with recent astronomical observation results. In view of the current status of the hydrogen o-p conversion on well-defined solid surfaces, recent progress in this field is reviewed in this article.

2. Fundamental features of molecular hydrogen

2.1. Electronic, rotational, and nuclear-spin states: classification into nuclear-spin isomers

Molecular hydrogen is composed of two protons and two electrons. The total wavefunction of a molecule consists of nuclear wavefunction and electronic wavefunction, each wavefunction being a product of orbital and spin functions. Let $\vec{r_1}$ and $\vec{r_2}$ are the position vectors of two electrons in the hydrogen molecule with $\vec{R_a}$ and $\vec{R_b}$ the position vectors of two nuclei as shown in Fig. 1. The spin vectors of the electrons and nuclei are defined as $\vec{s_i}$ (i=1,2) and $\vec{i_j}$ (j=a,b), respectively, and the quantum number of the total electron spin ($\vec{S} = \vec{s}_1 + \vec{s}_2$) and nuclear spin ($\vec{I} = \vec{i}_a + \vec{i}_b$) of the molecule are expressed as S and I, respectively.

Within the adiabatic approximation, the total wavefunction can be described by a product of the nuclear part ($\chi_n\phi_n$) and electronic part (ϕ_e) by separating the center of mass motion with $\vec{R} = \vec{R_a} - \vec{R_b}$:

$$\psi(\vec{r_1}, \vec{r_2}, S, \vec{R}, I) = \phi_e(\vec{r_1}, \vec{r_2}, S; \vec{R})\chi_n(I)\phi_n(\vec{R}), \quad (1)$$

where $\chi_n(I)$ and $\phi_n(\vec{R})$ represent the nuclear-spin part and spatial part of the wavefunction, respectively. Figure 2 shows the adiabatic potentials for

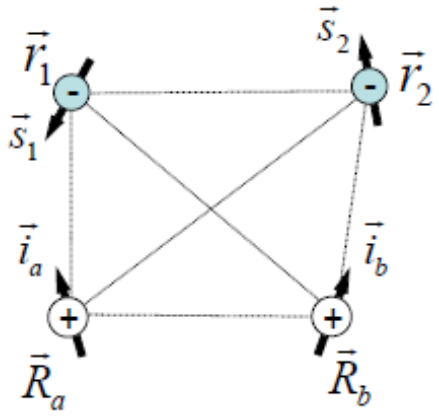

Figure 1: Definition of the position and spin vectors of electrons and nuclei in molecular hydrogen. $\vec{r_i}(i = 1, 2)$ and $\vec{R_j}(j = a, b)$ are the position vectors of the electrons and nuclei, respectively, and $\vec{s_i}$ (i=1,2) and $\vec{i_j}$ ($j = a, b$) are the spin vectors of the electrons and nuclei, respectively.

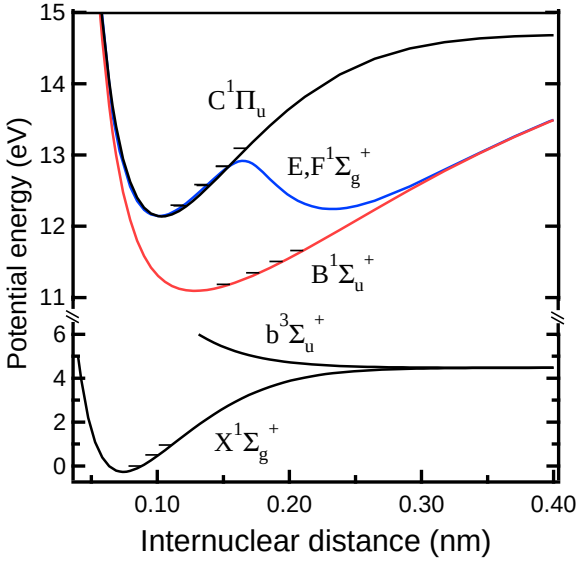

Figure 2: Adiabatic potentials for molecular hydrogen. The electron configurations are X ($(1s\sigma_g)^2$), B and b ($(1s\sigma_g)(2p\sigma_u)$), E,F ($(1s\sigma_g)(2s\sigma_g)$) and C ($(1s\sigma_g)(2p\pi_u)$) [34, 35, 36, 37].

molecular hydrogen, where the ground state of X and excited states of b, B, C and E,F are shown.

The nuclear part is physically understood as the nuclear motion on the adiabatic potentials. The nuclear wavefunction is further decomposed into the radial ($R = |\vec{R}|$) and angular (θ, ϕ) parts, which represent the vibrational and rotational motions:

$$\phi_n(\vec{R}) = L_v(R) Y_{J,M}(\theta, \phi). \tag{2}$$

In the first approximation, the vibrational motion corresponds to the vibration in harmonic potentials with the vibrational frequency described by the quadratic curvature of the potential around the potential-energy minimum. The orbital motion, on the other hand, is characterized by its angular momentum J with the wavefunction described by the spherical harmonics, and the energy is described as $BJ(J+1)$ with a rotational constant B in the rigid rotor approximation. The rotational constant is expressed by the moment of inertia that is determined by the atomic mass and interatomic distance. The rotational state has a degeneracy of $(2J + 1)$. If the effects of anharmonicity on the vibration and the change of the interatomic distance due to vibrational excitation on the rotation are taken into consideration, the total energy of the molecule E is described as [38]

$$\begin{aligned} E &= T_e + \omega_e(v + \frac{1}{2}) - \omega_e\chi_e(v + \frac{1}{2})^2 \\ &\quad + [B - \alpha_e(v + \frac{1}{2})]J(J + 1) - \frac{4B^3}{\omega_e^2} J^2(J + 1)^2, \end{aligned} \tag{3}$$

where T_e and ω_e are the constants representing the electronic and vibrational energies with a vibrational quantum number of v, and χ_e and α_e express the correction due to the anharmonicity and change of the interatomic distance upon vibrational excitation, which are listed in Tables 1 and 2 for H_2 and D_2.

The H_2 and D_2 molecules consist of two protons with nuclear spin 1/2 and deuterons with nuclear spin 1, respectively, i.e. the proton and deuteron are the Fermi and Bose particles, respectively. Because of the quantum statistics, the total wavefunction of H_2 and D_2 must be antisymmetric and symmetric with respect to permutation of the two nuclei, respectively. In the following, the transformation of the wavefunction due to the two-nuclei permutation is described.

Table 1: Electronic energy (T_e), vibrational constants (ω_e and $\omega_e\chi_e$) and rotational constants(B and α_e) for H_2 in the unit of cm^{-1} [39].

	T_e	ω_e	$\omega_e\chi_e$	B	α_e
X	0	4401.21	121.33	60.853	3.062
B	91700	1358.09	20.888	20.0154	1.1845
E	100082.3	2588.9	130.5	32.68	1.818

Table 2: Electronic energy (T_e), vibrational constants (ω_e and $\omega_e\chi_e$) and rotational constants(B and α_e) for D_2 in the unit of cm^{-1} [39].

	T_e	ω_e	$\omega_e\chi_e$	B	α_e
X	0	3115.5	61.82	30.4436	1.0786
B	91697.2	963.08	11.038	10.068	0.4198
E	100128.1	1784.42	48.1	16.37	0.6764

The nuclear-spin function is expressed according to the total nuclear spin, I, and I is either 1 or 0 for H_2 and 2, 1, or 0 for D_2. The spin eigenfunctions are expressed by sums of spin functions as shown in Figs. 3 and 4. Here, each ket corresponds to a product of two nuclear-spin functions with the numbers denoting the z components of the two spin states. As clearly seen in the formulas of Figs. 3 and 4, $\chi_n(I=1)$ and $\chi_n(I=0)$ of H_2 are symmetric and antisymmetric with respect to the permutation of the two spins, respectively. For D_2, on the other hand, whereas $\chi_n(I=2)$ and $\chi_n(I=0)$ are symmetric, $\chi_n(I=1)$ is antisymmetric with two-spin exchange. Of these states, the state with a larger spin multiplicity is called ortho and the other is called para species. The ortho and para H_2 are 3-fold and 1-fold degenerate, respectively, while the degeneracy of ortho and para D_2 is 6 and 3, respectively.

The exchange of the position vectors of the two nuclei correspond to the transformation of the polar and azimuthal angles as $\theta \to \pi - \theta$ and $\phi \to \pi + \phi$ as illustrated in Fig. 5. The rotational wavefunction is then transformed as Eq. 4. Since the two-nuclei exchange does not affect the inter-nuclear distance R, the vibrational wavefunction of diatomic molecules does not change the sign irrespective of the vibrational quantum number as

$$\begin{aligned} L_v(R) &\to L_v(R) \\ Y_{J,M}(\theta,\phi) &\to Y_{J,M}(\pi-\theta,\pi+\phi) = (-1)^J Y_{J,M}(\theta,\phi). \end{aligned} \tag{4}$$

$$\chi_n(I=1, I_z=1\sim-1) \qquad \chi_n(I=0, I_z=0)$$

$$\begin{cases} \left|\frac{1}{2},\frac{1}{2}\right\rangle \\ \frac{1}{\sqrt{2}}\left(\left|\frac{1}{2},-\frac{1}{2}\right\rangle+\left|-\frac{1}{2},\frac{1}{2}\right\rangle\right) \\ \left|-\frac{1}{2},-\frac{1}{2}\right\rangle \end{cases} \qquad \frac{1}{\sqrt{2}}\left(\left|\frac{1}{2},-\frac{1}{2}\right\rangle-\left|-\frac{1}{2},\frac{1}{2}\right\rangle\right)$$

Figure 3: Spin eigenfunctions χ_n of H_2 for I=1 and 0 with the z component (I_z) of the total nuclear spin $\vec{I}$. The first and second numbers in the kets represent the z components of the two spins. I=1 and 0 correspond to o-H_2 (odd J) and p-H_2 (even J), respectively.

Table 3: Symmetry with respect to two-nuclei permutation. S and A denote symmetric and antisymmetric states, respectively.

		S	A
Electron		Σ_g^+, Σ_u^-	Σ_u^+, Σ_g^-
Rotation (J)		even	odd
Nuclear spin (I)	H_2	1	0
	D_2	2, 0	1

As easily understood from Eq. 4, the rotational wavefunction changes its sign when J=odd.

Finally, the effect of the two-nuclei exchange on the electronic wavefunction is considered. With the two-nuclei permutation, the electron coordinates are changed as inversion with respect to the molecule center and mirror reflection with respect to a mirror plane through the molecular axis. Hence, the electron wavefunctions denoted as Σ_g^+ and Σ_u^- are symmetric, and those as Σ_g^- and Σ_u^+ are antisymmetric [p. 131 of Ref. [38]]. The symmetry relation is summarized in Table 3.

Since the total wavefunction of H_2 and D_2 is antisymmetric and symmetric with respect to the two-nuclei permutation as described above, the rotational state is correlated with the nuclear-spin state as depicted in Fig. 6 for the electronic states of Σ_g^+ and Σ_u^-. Shown on the left-hand side are para H_2 (p-H_2) and ortho D_2 (o-D_2) with even J, and ortho H_2 (o-H_2) and para D_2

$$\chi_n(I=2, I_z=2\sim -2)$$

$$\begin{cases} |1,1\rangle \\ \frac{1}{\sqrt{2}}\left(|1,0\rangle+|0,1\rangle\right) \\ \frac{1}{\sqrt{6}}\left(|1,-1\rangle+2|0,0\rangle+|-1,1\rangle\right) \\ \frac{1}{\sqrt{2}}\left(|0,-1\rangle+|-1,0\rangle\right) \\ |-1,-1\rangle \end{cases}$$

$$\chi_n(I=1, I_z=1\sim -1)$$

$$\begin{cases} \frac{1}{\sqrt{2}}\left(|1,0\rangle-|0,1\rangle\right) \\ \frac{1}{\sqrt{2}}\left(|1,-1\rangle-|-1,1\rangle\right) \\ \frac{1}{\sqrt{2}}\left(|0,-1\rangle-|-1,0\rangle\right) \end{cases}$$

$$\chi_n(I=0)$$

$$\frac{1}{\sqrt{3}}\left(|1,-1\rangle-|0,0\rangle+|-1,1\rangle\right)$$

Figure 4: Spin eigenfunctions χ_n of D_2 for I=2, 1 and 0 with the z component (I_z) of the total nuclear spin $\vec{I}$. The first and second numbers in the kets represent the z component of each spin. I=2 and 0 correspond to o-D_2 (even J), and I=1corresponds to p-D_2 (odd J).

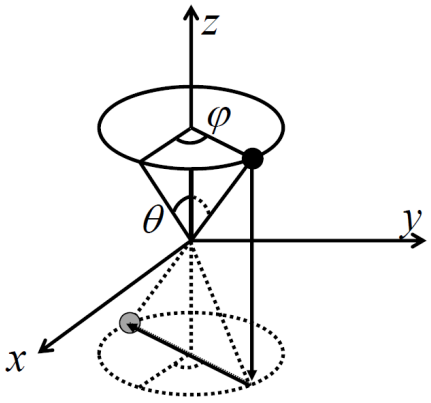

Figure 5: Transformation of the coordinates due to exchange of the two-nuclei position vectors that corresponds to reverse the sign of the relative position vector as $\vec{R} \to -\vec{R}$. The polar and azimuthal angles are transformed as $\theta \to \pi - \theta$ and $\phi \to \pi + \phi$.

(p-D_2) with odd J are shown on the right-hand side.

The partition function describing the population of each rotational level (E_J) at a temperature of T for o-H_2 ($Z_o(T)$) and p-H_2 ($Z_p(T)$) is described as

$$\begin{aligned} Z_o(T) &= \sum_{J=\text{odd}} g_{(I=1)}(2J+1)\exp(-\frac{E_J}{k_BT}) \\ Z_p(T) &= \sum_{J=\text{even}} g_{(I=0)}(2J+1)\exp(-\frac{E_J}{k_BT}), \end{aligned} \tag{5}$$

where $g_{(I=1)}$=3 and $g_{(I=0)}$=1 are the nuclear-spin degeneracies and $(2J+1)$ represents the rotational-state degeneracy. The population ratio of o-H_2 and p-H_2 (OPR: ortho-para ratio) in thermal equilibrium is then obtained by $Z_o(T)/Z_p(T)$, which is shown in Fig. 7 as a function of temperature. At a sufficiently low temperature, this value leads to 0, whereas it reaches 3 at a high temperature. Similarly, the para-ortho ratio of D_2 becomes 0 and 1/2 at low and high temperature limits, respectively, as obtained from the partition function of D_2.

2.2. Adsorption on solid surfaces

2.2.1. Adsorption potential

Molecular hydrogen is adsorbed on surfaces mainly in two schemes: dissociative chemisorption and molecular physisorption. In the former case, H_2 is dissociated and two hydrogen atoms are strongly bound via chemical bond formation. In the latter case, on the other hand, H_2 is weakly trapped on surfaces via the van der Waals interaction and electric multipole interaction. The typical adsorption energy is 0.5 eV per H atom for chemisorption and 30 meV per H_2 molecule for physisorption [40, 41, 42]. Since the ortho-para conversion via dissociative adsorption is out of the scope of this article, only the physisorption properties of H_2 are described in this section.

Physisorption of H_2 is realized by competition between the attractive van der Waals force and Pauli repulsion due to the overlap of the closed-shell electron wavefunctions with substrate electrons. Physisorption of various molecules was reviewed in a recent article [43]. As schematically shown in Fig. 8, the substrate electron density is smeared out at the surface, which determines the physisorption position. As discussed later, furthermore, the electron density at the substrate plays a decisive role in the ortho-para conversion. As intuitively understood from Fig. 8, both the van der Waals force and Pauli repulsion are dependent on the direction of the molecular axis.

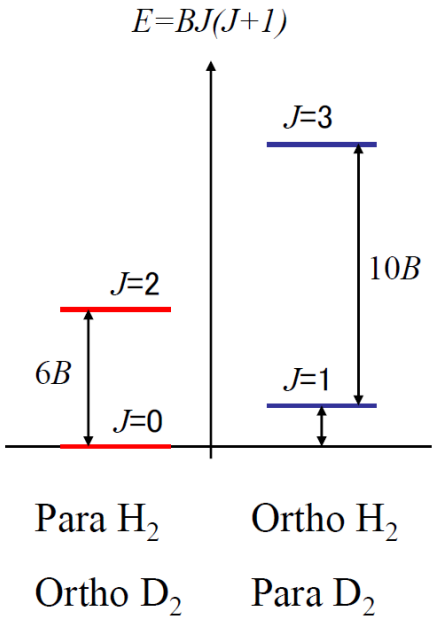

Figure 6: Rotational-energy levels for low-J states of the ortho and para species of H_2 and D_2 in the electronic Σ_g^+ and Σ_u^- states. $E = BJ(J+1)$ denotes the rotational energy with the rotational constant B and rotational quantum number J.

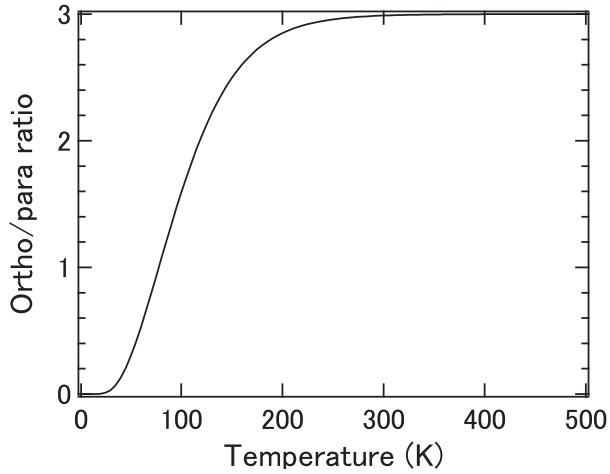

Figure 7: Ortho to para ratio (OPR) of H_2 calculated from the partition function for the rotational level as a function of temperature.

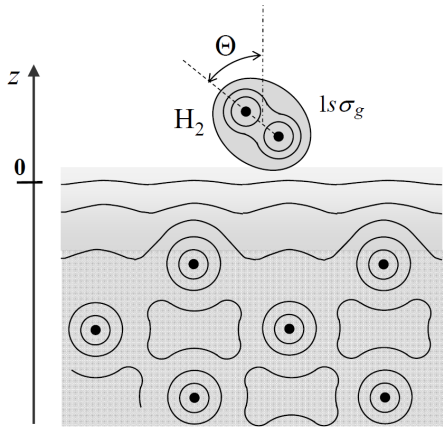

Figure 8: Schematic illustration of H_2 physisorbed on a surface at a certain distance. The surface electron density decays exponentially from the surface with increasing distance (z). H_2 with the $1s\sigma_g$ orbital exists in the tail region of the surface electron with the molecular-axis angle of Θ from the surface normal direction.

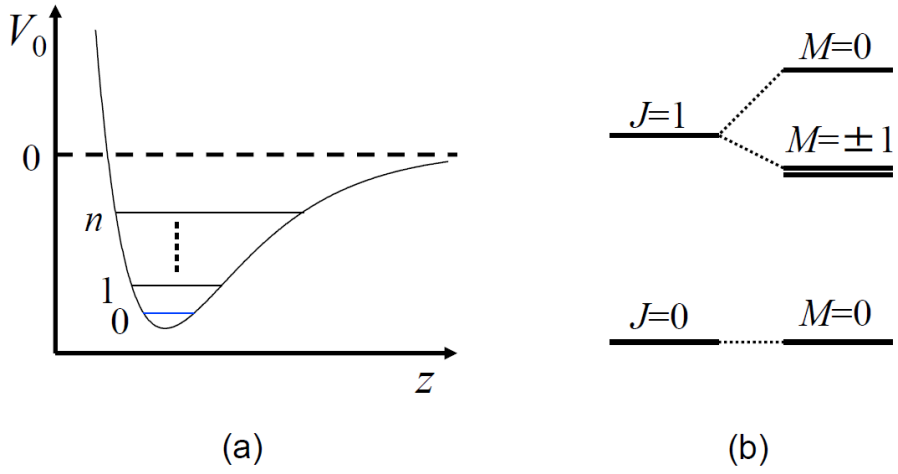

Figure 9: (a) Schematic figure of the physisorption potential due to the isotropic term V_0 as a function of the molecule-surface distance (z). The vibrational levels are denoted with the vibrational quantum number n. (b) Splitting of the rotational-energy level due to the $V_2(z)P_2(\cos\Theta)$ anisotropic term in the case of $V_2 < 0$.

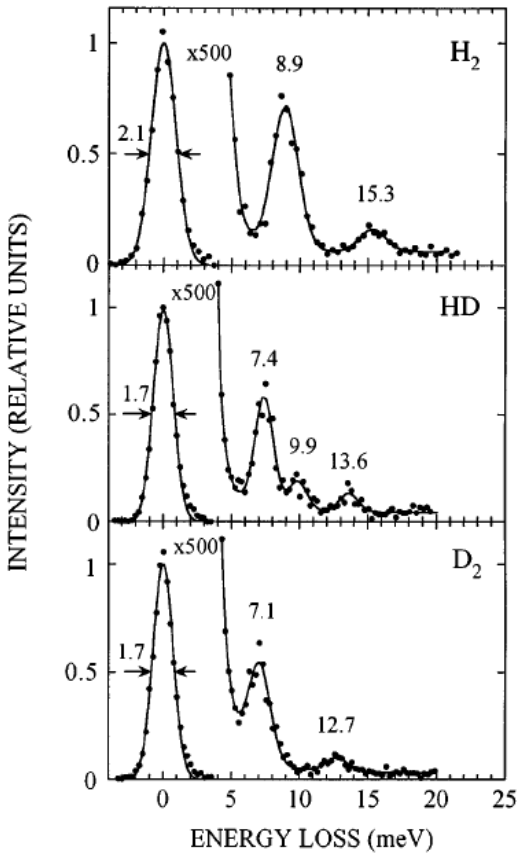

Figure 10: Electron energy loss spectra taken for H_2, HD and D_2 physisorbed on Cu(100) at about 10 K. The two loss peaks in each spectrum (except the feature at 9.9 meV in HD) correspond to n=0 → 1 and n=0 → 2 excitations of the molecule–substrate vibration shown in Fig. 9(a). Reproduced by permission from [44]. The vibrational energy is smaller for heavier isotopes.

The physisorption potential $V(z, \Theta)$ of a molecule is mainly characterized by its well depth and anisotropy, which represent the electrostatic energy as functions of the distance (z) of the center of mass of the molecule from the surface and the polar angle (Θ) of the molecular axis with respect to the surface normal. The potential is then generally expanded in Legendre functions as

$$V(z, \Theta) = \sum_{\ell=0}^{\infty} V_\ell(z) P_\ell(\cos\Theta). \tag{6}$$

Since H_2 is a homonuclear molecule, ℓ is restricted to even integers.

The first term of this formula represents the isotropic potential, which is schematically shown in Fig. 9(a). The well depth was theoretically evaluated to be 10 – 40 meV depending on the substrate [45, 46], which were also experimentally examined by selective adsorption experiments [47, 48, 49, 50, 51, 52, 53, 54], where molecular hydrogen is selectively adsorbed on surfaces at particular conditions of the kinetic energy and incidence angle corresponding to the bound states in the potential well. The adsorption energy can also be experimentally evaluated by temperature-programmed desorption (TPD) [55, 56, 57], which revealed the physisorption energy of 30 – 60 meV on ice and carbon surfaces. The vibrational states in the physisorption well were directly probed with EELS by Andersson's group [44]. Figure 10 shows the EELS data taken for H_2, D_2 and HD. Several loss features were observed at 7 – 15 meV, which were attributed to n=0 $\rightarrow$ 1 and n=0 $\rightarrow$ 2 excitations in Fig. 9(a), which compared well with the results of selective adsorption resonances. At low-symmetry sites like steps and kinks, the physisorption potential is largely modified as compared to the flat terrace site, and more strongly adsorbed H_2 has been identified [58, 59, 60, 61, 62, 63]. On adatom (Au and Cu)-adsorbed Cu(100), on the other hand, D_2 was found to be strongly adsorbed at the adatom site with a binding energy of about 40 meV [64]. Owing to recent advances of the density functional theory for the van der Waals interaction, the physisorption energy and potential of H_2 are theoretically treated from first principles [65, 66].

As mentioned in Sec. 2.1, the rotational energies of H_2 in the J=1 and 2 states are 14.7 and 43.9 meV, respectively, which are comparable to the physisorption energy. In contrast to heavier molecules, the rotational motion of molecular hydrogen is retained in the adsorption state. This is why molecular hydrogen is called a quantum rotor. Since the $V_\ell(z)P_\ell(\cos\Theta)$ ($\ell \geq 2$)

terms are expected to be comparable or smaller than the physisorption well depth due to the isotropic term ($V_0(z)$), the effect of the anisotropic potential can be treated as a perturbation.

According to the perturbation theory, the first-order energy shift due to the rotational motion is described by

$$\begin{aligned} \Delta E^{(1)}(n,J,M) &= \langle n|V_2|n\rangle\langle JM|P_2(\cos\Theta)|JM\rangle \\ &= \frac{3\langle n|V_2|n\rangle}{2J+3}\left(\frac{J^2-M^2}{2J-1}-\frac{J}{3}\right), \end{aligned} \tag{7}$$

where $\langle n|V_2|n\rangle$ is the matrix element of $V_2(z)$ with respect to the molecule-surface vibrational wavefunction in $V_0(z)$ and $|JM\rangle$ represents the rotational wavefunction of $Y_{J,M}(\Theta,\phi)$ [67]. The integral of $\langle JM|P_2(\cos\Theta)|JM\rangle$ is easily done following the formula for the angular momentum [68]. It is clear that the rotational-state degeneracy is lifted as shown in Fig. 9(b). Since the rotational wavefunction is unperturbed in the first-order perturbation, this is called nearly free rotor here[1]. The second-order energy term, on the other hand, is expressed as

$$\Delta E^{(2)}(n,J,M) = \sum_{n',J',M'} \frac{|\langle n'|V_2|n\rangle\langle J'M'|P_2(\cos\Theta)|JM\rangle|^2}{E(nJM)-E(n'J'M')}. \tag{8}$$

This second-order energy becomes significant when $\langle n'|V_2|n\rangle$ is in the same order as $E(nJM)-E(n'J'M')$, i.e. 44 meV for $J=0$ and 73 meV for $J=1$ in the case of $n=n'$. In this case, the rotational wavefunction is distorted from that of the original J state because of mixing with other rotational states, which is called hindered rotation here. The energy levels and wavefunctions of such hindered rotation were theoretically analyzed in detail [69]. Figure 11 shows the obtained energy levels as a function of the potential anisotropy for J=0 and 1 states [69]. Historically, the anisotropic potential was treated as either $C\cos^2\Theta$ or $C'\sin^2\Theta$ instead of $P_2(\cos\Theta)$ [69], where

[1]The rotational state under an isotropic potential is sometimes called three-dimensional (3D) rotation. In molecular physics, on the other hand, the 3D rotation occasionally denotes the rotational motion of non-linear molecules, which have three rotational axes (Θ,ϕ,χ) as compared to linear molecules (Θ,ϕ) called 2D rotation. To avoid confusion, we use the expressions of free rotor, nearly-free rotor, and hindered rotor to represent the rotational motion under isotropic potential, small anisotropic potential, and large anisotropic potential, respectively, in this article.

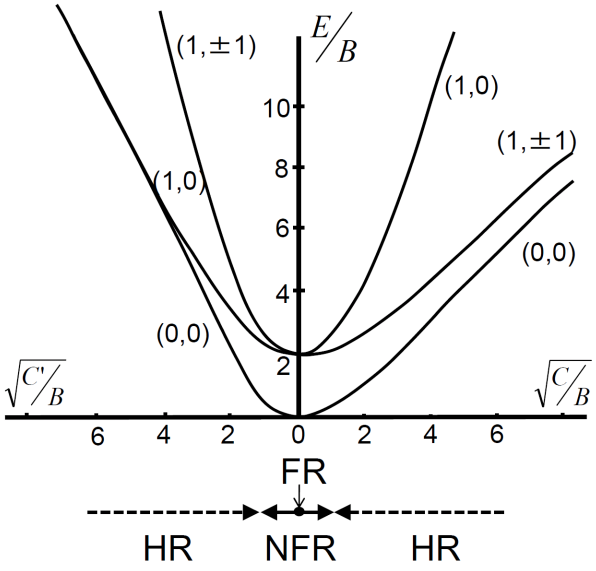

Figure 11: Rotational energy for the J=1 and J=0 states as a function of the square root of the ratio of the anisotropic potential to the rotational constant. The anisotropic potential is either $C\cos^2\Theta$ or $C'\sin^2\Theta$. Without anisotropic potential, the molecule behaves as a free rotor (FR). While the molecule is in a nearly free rotor (NFR) state under a small anisotropic potential, the rotational motion is described as a hindered rotor (HR) under a large anisotropy. Adapted from [69].

C and C' are constants. Since the mean value of the anisotropic potential with these formulas is positive, the energy level gets higher along with the lifting of the degeneracy of the J=1 state as C or C' becomes larger. As the anisotropic potential becomes infinitely large, the rotational motion tends to be confined in either the surface-normal or parallel direction depending on the sign of $V_2(z)$, which is sometimes designated one-dimensional (1D) or two-dimensional (2D) rotation in literatures, respectively. In the former case, the energy level of J=0 becomes equal to that of J=1 (M =0). On flat surfaces, however, such a large $V_2(z)$ value is unlikely to exist.

The rotational sublevel splitting was investigated both experimentally and theoretically. Selective adsorption experiments directly identified the level splitting and evaluated the potential anisotropy to be 1 – 2 meV on the basis of Eq. 7 [70, 71, 72]. Although the resolution was not sufficiently good for the observation of the splitting, an EELS study, by applying a particu-

lar scattering geometry, analyzed the sublevel splitting of 1.4 meV for the J=2 state on Cu(100) [73]. The anisotropy of the van der Waals interaction originates from the asymmetry of the molecular polarizability, which was theoretically evaluated to be as small as 7 % of the isotropic term because of the image charge effect [67]. On the other hand, the anisotropy of the repulsive part might be larger and dominant for physisorption. The physisorption energy and potential anisotropy of H_2 are theoretically analyzed on surfaces by Multi-reference-configuration-interaction calculations [74, 75] and van der Waals density functional theory [65]. On a more corrugated surface such as inner walls of nanopores, furthermore, the azimuthal dependence of the potential is significant, which lifts the degeneracy of the $M = \pm 1$ states in Fig. 9(b) It is noted that pure-rotational spectroscopy detailed in Sec. 4 allows for experimental analysis of the rotational-sublevel splitting and potential anisotropy [76, 77, 78].

2.2.2. Physisorption energy of ortho and para species

One important consequence of the potential anisotropy and resulting rotational sublevel splitting is the difference of the adsorption energy between the ortho and para species. The physisorption energy is determined by the sum of the isotropic term and anisotropic term of the potential. The isotropic term is the same for both ortho and para species. As clearly demonstrated in Fig. 9(b), on the other hand, some of the ortho-H_2 level are lowered due to the anisotropic term, the other being raised, while the p-H_2 level remains unchanged. This indicates that o-H_2 can be more strongly bound to surfaces under an anisotropic potential.

The adsorption energy difference was first recognized as the vapor pressure difference between the ortho and para species [79, 80]. This effect has been used for separation of o-H_2 and p-H_2: Under a fixed n-H_2 pressure, the o-p ratio in the physisorption state is higher than the gas phase value of 3 because of the larger adsorption energy for o-H_2, which is called the separation coefficient [13, 81]. The separation coefficient was theoretically analyzed in terms of the rotational-energy level splitting in the physisorption well [11, 12, 82, 69, 83, 84]. On these bases, highly purified o-H_2 and p-D_2 can be obtained with several condensation steps. The adsorption energy difference was also applied to Chromatographic separation, where more strongly bound o-H_2 is released later than p-H_2 [85, 86, 87].

The o-p separation was often performed on ionic surfaces like Al_2O_3. The origin of the potential anisotropy was, therefore, considered to be the

electrostatic energy originating from the hydrogen polarization induced by the electric field on an ionic-material surface [88]. From the chromatographic data, the potential barrier for rotation was experimentally evaluated to be C=0.46 kcal/mol for the anisotropy of $C\cos^2\Theta$ [89]. In addition to the out-of-plane anisotropy, the in-plane anisotropy was also analyzed [90], and the theory was applied to the heat capacity, entropy and o-p separation coefficient [91, 92]. The difference of the adsorption energy was also examined on a Graphon surface by a low-temperature calorimetric method: the heat of adsorption was estimated to be 0.91 and 0.96 kcal/mol for p-H_2 and o-H_2, respectively [93].

The adsorption energy difference can also be evaluated by probing the thermal stability of the ortho and para species on a surface. As detailed in Sec. 4, infrared absorption spectroscopy (IRAS) and resonance-enhanced multiphoton ionization (REMPI) combined with desorption techniques have been applied to distinguish the rotational state of molecular hydrogen on surfaces. By using IRAS, o-H_2 was shown to be more strongly adsorbed than p-H_2 on NaCl [94]. TPD spectroscopy combined with REMPI was performed on activated Al_2O_3 [24], amorphous ice [26, 95] and Ag surfaces [96]. Figure 12 shows the TPD spectra taken for H_2 from activated Al_2O_3. After exposure of the sample to n-H_2 of 3×10^3 L at 14 K, TPD of H_2 in the J=0 and 1 states was recorded. The peak temperature of the desorption signal in J=1 is clearly higher than that of J=0 suggesting that H_2 in J=1 is more strongly bound than J=0. Similar experiments were performed for D_2 on amorphous ice surfaces [26], which is shown in Fig. 13. Dominant desorption species are in the J=0 and 1 states, and the desorption temperature of J=1 is obviously higher than that of J=0 indicating stronger binding of D_2 in J=1.

2.2.3. Sticking probability

When o-H_2 undergoes o-p conversion in a physisorption well, the initial step is the sticking of o-H_2 to surfaces from gas phase. The overall conversion probability therefore depends on the sticking probability. The sticking probability of light molecules like hydrogen on a substrate with heavier elements is usually small, typically $\sim$0.1 because the energy dissipation is inefficient. When the surface is covered by H_2, the sticking probability is reported to be 1 [97], because the kinetic energy of the incident molecule is readily accommodated by preadsorbed molecules. In an o-p conversion experiment, furthermore, the relative coverage of o-H_2 and p-H_2 is often discussed. Then, the difference of the sticking probability onto surfaces of these species has

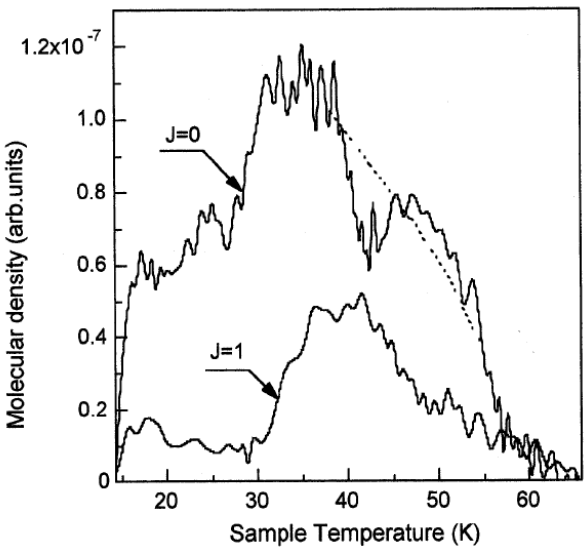

Figure 12: Rotational-state-selective temperature-programmed desorption spectra of H_2 from activated Al_2O_3 powder measured with a heating rate of 0.1 K/s. H_2 in J=0 and 1was probed by REMPI after exposure of the sample to n-H_2 of 3×10^3 L at 14 K. The activated Al_2O_3 powder with a specific area of 270 m^2/g was heated at 520 K for 10 h prior to the experiments. The dip at 42 K for the J=0 spectrum is due to the REMPI laser instability, and the dashed curve is a guide for eyes. Reproduced by permission from [24].

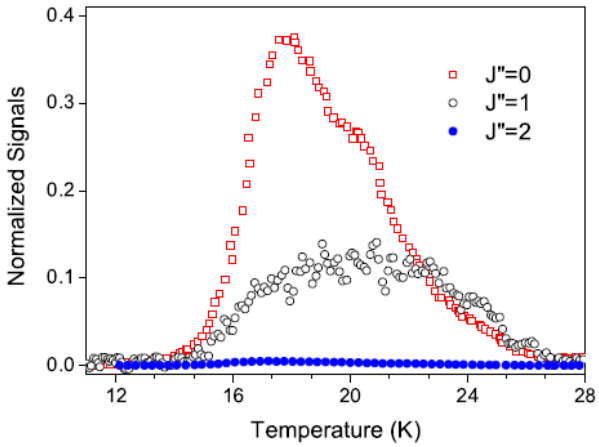

Figure 13: Rotational-state-selective temperature-programmed desorption spectra of D_2 from amorphous ice surfaces. D_2 of 1.5 monolayer (ML) was adsorbed on porous amorphous ice of 10 ML at 10 K. D_2 is mostly desorbed in J=0 and 1 states, and the desorption temperature for J=1 is higher than that of J=0. Reproduced by permission from [26].

to be carefully examined. Historically, when EELS studies first observed a higher intensity of the loss feature corresponding to p-H_2 as compared to that of o-H_2, the sticking probability of p-H_2 was suspected to be higher than o-H_2. Such possibility was later discussed to be small. In this subsection, previous studies on the sticking probability of ortho and para hydrogen are briefly described.

For molecular adsorption on solid surfaces, an important factor governing the sticking probability is the dissipation of the incident kinetic energy and adsorption energy. In the physisorption potential of Fig. 9(a), the impinging molecule is in a continuum state with a positive energy, and comes from larger z toward the potential minimum. Sticking of a molecule is regarded as the transition from a continuum state with a positive energy to a bound state with a negative energy in the potential by dissipating the energy between the initial and final states to other degrees of freedom. Two important paths of the energy dissipation are phonon excitation and electronic excitation of surfaces. In the case of chemisorption, electronic excitation is important (e.g. [98]). As for the weak physisorption of light molecules, on the other hand, coupling to electronic excitation is expected to be weak, and sticking occurs via energy transfer to the substrate phonon system [53]. Other important

factors for molecular sticking are temporal trapping in the physisorption well via the energy transfer of the kinetic energy of an impinging molecule in the surface normal direction to the kinetic energy in the parallel direction or the internal energy. This process corresponds to the selective adsorption resonance. As the internal-vibrational energy of molecular hydrogen is as high as 500 meV, the accessible internal mode is the rotational motion of the molecule. Since the total energy of the trapped molecule is still positive, this corresponds to a quasibound state, and further energy dissipation is required for the transition of the molecule into the true stuck state with a total energy of a negative value.

Experimentally, Andersson and Harris investigated the sticking probability of n-H_2 and p-H_2 with EELS and workfunction change ($\Delta\phi$) measurements to clarify the effect of the rotational motion on the sticking [99]. They first evaluated the EELS cross section for J=0 $\rightarrow$ 2 and J=1 $\rightarrow$ 3 transitions to be the same as those in the gas phase, then precisely determined the ortho and para H_2 coverages from the EELS intensities. On the basis of the data, the sticking probability ratio for p-H_2 to n-H_2 was evaluated to be 1.5. They proposed that the trapping of H_2 via translational to rotational energy transfer is significant.

In later publications, the sticking probability of H_2 and D_2 was investigated in a more sophisticated way [100, 101, 53]. By changing the incident energy and angle of molecular beams, both the sticking and reflection of incident molecules were experimentally measured in detail. Figure 14 shows the initial sticking coefficient, S_0, of n-H_2 and p-H_2 on Cu(100) at 15 K as a function of the molecule energy. The sticking probability revealed a smooth behavior falling off around 30 – 50 meV. This energy reflects the substrate phonon density of states, which points to the phonon-mediated dissipation [100, 53, 102]. This broad feature extending up to $\sim$50 meV cannot be explained by classical theory, and quantum treatment was shown to be necessary to reproduce the sticking behavior [53]. Overlapped with this smooth behavior, an enhancement of S_0 at an energy corresponding to rotational excitation of J=0 $\rightarrow$ 2 was observed as indicated in Fig. 14. After more detailed and careful experiments and theoretical analysis, all features observed in the sticking curves were attributed to either corrugation-mediated selective adsorption resonances, rotation-mediated selective adsorption resonances or combined resonances involving both rotational excitation and diffraction [52, 53].

For the energy transfer from the translational motion to rotational mo-

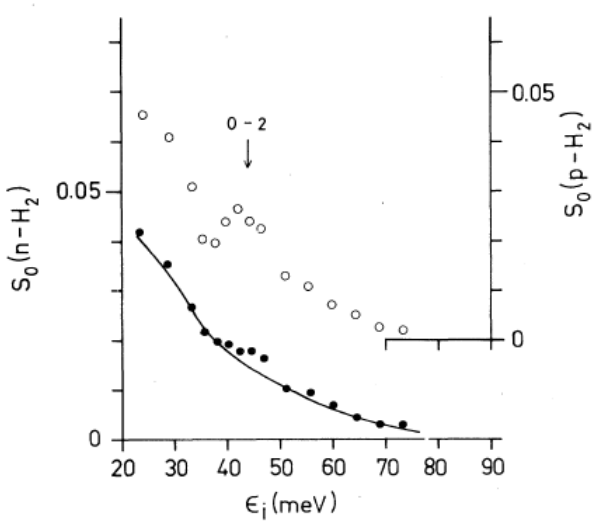

Figure 14: Sticking probability of n-H_2 and p-H_2 as a function of the incident energy of H_2 on Cu(100) at 15 K. Both reveal a broad feature extending up to ∼50 meV, and the curve for p-H_2 shows a hump corresponding to the rotational excitation of J=0 → 2. Reproduced by permission from [100].

tion, there must be coupling between these modes; while the two motions are independent under an isotropic potential, they are coupled by the anisotropic term of the potential described in Sec. 2.2. The energy transfer from the normal motion to parallel motion, on the other hand, can be achieved by the potential corrugation on the surface, i.e. potential difference as a function of the molecule position in the surface parallel direction. When further interaction with the substrate phonon is taken into consideration, relaxation from the quasibound state to the bound state can be calculated. According to semiclassical trajectory calculations [103] and one-phonon distorted-wave Born-approximation calculations [104], the selective adsorption resonances are weak and dependence of the sticking probability on the rotational state is small. Sticking and associated energy dissipation are obviously important and continuing issues in Surface Science [105, 106].

3. Ortho-para conversion – theoretical aspect

As described in previous sections, the wavefunctions of the ortho and para hydrogen are orthogonal with each other without coupling between the

nuclear-spin and rotational motion. Other molecules such as NH_3, CH_4 and H_2O are also classified into nuclear-spin isomers. The theory of the ortho-para conversion of polyatomic molecules was well developed [107, 108], and has been applied to e.g. CH_3F [109], C_2H_4 [110], H_2CO [111], CH_4 [112], C_2H_3 [113] and H_2O [114]. The theory is essentially based on the intramolecular mixing of the ortho and para states. Because of the spin-spin and spin-rotation interaction, there possibly occurs mixing between the ortho and para states. Although these coupling terms are generally small and negligible, the mixing becomes significant when the energy levels of the ortho and para states are near-degenerate. This may be accidentally realized because polyatomic molecules have some rotational modes with different rotational constants. The mechanism of the o-p conversion of polyatomic molecules was discussed that thermal excitation to the near-degenerate levels results in finite mixing between the ortho and para states leading to o-p conversion [108].

Compared to the polyatomic molecules, because of the small moment of inertia, hydrogen molecules have a large energy separation between the rotational states. In the physisorption state at low temperature dealt with in this article, therefore, the rotational states accessible by thermal excitation are restricted to low-J sates, only J=1 and 0. Under this condition, mixing of the ortho and para states is extremely small and spontaneous conversion probability can be neglected as described below.

When there is a perturbation H' due to interaction with surfaces and the matrix element between the ortho and para states has a non-zero value, the o-p transition probability becomes significant. In this section, fundamental concepts for the o-p conversion are reviewed.

3.1. Gas phase conversion mechanism

3.1.1. Radiative transition

In an isolated state, radiative transition occurs through interaction of a molecule with the electromagnetic field. Following the ordinary procedure, the dominant perturbation term is the electric dipole described with the position vectors of electrons ($\vec{r_1}, \vec{r_2}$) and nuclei ($\vec{R_a}, \vec{R_b}$) and the electric field $\vec{E}$:

$$H' = e(\vec{r_1} + \vec{r_2} - \vec{R_a} - \vec{R_b}) \cdot \vec{E}. \tag{9}$$

It is easy to see that the dipole moment apparently remains unchanged by exchange of the position vectors of $\vec{R_a}$ and $\vec{R_b}$. Since the symmetry of the

wavefunction with respect to the two-nuclei position exchange is different for the ortho and para species, either symmetric or antisymmetric, the dipole moment between the ortho and para states is identically zero. This indicates the transition between the ortho and para states is a forbidden process. Considering the spin part, because the dipole moment does not contain the spin vector, the ortho and para states with the nuclear-spin triplet and singlet states are also orthogonal.

The radiative ortho-para conversion probability was first discussed theoretically by considering the hyperfine interaction strength and mixing of the electronically excited states [115]. The transition probability was evaluated to be $\sim 10^{-10}$ s^{-1} [115, 1, 116]. In their discussion, however, only the mixing with the $^3\Sigma_u^+$ state was taken into consideration, which means that the selection rule for the rotational and spin states was not considered correctly. Therefore, the value so obtained was an overestimation. Later, the o-p conversion probability was more accurately evaluated on the basis of the relativistic spin-orbit interaction (nuclear spin and electron orbital momenta) [117, 118, 119, 120], and the formula for the probability of the $J \rightarrow J-1$ transition was obtained. According to this formula, the $J = 1 \rightarrow J = 0$ transition probability can be calculated to be 7×10^{-20} s^{-1}. A more accurate and complete calculation was recently performed by Pachucki and Komasa by taking account of a nonadiabatic correction for H_2 and relativistic corrections, the value obtained being 6.2×10^{-14} yr^{-1}=2.0×10^{-21} s^{-1} [121]. Note that this time scale for conversion (inverse of the conversion probability) is longer than the age of the universe (1.37×10^{10} yr).

3.1.2. Proton exchange

The o-p conversion of H_2 in an isolated state does not take place practically. When H_2 encounters other atoms or ions, the o-p conversion might be induced via proton exchange [122]:

$$\begin{aligned} \mathrm{o-H_2 + H} &\rightarrow \mathrm{p-H_2 + H} \\ \mathrm{o-H_2 + H^+} &\rightarrow \mathrm{p-H_2 + H^+}. \end{aligned}$$

These processes have been investigated in gas phase. Of the two reactions, there is an activation barrier of $\sim$0.3 eV for the H_2 + H reaction [123]. The conversion cross section was estimated to be less than 10^{-16} cm^3 s^{-1} at 300 K [123, 124]. It should be noted that the H atom possibly causes ortho-para conversion of H_2 through magnetic interaction on the basis of

the Wigner model described in Sec. 3.3.2 because H possesses an unpaired electron spin. As to the latter reaction, on the other hand, the reaction rate for $H_2 + D^+ \rightarrow HD + H^+$ was experimentally estimated to be 1–2 $\times 10^{-9}$ $cm^3 s^{-1}$ [125, 126]. Theoretically, the o-p conversion probability was initially evaluated to be about 10^{-10} cm^3 s^{-1} [124]. Later, the conversion rate for J=1 $\rightarrow$ 0 was more accurately evaluated to be 2.2×10^{-10} cm^3 s^{-1} by statistical theory [127], and J=0 $\rightarrow$ 1,3 excitation probability was calculated in terms of S-matrix [120]. Recent studies by Honvault et al. employed a fully quantum time-independent approach combined with a high accuracy ab initio potential energy surfaces (PES) to derive the cross section as a function of the collision energy [128, 129]. The rate coefficient is calculated to be 4.15×10^{-10} $cm^3 s^{-1}$ at 10 K.

As discussed in Sec. 6, H and H^+ are dominant species in an astronomical environment, which induce o-p conversion via proton exchange as described above. In addition to H and H^+, H_2 might encounter H_3^+ or o-H_2 in space. While H_3^+ would also induce o-p conversion via proton exchange [126, 130], o-H_2 + o-H_2 might temporarily form H_4 [131], which would eventually lead to two p-H_2 molecules. The proton exchange processes might be significant on surfaces when co-adsorbed with these species.

3.2. Basic interaction inducing o-p conversion

The nuclear wavefunctions of the ortho and para hydrogen are as shown in Eqs. 1 and 2 described by the products of the nuclear-spin function and rotational-vibrational wavefunction, which are functions of the spin coordinates ($\vec{i_a}$ and $\vec{i_b}$) and position coordinates ($\vec{R_a}$ and $\vec{R_b}$) defined in Fig. 1, respectively. Although there is a coupling between the nuclear spin and rotational angular momentum [132], the spin and rotational parts are described in a separated form here, because the coupling term is small and the physical picture for transition is better understandable. For the o-p conversion of H_2, the spin state is changed from the triplet state to the singlet state, while the rotational state is changed from a J=odd state to a J=even state. As shown below, H' must contain $\vec{i}$ ($\vec{i}$=$\vec{i_a} - \vec{i_b}$) and $\vec{R}$ ($\vec{R} = \vec{R_a} - \vec{R_b}$) for the spin-state transition and rotational-state transition, respectively. Here, the calculation is shown for the H_2 case below, yet the results are essentially the same for D_2.

Any perturbation Hamiltonian containing operators $\vec{i_a}$ and $\vec{i_b}$ is generally expressed by the following formula with coefficients A and B, and can be

described by functions of $(\vec{i_a} + \vec{i_b})$ and $(\vec{i_a} - \vec{i_b})$:

$$H' = A\vec{i_a} + B\vec{i_b} = \frac{A+B}{2}(\vec{i_a} + \vec{i_b}) + \frac{A-B}{2}(\vec{i_a} - \vec{i_b}). \quad (10)$$

We consider the matrix element of H' between the nuclear-spin functions χ_n in Fig. 3. Since χ_n's are the eigenstates of the total nuclear spin $\vec{I}$ $(=\vec{i_a} + \vec{i_b})$, the matrix element of $(\vec{i_a} + \vec{i_b})$ between $\chi_n(I = 1)$ and $\chi_n(I = 0)$ is zero. On the other hand, the matrix element of $\vec{i}$ between $\chi_n(I = 1)$ and $\chi_n(I = 0)$ is non-zero:

$$\begin{aligned} < \chi_n(I=0)|i^{\pm}|\chi_n(I=1, I_z = \mp 1) > &= \mp\sqrt{2} \\ < \chi_n(I=0)|i^{z}|\chi_n(I=1, I_z = 0) > &= 1, \end{aligned} \quad (11)$$

where $i^{\pm}$ denotes the raising and lowering operators divided by $\hbar$. Therefore, the perturbation of $\vec{i}$=$\vec{i_a} - \vec{i_b}$ mixes the ortho and para states leading to finite transition probability (see Appendix A).

On the other hand, the position coordinates $\vec{R}$ ($\vec{R}$=(x, y, z)= (R, θ, ϕ)) are expressed in the spherical expression as

$$\begin{aligned} R^{\pm 1} &= \mp\frac{x \pm iy}{\sqrt{2}} = R\sqrt{\frac{4\pi}{3}}Y_{1,\pm 1} \\ R^{0} &= z = R\sqrt{\frac{4\pi}{3}}Y_{1,0}. \end{aligned} \quad (12)$$

In a similar way to the spin functions, the matrix element of $R^{\pm 1,0}$ between the rotational states of ortho and para H_2, $Y_{1,M}$ and $Y_{0,0}$, is described as [68]

$$\begin{aligned} < Y_{0,0}|R^{\pm 1}|Y_{1,\mp 1} > &= -\frac{R}{\sqrt{3}} \\ < Y_{0,0}|R^{0}|Y_{1,0} > &= \frac{R}{\sqrt{3}}. \end{aligned} \quad (13)$$

Although the above formula is given for the transition between the J=1 and J=0 states, it is easily generalized for arbitrary J states.

Finally, the matrix element of Eq. 13 between the vibrational wavefunctions $(L_v(R))$ is evaluated with the equilibrium interatomic distance of R_e as

$$< L_{v'}(R)|R|L_v(R) > = < L_{v'}(R)|R_e|L_v(R) > + < L_{v'}(R)|(R - R_e)|L_v(R) > . \quad (14)$$

Here, the first and second terms of Eq. 14 give the selection rule of Δv=0 and ± 1, respectively, for a harmonic oscillator.

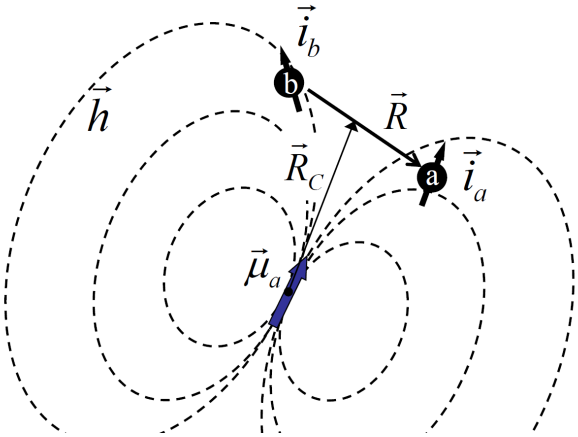

Figure 15: Schematic illustration of a hydrogen molecule under an inhomogeneous magnetic field $\vec{h}$ expressed by dashed curves. $\vec{i_a}$ and $\vec{i_b}$ denote the nuclear spins of nuclei a and b, respectively. $\vec{R}$ and $\vec{R}_c$ represent the relative coordinate vector and the center of mass coordinate vector, respectively, i.e. $\vec{R}_a = \vec{R}_c + \vec{R}/2$ and $\vec{R}_b = \vec{R}_c - \vec{R}/2$. The inhomogeneous magnetic field is expressed by a dipole field originating from a magnetic dipole moment $\vec{\mu}_a$.

3.3. First-order perturbation

3.3.1. Perturbation Hamiltonian

Magnetic dipole interaction

When there is an inhomogeneous magnetic field as schematically shown in Fig. 15, the perturbation is expressed as

$$\begin{aligned} H' &= g_n\beta_n(\vec{i_a}\cdot\vec{h_a} + \vec{i_b}\cdot\vec{h_b}) \\ &= \frac{g_n\beta_n}{2}[(\vec{i_a}+\vec{i_b})\cdot(\vec{h_a}+\vec{h_b}) + (\vec{i_a}-\vec{i_b})\cdot(\vec{h_a}-\vec{h_b})] \end{aligned} \tag{15}$$

where $\vec{h_a}$ and $\vec{h_b}$ denote the magnetic field at the nuclei (a and b), and g_n and β_n are the nuclear g-factor and nuclear magneton, respectively. Following the discussion in Sec. 3.2, the second term contributes to the spin conversion. Since $(\vec{h_a} - \vec{h_b}) \cong \vec{R}\cdot\nabla\vec{h}(\vec{R_c})$ as the first term of the Taylor expansion, it is seen that this term contains the operator $\vec{R}$ [21]. When the magnetic field is inhomogeneous, i.e. $\nabla\vec{h}(\vec{R_c}) \neq 0$, this term is effective for o-p conversion.

In Fig. 15, the magnetic field is expressed by the dipolar field due to a

point magnetic moment near H_2 as

$$\vec{h}(\vec{r}) = \frac{1}{4\pi\mu_0}(\frac{\vec{\mu_a}}{|\vec{r}|^3} - \frac{3\vec{\mu_a}\cdot\vec{r}}{|\vec{r}|^5}\vec{r}), \quad (16)$$

which indicates that the field can be inhomogeneous on an atomic scale. The magnetic moment originates from either spins or orbital angular momenta of electrons and nuclei. Since the electron Bohr magneton is $\sim 10^3$ as large as the nuclear magneton, the o-p conversion due to the nuclear spin tends to be $\sim 10^6$ as slow as that due to the electron spin. This interaction was considered for the o-p conversion due to interaction of magnetic impurities, magnetic materials, and solid H_2.

The magnetic dipole moment was usually treated as a point dipole. Electrons are however spatially extended as expressed by wavefunctions. The effect of the extended feature of electrons on the dipole interaction was theoretically examined, and was shown to possibly enhance the o-p conversion rate [133, 134].

Fermi contact interaction

When there is a finite electron density at the nucleus position, there occurs the Fermi contact interaction. With the electron spin density operator ($\vec{s}(\vec{r})$) and one electron density operator ($\rho(\vec{r})$), the Fermi contact interaction of the electron with the two nuclei of H_2 is described as

$$\begin{aligned} H' &= \frac{8\pi}{3}\frac{\mu_0}{4\pi}g_n\beta_n g_e\beta_e\{\vec{s}(\vec{R}_a)\cdot\vec{i}_a + \vec{s}(\vec{R}_b)\cdot\vec{i}_b\} \\ &\cong \frac{2\mu_0}{3}g_n\beta_n g_e\beta_e[\{\vec{s}\cdot(\vec{i_a}+\vec{i_b})\}\{\rho(\vec{R}_a)+\rho(\vec{R}_b)\} \\ &\quad +\{\vec{s}\cdot(\vec{i_a}-\vec{i_b})\}\{\rho(\vec{R}_a)-\rho(\vec{R}_b)\}], \end{aligned} \quad (17)$$

where g_e and β_e are the electron g-factor and Bohr magneton, respectively [21]. Since the surface electron wavefunction spills over from the surface exponentially as schematically shown in Fig. 8, H_2 in the physisorption well suffers from the Fermi contact interaction. As the magnetic dipole interaction, the electron density difference in the second term of the Hamiltonian can be approximated as the first term of the Taylor expansion with respect to the position vector as $\vec{R}\cdot\nabla\rho(\vec{R_c})$ [21, 135]. Then, it is shown that the perturbation is significant when the electron density is inhomogeneous containing both $\vec{R}$ and $\vec{i_a}-\vec{i_b}$, and mixes the ortho and para states.

In addition to the direct Fermi contact interaction, the overlap between the surface electron orbital and H_2 orbital was shown to be significant for the Fermi contact interaction leading to enhancement of the o-p conversion rate [135, 133]. Furthermore, the intramolecular Fermi contact interaction becomes important when considering higher-order perturbation through interaction with surfaces, which will be described in Sec. 3.4.

Electron motion

If the electron motion is taken into consideration, there occurs an interaction between the nuclear spin and the magnetic field originating from the electron motion. As is usual the case for the interaction with the electromagnetic field, this interaction can be described as

$$H' = \frac{e}{2m_e}\sum_{i=a,b}[\vec{p}\cdot\vec{A}(\vec{r}-\vec{R}_i)+\vec{A}(\vec{r}-\vec{R}_i)\cdot\vec{p}] \quad (18)$$

where $\vec{A}(\vec{r})$ is the vector potential originating from the magnetic field produced by hydrogen nuclear spins, and $\vec{p}$ and m_e denote the electron momentum and mass, respectively [21]. Since $\vec{A}(\vec{r})$ is described by the outer product of the magnetic moment and the position vector, the perturbation Hamiltonian has a term proportional to $[(\vec{i_a}-\vec{i_b})\times(\vec{R}\cdot\nabla)\vec{D}]\cdot\vec{p}$ with $\vec{D}=(\vec{r}-\vec{R})/|\vec{r}-\vec{R}|^3$ [21]. As in the cases above, it mixes the ortho and para states. This interaction was named "spin-orbit interaction" in the paper by Yucel [21], because the interaction between the nuclear spin and electron orbital motion is taken into account. Nevertheless, it should be noted that this is not the ordinary spin-orbit interaction that appears as a relativistic effect [136].

Quadrupole interaction

The deuteron nucleus has a quadrupole moment Q_μ as shown in Table 4, which interacts with the electric-field gradient V_μ [137, 138, 139]. The interaction Hamiltonian of D_2 with the electric-field gradient is expressed in the spherical representation as

$$\begin{aligned} H' &= \sum_{\mu=0,\pm1,\pm2}[V_\mu(\vec{R}_a)Q^a_\mu + V_\mu(\vec{R}_b)Q^b_\mu] \\ &= \frac{1}{2}\sum_{\mu=0,\pm1,\pm2}[V_\mu(\vec{R}_a) \\ &\quad +V_\mu(\vec{R}_b)](Q^a_\mu+Q^b_\mu)+[V_\mu(\vec{R}_a)-V_\mu(\vec{R}_b)](Q^a_\mu-Q^b_\mu) \end{aligned} \quad (19)$$

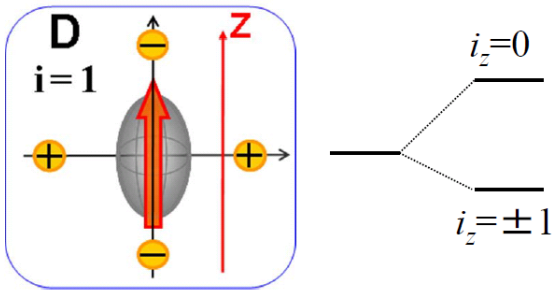

Figure 16: Schematic illustration of the quadrupole interaction with an electric-field gradient. The electric-field gradient is expressed by four point charges, and the ellipsoidal charge distribution aligns the spin direction lowering the energy of the $i_z = \pm 1$ state.

Table 4: Nuclear g-factor and quadrupole moment (Q) of proton and deuteron.

	$g-$ factor	Q (e·fm^2)
proton	+5.6	0
deuteron	+0.86	+0.28

As the above treatments, the second term in the summation is approximated as $[\vec{R} \cdot \nabla V_\mu(\vec{R}_c)](Q^a_\mu - Q^b_\mu)$ in the first term of the Taylor expansion. Since Eq. 19 contains $\vec{R}$ and $Q^a_\mu - Q^b_\mu$ has non-vanishing matrix elements between the $\chi_n(I = 1)$ of p-D_2 and $\chi_n(I = 2)$ of o-D_2 [139], the quadrupole interaction induces the para-ortho (p-o) conversion of D_2.

The quadrupole interaction is qualitatively understood by Fig. 16. While the nuclear-charge distribution is spherical for the proton, the deuteron has a non-spherical charge distribution and the spin direction is aligned to the major axis of the nucleus due to the relative motion of the proton and neutron in the nucleus. If there is an electric field gradient as represented by the charge distribution shown in Fig. 16, the electrostatic energy depends on the spin direction leading to lifting of the degeneracy.

3.3.2. Transition probability

Wigner law

Following the time-dependent perturbation theory, the amplitude of a

p-H_2 state, C_p, changes as [136]

$$i\hbar\frac{dC_p}{dt} = \langle p|H'|o\rangle \exp(-i\omega_{op}t). \tag{20}$$

Here, $\hbar\omega_{op}$ represents the energy difference between the initial ortho ($|o\rangle$) and final para ($|p\rangle$) states, which is denoted by the o-p energy. By integrating the above equation, the probability to find the para state at time t can be expressed as

$$|C_p|^2 = \frac{|\langle p|H'|o\rangle|^2}{\hbar^2}\frac{\sin^2(\omega_{op}t/2)}{(\omega_{op}/2)^2}. \tag{21}$$

When H' is the dipole magnetic field due to a paramagnetic impurity with a magnetic moment of μ_a as schematically shown in Fig. 15, $H' \propto \nabla\vec{h}(\vec{R}_c)$ is proportional to a^{-4} ($a = |\vec{R}_c|$).

To evaluate the transition probability, it is assumed that the perturbation is present within a finite time. Wigner assumed that a corresponds to the interaction region around a paramagnetic impurity, and that the converting hydrogen molecule moves across this region with a thermal velocity of v [140]. The duration time t of the perturbation is then expressed as $t = a/v$, which leads to the transition probability P as

$$P = \frac{\mu_a^2(g_n\beta_n)^2K}{3h^2\mu_0^2a^6M_pv^2}. \tag{22}$$

Here, $K = M_pR^2/2$ is the moment of inertia of the molecule, and the kinetic energy is taken as $M_pv^2 = 3k_BT$ with the proton mass of M_p and temperature of T. This conversion rate is proportional to μ_a^2/a^6, which is referred to as the Wigner law. This was later applied to a heterogeneous physisorption system [141].

Spectral density

In the Wigner formalism, the o-p energy was simply assumed to be accommodated by the kinetic energy of the molecule. This energy dissipation/excitation can be more rigorously treated by considering the transition from an energetically discrete state to a continuum state with a density of states. The transition probability can be described on the basis of the time-dependent perturbation theory as [136]

$$P = \frac{2\pi}{\hbar}|\langle f|H'|i\rangle|^2J(\hbar\omega_{op}). \tag{23}$$

Here, $J(\hbar\omega_{op})$ represents the density of states with an energy of $\hbar\omega_{op}$, and $|i\rangle$ and $|f\rangle$ are the initial ortho and final para states including the degrees of freedom for energy dissipation.

The density of states was theoretically treated by taking account of the time evolution of the molecule position, where the correlation of the molecule position gives rise to a spectral density. In addition to the translational motion of the molecule, the paramagnetic spin correlation was also taken into consideration implying that the spin system absorbs/emits the o-p energy via spin waves. These were first discussed by Leffler [142] by fixing the two-nuclei position without considering the rotational motion [143]. On the same ground, the o-p conversion was dealt with in terms of the nuclear-spin relaxation [144]. However, the rotational motion is essential for the o-p conversion, and must be taken into consideration.

The energy dissipation/excitation upon o-p conversion was later more accurately discussed by Ilisca, and the relative importance of the translational motion and spin waves was compared in detail [145, 146]. Petzinger and Scalapino then gave the absolute conversion rate on the same ground [132]. The idea of the o-p energy transfer to the spin system was further discussed for the o-p conversion on magnetic surfaces. It was pointed out that the spin relaxation time gets shorter above the phase transition temperature of magnetic surfaces and becomes significant for the energy transfer thereby enhancing the o-p conversion [147, 148, 14]. In relation to the o-p conversion on magnetic surfaces, it is known that there are significant effects of the external magnetic field on the o-p conversion, which acquired much attention and was reviewed in the article by Ilisca [10]. After publication of the review article, theory for the magnetic-field effect was developed in terms of the efficiency of the o-p energy transfer into the electronic system [15, 16].

On the basis of Eq. 23, Motizuki and co-workers calculated the probabilities of the o-p conversion of H_2 and p-o conversion of D_2 when the molecules are solidified by taking account of the phonon density of states [149, 139]. The perturbation Hamiltonian was expanded in powers of the displacement of the molecule center of mass, which allowed evaluation of the phonon emission/absorption matrix elements. By treating the lattice vibration within the Debye approximation and calculating the phonon density of states, the o-p transition probability was obtained, which corresponds to the o-p energy dissipation into the lattice phonon. The calculated conversion rate for H_2 was 1.9 % per hour [149], which was in good agreement with the experimental results [150]. The experimental p-o conversion rate of D_2, on the other hand,

is 5.5×10^{-4} /h [151, 152]. The theoretical study showed that the conversion rate due to the magnetic dipole interaction is the same order as the rate due to the quadrupole interaction [139].

In a high pressure condition, the phonon density of states of solid hydrogen changes as compared to those at low pressures, and the rotational sublevel splitting is caused by the anisotropic potential due to the electric quadrupole–quadrupole interaction [3]. These effects modify the energy dissipation channel significantly influencing the conversion rate [153, 154, 155, 156, 157]. The dependence of the conversion probability on the magnetic sublevel is discussed in relation to the NMR spectrum [158].

When H_2 is in a fixed position with a distance of a from a paramagnetic spin, the o-p conversion rate is expected to be proportional to $|\langle p|H'|o\rangle|^2 \propto a^{-8}$ in contrast to the Wigner law of a^{-6} where H_2 is assumed to move across the interaction region of a paramagnetic impurity. This was recently confirmed by a sophisticated experiment for H_2 encapsulated in C_{60} [159]. Figure 17(a) shows a schematic of their samples. A paramagnetic spin catalyst was covalently linked to C_{60} with spacer molecules (distance a) between the encapsulated H_2 and the paramagnetic molecule. For various spacer distances, the para to ortho conversion time was measured at room temperature with NMR after thermalized at 77 K, which showed a clear a^{-8} dependence of the conversion time as shown in Fig. 17(b) [159]. The interaction time was treated by the coherence time of the impurity spin [146].

For the physisorbed H_2, Yucel calculated the o-p conversion probability by taking account of the two-dimensional phonon of the adsorbed H_2 layer as the o-p energy dissipation channel [21]. As the perturbation, the magnetic dipole, Fermi contact and orbital motion of metal surface electrons were considered. The calculated conversion time is shown in Fig. 18 as a function of the H_2-surface distance. Here, the surface was assumed to be diamagnetic without any paramagnetic ions. This study was motivated by the experimental findings of possible o-p conversion on diamagnetic metal surfaces of Cu and Ag as detailed below. Although the surface is diamagnetic, the magnetic dipole and Fermi contact interaction become significant due to thermal fluctuation of the metal electron.

3.4. Second-order perturbation

When H_2 is in a physisorption well, the second-order perturbation can also be important as well as the first-order term. This was first proposed by Ilisca and Sugano [160, 161], who recognized the experimentally observed

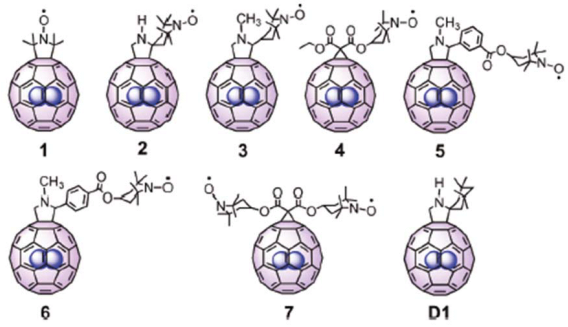

[a]Blue balls indicate a mixture of encapsulated H_2 and HD.

(a)

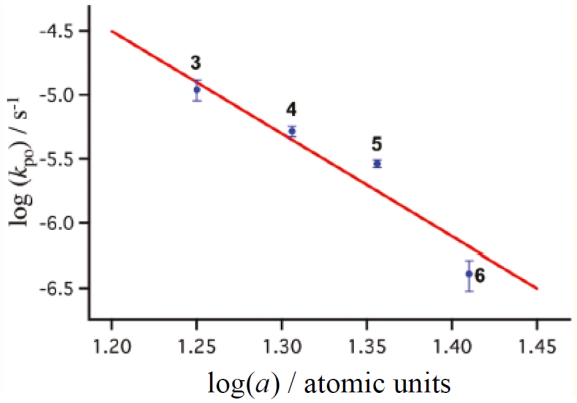

(b)

Figure 17: (a) Schematic illustration of H_2 encapsulated in C_{60}. A paramagnetic molecule of NO is linked to C_{60} at a distance of a with various spacer molecules. (b) Para to ortho conversion rate of H_2 in C_{60} induced by the paramagnetic molecule at room temperature. The conversion rate is shown to be proportional to a^{-8}. Adapted by permission from [159].

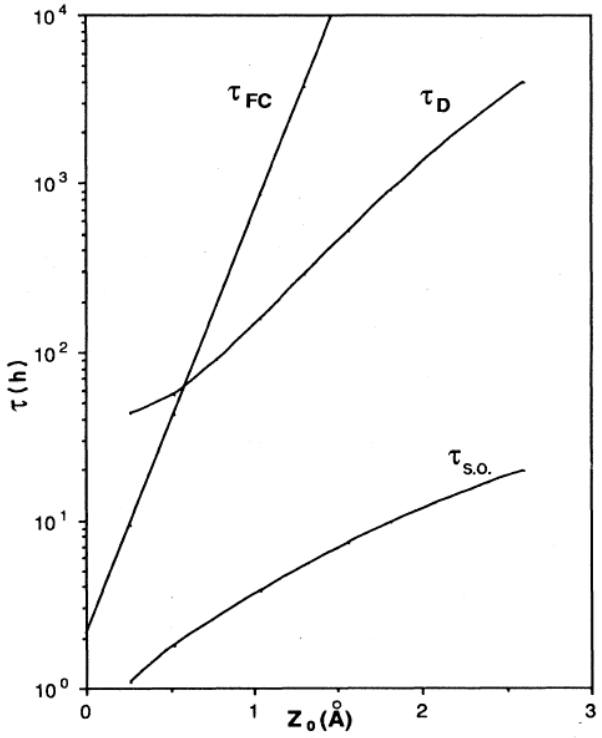

Figure 18: The ortho-para conversion times as a function of the metal-molecule distance z_0 on a Cu surface for different processes of the magnetic dipole (τ_D), Fermi contact (τ_{FC}) and electron motion (τ_{SO}) calculated by Yucel. Reproduced by permission from [21].

conversion rate on oxide surfaces was around two orders of magnitude larger than the value estimated on the basis of the first-order perturbation. According to the perturbation theory, the second-order transition probability via intermediate states is expressed as [136]

$$P = \frac{2\pi}{\hbar} |\sum_I \frac{\langle f|H'|I\rangle\langle I|H'|i\rangle}{E_i - E_I}|^2 J(E_f = E_i). \tag{24}$$

Ilisca and Sugano considered two interactions: Coulomb interaction (H_C) expressed as Eq. 25 and Fermi contact interaction (H_{FC}) described by Eq. 17 as $H' = H_C + H_{FC}$.

$$H_C = \frac{e^2}{4\pi\epsilon}(\sum_i \sum_j \frac{Z_j}{|\vec{r_i} - \vec{R_j}|} + \sum_{i,j(i\neq j)} \frac{1}{|\vec{r_i} - \vec{r_j}|}). \tag{25}$$

Here, $\vec{r_i}$ and $\vec{R_j}$ represent the electron and nucleus positions including surfaces, and Z_j is the atomic number of the j nucleus. They showed that the o-p conversion occurs as a two-step process following eq. 24 where H_C virtually induces excitation to an electronically excited state of the H_2-surface complex and H_{FC} causes nuclear-spin flip through interaction of the electronic spin in the virtually excited state. Following the original paper by Ilisca and Sugano, this second-order process is called "two-step process" in this article.

Figure 19(a) schematically shows the electronic and spin state of the surface paramagnetic ion and hydrogen molecule in the o-p conversion process. The paramagnetic ion is shown to possess a spin 1/2, which does not lose any generality. Since the hydrogen molecule is physisorbed, the electronic state of the molecule is assumed to be retained. The $1s\sigma_g$ and $1s\sigma_u$ orbitals of H_2 are denoted by g and u in the figure. With the Coulomb interaction, an electron in the $1s\sigma_g$ orbital is excited to the surface and the electron in the surface is excited to $1s\sigma_u$ while the total electron spin of the system is kept at 1/2. This corresponds to excitation of the molecule to the first excited state of $b^3\Sigma_u^+$ in the intermediate state. Because the orbital wavefunction of the $b^3\Sigma_u^+$ is ungerade, the matrix element between the initial and intermediate states has an antisymmetric character with respect to the permutation of the two nuclei as shown in Table 3. This leads to a selection rule of even-odd transition (ΔJ=odd) [160].

In the second step, on the other hand, the matrix element of the Fermi contact interaction over the intermediate $b^3\Sigma_u^+$ and final $X^1\Sigma_g^+$ states leads

to

$$\begin{aligned} \langle {}^3\Sigma_u^+ | H_{FC} | {}^1\Sigma_g^+ \rangle &= \lambda_{IFC} (\vec{s}_1 - \vec{s}_2) \cdot (\vec{i}_a - \vec{i}_b) \\ \lambda_{IFC} &= \int \phi_{1s\sigma_g}(\vec{r}) \delta(\vec{r} - \vec{R}_a) \phi_{1s\sigma_u}(\vec{r}) d\vec{r}. \end{aligned} \tag{26}$$

Here, the coefficient λ_{IFC} is described by the integration over the molecular orbitals (see Appendix B), therefore this is called the intra-molecular Fermi contact interaction. As discussed in Sec. 3.2, the spin difference operator mixes the spin triplet and singlet states, which means that the electron spin triplet and nuclear-spin triplet state can be mixed with the electron spin singlet and nuclear-spin singlet state. As an overall process, $\Delta J = 1$ in the first step and $\Delta I = 1$ in the second step results in o-p conversion, which is schematically shown in Fig. 19(a). This overall process is labeled the XY process [160]. It should be noted that the o-p conversion is significant only when H_2 is virtually excited to $b^3\Sigma_u^+$ through interaction with surfaces although the Fermi contact coupling is intramolecular.

An intriguing outcome of this study was that the proposed concept could also be applied to diamagnetic metals [162, 22, 163]. Figure 19(b) shows the electronic state from the initial to final states in the case of a diamagnetic metal, where the surface electrons form a singlet state in the initial state. In the intermediate state, the surface electrons form a triplet state along with the transition of the molecule state from ${}^1\Sigma_g^+$ to ${}^3\Sigma_u^+$ while the total spin of the system is kept at 0. Note ΔJ =odd in this first step. In the second step, the molecule undergoes the transition from the triplet to singlet states for both electrons and nuclei implying o-p conversion.

An extended version of this model was also proposed by considering another intermediate state, which is shown in Fig. 19(c) [22]. Here, the intermediate state is assumed to be a charge-transferred state, where H_2 forms a negative ion with an additional electron in the $1\sigma_u$ orbital. In the second step from the intermediate to final states in the figure, the molecule undergoes nuclear-spin conversion while the electron spin flips as it goes back to the surface through the Fermi contact interaction. The electron configurations of the intermediate ($|{}^1I\rangle$) and final ($|{}^3f\rangle$) states are expressed by $(1s\sigma_u)^1(k)^1$ and $(k)^1(k')^1$, respectively, with the substrate states of k and k', and the orbital integration $\langle {}^3f | H_{FC} | {}^1I \rangle$ has a spin antisymmetric component of $\lambda_{SFC}(\vec{s}_1 - \vec{s}_2) \cdot (\vec{i}_a - \vec{i}_b)$ (see Appendix B). This was labeled the UY process [22]. It should be noted that the electrons relevant to the Fermi

contact interaction in this process are not exclusively those in the molecule, implying that the interaction is not an intramolecular one. There are image charge states on metal surfaces, which are furthermore shown to enhance the electron transfer thereby accelerating o-p conversion [164].

The conversion times calculated on the basis of these models are shown in Fig. 20 in comparison to those calculated in the first-order (one-step) processes, which obviously shows that the two-step models of XY and UY are more effective than the one-step mechanisms [22].

The electron transfer between H_2 and the substrate and the magnetic dipole and direct Fermi contact interactions are obviously dependent on the molecule orientation as well as the molecule distance from the surface as intuitively understood in Fig. 8. Dependence of the o-p conversion on the molecular orientation was theoretically examined on the basis of the one-step process via the direct Fermi contact [165, 166] and two-step processes for the system of paramagnetic impurities adsorbed on a surface [167, 168, 169, 170] and metal surfaces [171, 172]. It was shown that the o-p conversion is more efficient when the molecular axis is aligned along the surface normal direction. This indicates that the M=0 state of J=1, which is often designated the cartwheel-like rotation, is preferred for the o-p conversion compared to the $M = \pm 1$ states designated the helicopter-like rotation. When the adsorption potential is anisotropic, the energy level is split depending on M as shown in Fig. 9. When $V_2 < 0$, H_2 molecules tend to occupy the $M = 0$ state because the energy level is lower, then the o-p conversion would be enhanced as compared with the case of an isotropic potential [173]. When the anisotropic potential is larger and the rotational motion is expressed by the hindered rotation, the orientational dependence will be more pronounced because of the distortion of the rotational wavefunction.

3.5. Higher-order perturbation

Although the theory based on the second-order perturbation was successful, this concept may not be straightforwardly applied to diamagnetic insulators. In Fig. 19(b) and (c), the final state of the substrate is an electron spin triplet state. If the substrate were a diamagnetic insulator, transition to the triplet state requires a band-gap energy, which is much larger than the o-p energy. This problem was shown to be circumvented by considering further higher-order perturbation including the Stark coupling and spin-orbit coupling [33], which is called a multi-step process in analogy with the two-step process.

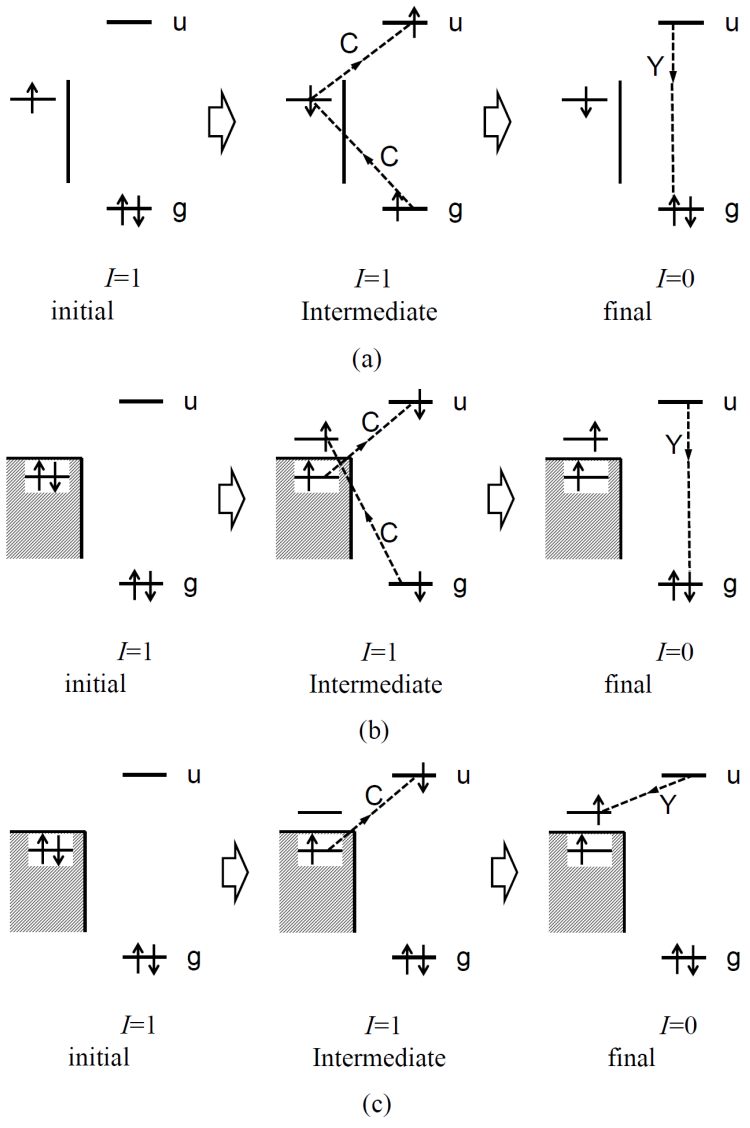

Figure 19: Schematic illustration of the electronic excitation for the two-step o-p conversion model. From left to right, the initial, intermediate and final electronic states are shown, each consisting of the substrate and H_2 electronic levels. (a) XY process on a paramagnetic surface, (b) XY process on a diamagnetic metal, and (c) UY process on a diamagnetic metal. The initial o-H_2 (I=1) undergoes charge exchange with surfaces labeled C in the first step from the initial to intermediate state, and in the second step nuclear-spin conversion of $I = 1 \rightarrow I = 0$ through the Fermi contact interaction labeled Y.

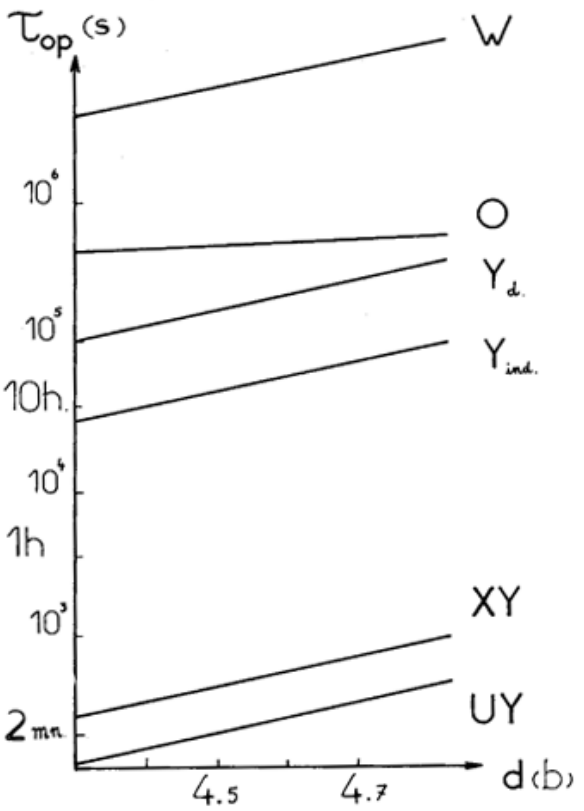

Figure 20: The ortho-para conversion times as a function of the metal-molecule distance d (a. u.) for different processes on the basis of one-step (O: electron motion, W: magnetic dipole, Y_d: direct Fermi contact, and Y_{ind}: indirect Fermi contact via molecular orbitals) and two-step (UY and XY) processes calculated for an Ag surface by Ilisca. Reproduced by permission from [22].

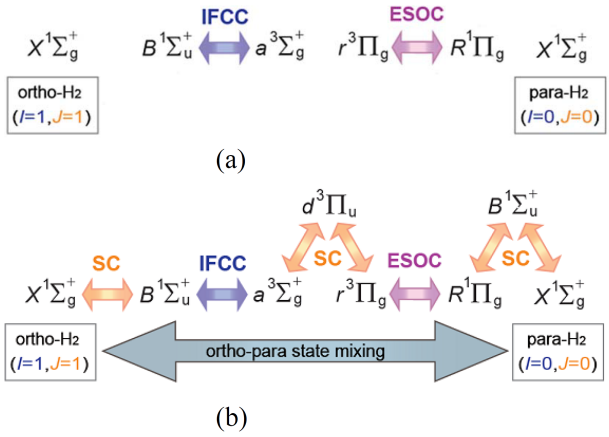

Figure 21: Schematic illustration of mixing between o-H_2 and p-H_2 in the multi-step process. (a) Intrinsic mixing of $a^3\Sigma_g^+$ and $B^1\Sigma_u^+$ with intramolecular Fermi contact interaction, and enhanced spin-orbit coupling between $^3\Pi$ and $^1\Pi$. (b) Stark mixing between the gerade and ungerade states due to intense surface electric fields leads to an overall mixing between o-H_2 and p-H_2.

Figure 21(a) shows the excited states of H_2 relevant to such a multi-step process. As discussed in the two-step process, the intramolecular Fermi contact interaction mixes the $^3\Sigma_u^+$ of o-H_2 and $^1\Sigma_g^+$ of p-H_2 (or vice versa). This also holds in the case of $^3\Sigma_g^+$ and $^1\Sigma_u^+$. Since the energy levels of $a^3\Sigma_g^+$ and $B^1\Sigma_u^+$ are closer than those of $b^3\Sigma_u^+$ and $X^1\Sigma_g^+$, the mixing coefficient is larger for $a^3\Sigma_g^+$ and $B^1\Sigma_u^+$ [174].

Another intramolecular interaction to be considered is spin-orbit coupling between $^3\Pi$ and $^1\Pi$ with the same electron configuration as shown in Fig. 22(a). The spin-orbit interaction Hamiltonian for a hydrogen molecule with two electrons is described as

$$H_{SOC} = \xi(\ell_1^z s_1^z + \ell_2^z s_2^z) \tag{27}$$

where ℓ_i^z and s_i^z denote the axial components of the angular momentum and spin of i electron, respectively, and ξ represents the spin-orbit coupling coefficient. Note that only the axial component of the electron angular momentum is well-defined in the diatomic molecule. This perturbation allows mixing between the total electron spin (S) singlet and triplet states with a selection rule of ΔS=1 as detailed in Appendix C. The mixing coefficient is described as $\langle ^3\Pi|H_{SOC}|^1\Pi\rangle/\delta_{t-s}$ with the energy difference δ_{t-s} between the $^3\Pi$ and $^1\Pi$

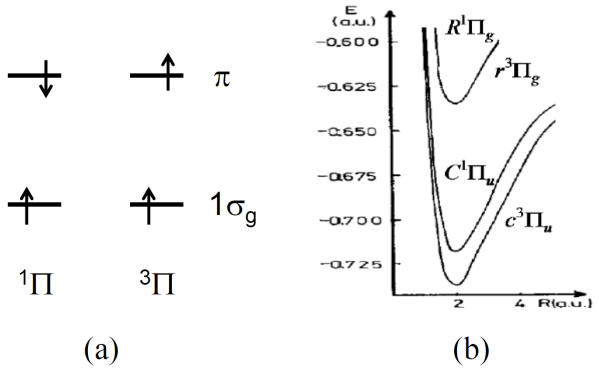

Figure 22: (a) Electron configuration of $^1\Pi$ and $^3\Pi$ states. (b) Adiabatic potentials for $c^3\Pi$ and $C^1\Pi$ for $(1s\sigma_g)(2p\pi_u)$, and $r^3\Pi$ and $R^1\Pi$ for $(1s\sigma_g)(4d\pi_g)$. The r and R states are energetically almost degenerate due to weak electron exchange-correlation.

states. This indicates that the mixing is larger as δ_{t-s} gets smaller.

The δ_{t-s} value is essentially determined by the Coulomb repulsion of the two electrons. In a high Rydberg state where the electron orbital has an extended feature, δ_{t-s} is expected to be small, i.e. weak electron exchange-correlation enhances the spin-orbit coupling. As shown in Fig. 22(b), the adiabatic potentials of the $r^3\Pi_g$ and $R^1\Pi_g$ states are almost degenerate with an energy difference of $\sim$0.1 meV [175, 176]. Although the spin-orbit interaction strength is small for light elements like H, the mixing can be significant in highly excited states due to the small energy difference.

These mixing properties are schematically shown in Fig. 21(a). The mixing of $a^3\Sigma_g^+$ and $B^1\Sigma_u^+$ with IFC and $r^3\Pi_g$ and $R^1\Pi_g$ with SOC is an inherent property of the molecule. Nevertheless, the o-p conversion is not induced without external perturbation because the ground state $X^1\Sigma_g^+$ is not mixed with the relevant excited states.

When H_2 is under an electric field, there occurs Stark coupling between the electronically excited states of H_2. The perturbation Hamiltonian (H_S) is equivalent to Eq. 9. The matrix element of this perturbation is non-zero between gerade and ungerade states. Simultaneously, the molecular rotational states of even and odd are mixed as the Coulomb interaction in the two-step process. This situation is displayed in Fig. 21(b), where the ortho and para states are mixed via intrinsically coupled B – a and r –R states. The overall selection rule becomes $\Delta S = 0$, $\Delta J = 1$, and $\Delta I = 1$,

and o-p conversion can be an allowed process [33].

3.6. Isotope effect

The isotopes of H_2 and D_2 have particular differences for the nuclear-spin conversions. This section summarizes the key factors governing the isotope dependence of the nuclear-spin conversion. While the electronic structure of H_2 and D_2 is essentially the same, the nuclei of proton and deuteron have different masses, nuclear spins, nuclear g factors, and nuclear quadrupole moments as shown in Table 4.

The mass difference leads to the difference in the rotational and vibrational energies. Whereas the rotational energy is different by a factor of 2, the difference in the vibrational energy is $\sqrt{2}$. For the nuclear-spin conversion, the rotational-energy has to be dissipated into other degrees of freedom. Since the rotational energy of D_2 is smaller than that of H_2, the rotational-energy dissipation of D_2 might be more efficient than H_2 (Sec. 5.1.2). For the conversion of solid hydrogen, in fact, the rotational energy of D_2 is considered to be dissipated into the phonon system as a one-phonon process, whereas that of H_2 requires two-phonon creation [149, 139]. In addition to the efficiency of the rotational-energy dissipation, the rovibrational energy is important for the level matching. In the two-step and multi-step conversion processes discussed in Secs. 3.4 and 3.5, intra-molecular coupling in the excited state is important, and the coupling strength is enhanced when the energy levels of the relevant states are near-degenerate. On the same adiabatic potential, the level matching might be different between H_2 and D_2 because of the difference in the rovibrational energy.

The nuclear g factor, on the other hand, affects the magnetic interaction. As shown in Eqs. 15 and 17, the magnetic interaction Hamiltonian is proportional to the nuclear g factor (g_n), which is a common feature for both the magnetic dipole and Fermi contact interaction. Since the total nuclear-spin quantum number is different for H_2 and D_2, the degeneracy of the initial and final states in the nuclear-spin conversion is different for the two molecules as detailed in Figs. 3 and 4. The matrix element between the initial and final states, furthermore, depends on the spin quantum number and the z component of the spin. The square of the matrix element, when averaged over the initial states and summed over the final states, is calculated to be proportional to $\frac{g_n^2}{3}$ and $2g_n^2$ for H_2 and D_2, respectively, reflecting the initial and final state degeneracy [21]. Considering g_n= 5.59 for proton and 0.857 for deuteron, both magnetic dipole and hyperfine contact interactions are

larger for H_2 than D_2 by a factor of 7.1, and the conversion time is expected to be shorter for H_2. In addition to the magnetic g factor, the quadrupole interaction is significant for D_2 as deuteron has a non-zero quadrupole moment.

When intermolecular interaction is significant, the magnetic field due to the nuclear spin and rotational moment of molecules contributes to the magnetic interaction. While o-H_2 ($I = 1, J = 1$) has both nuclear-spin and rotational moments, p-H_2 ($I = 0, J = 0$) has no magnetic moments. On the other hand, both p-D_2 ($I = 1, J = 1$) and o-D_2 ($I = 2, J = 0$) contribute to the magnetic dipole interaction. This difference leads to the difference of the conversion kinetics: the H_2 o-p conversion follows the second-order kinetics, while the D_2 p-o conversion is expressed by the first-order kinetics as demonstrated for solid hydrogen where the intermolecular magnetic interaction is responsible [149, 139].

4. Surface-sensitive experimental technique

The experimental technique that is capable of distinguishing o-H_2 and p-H_2 is classified into two classes, one probing the nuclear spin of H_2 and the other probing the rotational state of H_2. The only technique of the former class is the nuclear magnetic resonance (NMR) [177]. While only o-H_2 with I=1 can be detected by NMR, the spin-lattice relaxation time is dependent on the ortho concentration in a H_2 solid [178, 179], which allows for estimation of the o-p ratio of samples. The problem at the present stage is its sensitivity: the number of hydrogen atoms on ordinary well-defined surfaces is 10^{15}, which is too small for the NMR measurement.

All other methods used for the distinction of the ortho and para species are based on the fact that the two species have different rotational states shown in Fig. 6. A traditional method used for o-p separation and conversion studies was the thermal conductivity measurement [1]. A wire in the measurement cell was heated to 100 – 180 K, and the wire resistance was measured at a certain H_2 gas pressure. Since the specific heat derived from the partition function of Eq. 5 is different between the ortho and para species, which is intuitively understood from the different rotational levels shown in Fig. 6, the thermal conductivity is different between the two species, and the resistance data gives the ortho concentration in the sample gas. This type of measurement can be performed with Pirani gauges. [180, 181]. A typical procedure of the experiments is as follows: H_2 gas is introduced in a

reaction chamber containing sample surfaces. From time to time, a part of the H_2 gas is extracted from the reaction chamber and introduced into the measurement cell, where the o-p ratio is evaluated by the thermal conductivity measurement. Here, a large amount of H_2 is required for the study and a large amount of surface area as the sample is necessary, which is not suited to the study on well-defined single-crystal surfaces.

As described in Eq. 3, the internal energy of molecular hydrogen originates from the electronic, vibrational and rotational degrees of freedom. Since there is coupling of the rotational motion with the vibrational and electronic states, rotational spectroscopy can be achieved by vibrational excitation and electronic excitation accompanied by ro-vibrational excitation as well as pure rotational excitation. As H_2 has no permanent electric dipole moment, pure rotational and vibrational spectroscopy can be carried out by inelastic scattering of light and particles, such as Raman scattering spectroscopy (Raman), Inelastic Neutron scattering spectroscopy (INS), and Electron energy loss spectroscopy (EELS). In a particular situation, induced infrared absorption spectroscopy (IRAS) can be used as exemplified below.

The schemes for rotational and vibrational excitations are schematically shown in Fig. 23(a) and (b), respectively, and the excitation energies for H_2 and D_2 are listed in Table 5. While ΔJ=2 transitions are observed in pure rotational excitation of Raman and EELS because of the total-nuclear-spin conservation, INS can probe ΔJ=1 excitation, because a neutron has a nuclear spin 1/2 and spin-flip scattering occurs through the nuclear force [182]. In the vibrational excitation, on the other hand, Δv=1 excitation is observed. Since the rotational constant depends slightly on the vibrational level because of the stretch of the mean intra-molecular distance, the excitation energy is different between the J states as schematically shown in Fig. 23(b), which allows us to distinguish ortho and para species. The excitation energy difference is, however, small as listed in Table 5, therefore the vibrational spectroscopy is achieved by Raman and induced IRAS with high resolution. In EELS, on the other hand, vibrational excitation accompanied by rotational excitation is observed, which distinguishes the ortho and para species.

As to the sensitivity, the scattering cross section of Raman and INS is small and the probing depth is long, hence these techniques are not suited to the study on well-defined surfaces. INS has been applied to bulk or powder/porous materials such as oxides [183, 77, 78], carbon [184, 185, 186], metal-organic framework [187] to date. Raman has also been applied to bulk

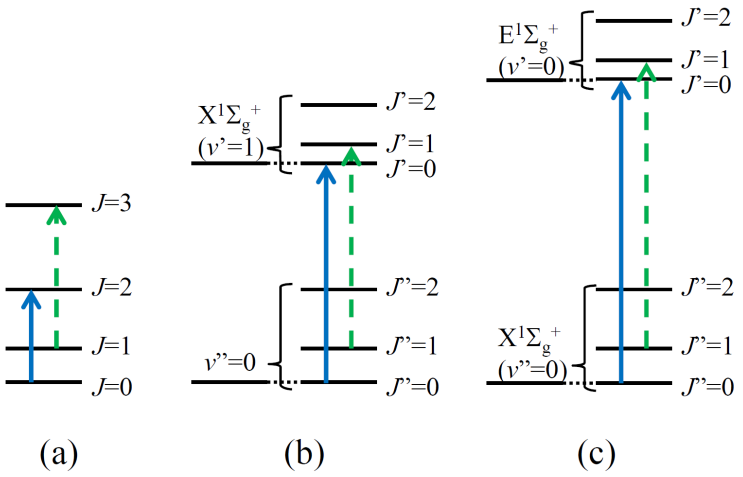

Figure 23: Schematic energy diagram of the rotational-energy levels in (a) the $X^1\Sigma_g^+$ state (v=0), (b) v=1 and 0 states of $X^1\Sigma_g^+$, and (c) $X^1\Sigma_g^+$ (v=0) and E,$F^1\Sigma_g^+$ (v=0) states. Solid (blue) and dashed (green) arrows denote excitations of the J=0 and J=1 states used in rotational-state spectroscopy. ΔJ=0 transitions are shown in (b) and (c). (c) is used for (2+1)REMPI (two-photon resonant excitation followed by one-photon ionization).

Table 5: Energy (meV) for pure rotational (J) and pure vibrational (v) excitations of H_2 and D_2 calculated by Eq. 3 using the constants listed in Tables 1 and 2. Wavelengths (μm) for corresponding photon energies are also shown in parentheses.

v	0 – 0		0 – 1	
J	0 – 2	1 – 3	0 –0	1–1
H_2	43.9	72.7	515.7	514.9
	(28.2)	(17.0)	(2.41)	(2.41)
D_2	22.2	36.9	370.9	370.7
	(55.9)	(33.6)	(3.34)	(3.35)

or powder/porous materials such as Si [188, 189], oxides [190] and carbon [191, 192, 193]. In EELS in a low-energy regime at a primary energy of 1–10 eV, electrons reflected from surfaces are detected after energy analysis. Hence, compared with the rather long probing depth of INS and Raman, EELS detects only surface-adsorbed molecules, which allows for rotational spectroscopy on well-defined surfaces. In the gas phase electron scattering experiments, it is known that there occurs a temporal negative-ion resonance at a primary electron energy of 3 eV, where the scattering cross section shows a maximum [194]. A similar resonance feature was also observed on the physisorbed H_2 [195], therefore, the EELS experiments for H_2 on surfaces have often been done at a primary energy of about 3 eV.

It should be noted that ΔJ=2 and Δv=1 radiative transitions are induced via the quadrupole moment of molecular hydrogen, which can be realized as infrared-light absorption and emission. Since the transition probability is small, however, IRAS due to the quadrupole transition is not utilized for detection of molecular hydrogen in laboratory experiments.

On solid surfaces, however, molecular hydrogen might be polarized particularly on ionic substrates owing to the strong electric field present on the surface. This induces a dipole moment in H_2, which causes infrared light absorption due to vibrational excitation as depicted in Fig. 23(b). This was observed on porous NaCl, ice and glass having a large surface area [196, 197, 198, 199, 94], and has been applied to porous and bulk materials such as carbon materials [200, 201, 202], Si [203], metal-organic framework [204, 205, 206], and oxides [207]. An experimental progress has enabled to probe o-H_2 and p-H_2 physisorbed on single-crystal surfaces [208, 209].

The other type of techniques capable of rotational-state-resolved measurements utilizes electronic excitation of molecules as shown in Fig. 23(c). Here, excitation to the E $^1\Sigma_g^+$ state is shown as an example. Similarly to the vibrational excitation in Fig. 23(b), the rotational constant in the E $^1\Sigma_g^+$ state is different from that in the $X^1\Sigma_g^+$ state as shown in Tables 1 and 2. Then, the excitation energy corresponding to the J=0 and J=1 molecules is slightly different, thereby allowing the rotational-state-resolved detection. Two experimental approaches to probe such electronically excited molecules are ionization and fluorescence, which are designated as resonance-enhanced multiphoton ionization (REMPI) and laser-induced fluorescence (LIF). The typically used resonant excitation is $X^1\Sigma_g^+ \rightarrow$ E,F $^1\Sigma_g^+$ and $X^1\Sigma_g^+ \rightarrow B^1\Sigma_u^+$. The excitation, ionization and fluorescence processes are shown by arrows in the adiabatic potential (Fig. 24).

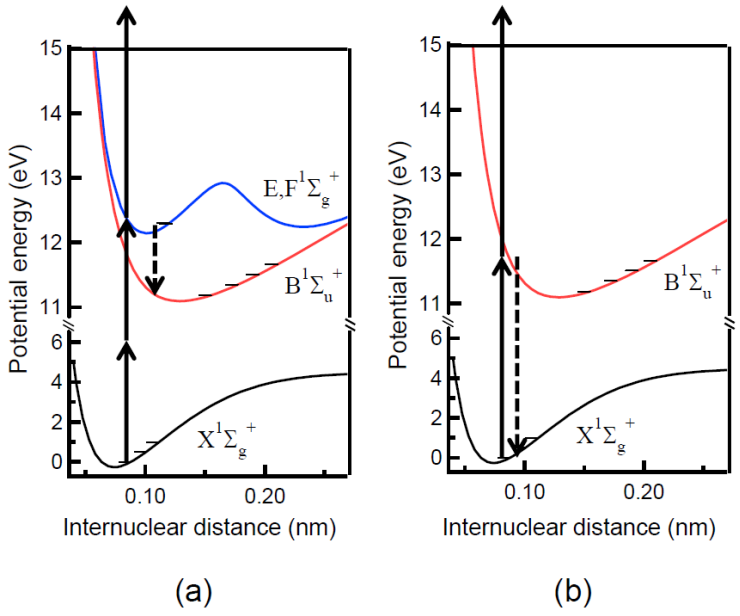

Figure 24: Resonant excitation, ionization and fluorescence processes used for REMPI and LIF. (a) Two-photon excitation to E,F $^1\Sigma_g^+$ and subsequent ionization are shown by solid arrows, whereas the dashed arrow denotes fluorescence due to E,F $^1\Sigma_g^+ \rightarrow$ B$^1\Sigma_u^+$. (b) One photon excitation to B$^1\Sigma_u^+$ and subsequent ionization are shown by solid arrows, and fluorescence due to deexcitation to X$^1\Sigma_g^+$ is denoted by the dashed arrow.

Due to the symmetry restriction, excitation to the E,F $^1\Sigma_g^+$ state by one-photon absorption is forbidden, and therefore can be achieved by two-photon absorption. In this excitation scheme, the selection rule for the rotational state is ΔJ=0, $\pm$2 [210, 211, 212]. On the other hand, the $B^1\Sigma_u^+$ state is accessible by a single-photon absorption due to its dipole-allowed nature with respect to the $X^1\Sigma_g^+$ ground state [213, 214], and the selection rule for the rotational state is ΔJ=$\pm$1.

The excited molecule in these E,F $^1\Sigma_g^+$ and $B^1\Sigma_u^+$ states can be ionized by absorption of another photon [210, 211, 212, 213, 214]. While fluorescence due to the $B^1\Sigma_u^+ \rightarrow X^1\Sigma_g^+$ transition is dipole-allowed [215], the E,F$^1\Sigma_g^+$ $\rightarrow X^1\Sigma_g^+$ transition is dipole-forbidden. However, the E,F$^1\Sigma_g^+$ state can be quenched through a dipole transition to the low-lying $B^1\Sigma_u^+$ state [216, 217, 218], and the rotational-state resolved E,F $\rightarrow$ B fluorescence was recently achieved [37, 219]. REMPI and LIF have been applied to dynamics studies of hydrogen on surfaces as reviewed in Refs. [220, 221, 222].

A typical LIF data via the E state taken for H_2 at 300 K is shown in Fig. 25. Four distinct maxima are observed in the excitation wavelength range of about 202 nm. By comparing the energy levels for the X and E states calculated following Eq. 3, these maxima are assigned to the J=0, 1, 2, and 3 states.

The REMPI and LIF are essentially gas-phase spectroscopic techniques. REMPI can actually detect H_2 in the pressure range as low as 10^{-8} Pa. However, both techniques have not been directly applied to H_2 physisorbed on a surface, because the electronic level of H_2 is modified and substantially broadened in a physisorption well, which hampers the resonant excitation in an internal-state-resolved manner.

To compromise this situation, the REMPI technique was combined with desorption methods where adsorbed H_2 was desorbed from the surface followed by REMPI detection. Two desorption schemes were applied, photo-stimulated desorption (PSD) [25, 223, 224, 225], and TPD [26, 33, 226]. The experimental setup of our group is schematically shown in Fig. 26. Well-defined sample surfaces prepared in UHV are exposed to H_2 or D_2, and REMPI detects molecules upon TPD or PSD with another laser beam of 2.3 – 6.4 eV (not shown). An important factor for this experiment is the desorption probability of the ortho and para species. Figure 27 shows the time of flight spectra of H_2 photodesorbed from Ag, which was obtained by changing the delay time of the REMPI laser from the pump desorption laser [25]. The spectra of $J = 1$ and $J = 0$ both reveal a maximum at a time

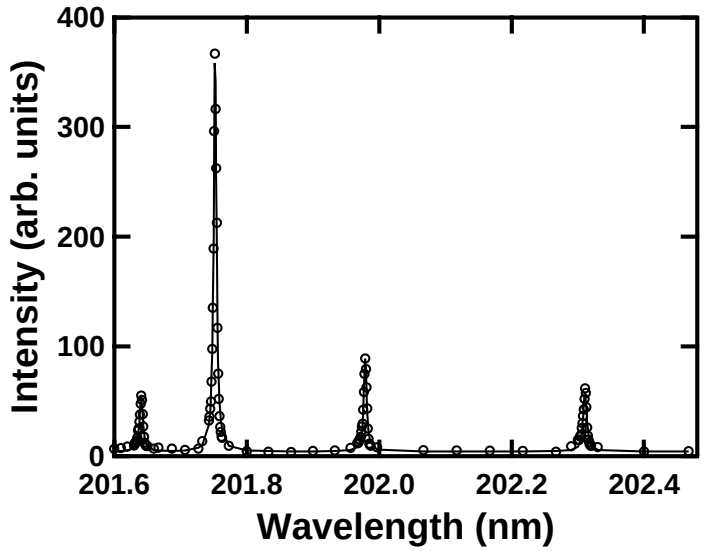

Figure 25: Typical LIF data measured for H_2 via the X $\rightarrow$ E two-photon excitation followed by fluorescence via E,F $\rightarrow$ B [37]. The fluorescence intensity is plotted as a function of the excitation laser wavelength, and the four maxima correspond to resonant excitation of H_2 in the J=0, 1, 2, and 3 states.

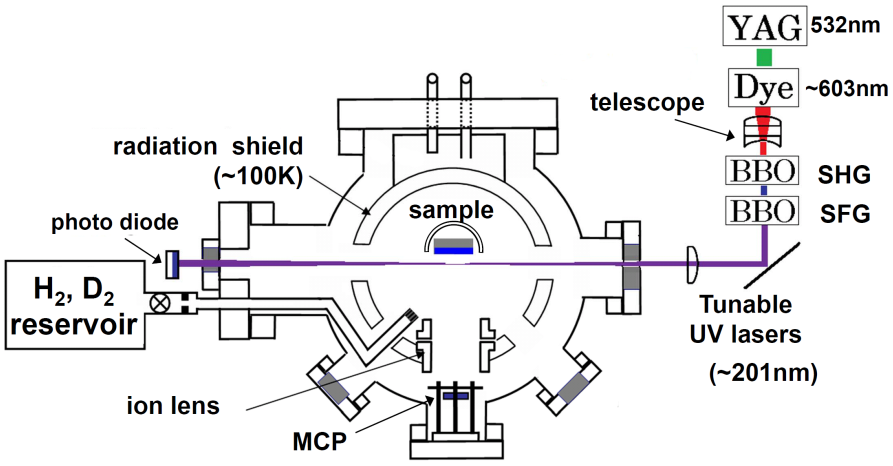

Figure 26: Schematic illustration of the experimental setup for REMPI detection used in the group of University of Tokyo. The molecules either photodesorbed or thermally desorbed from the sample surface are ionized with the REMPI laser focused in front of the sample, and detected by a microchannel plate (MCP) through an ion lens. Tunable laser light for (2+1) REMPI via E at ∼201 nm is generated by second-harmonic generation (SHG) and sum-frequency generation (SFG) of YAG-pumped dye laser at ∼603 nm (line width: 0.15 cm^{-1}).

of flight of 22 μs. It was argued that the desorption mechanism is the same independent of the rotational state, thus the desorption intensities probed by REMPI-PSD are expected to be proportional to the H_2 coverages on surfaces [25, 223]. Figure 28 shows typical REMPI-TPD results [33]: thermally desorbed H_2 was rotational-state selectively measured during sample heating, which corresponds to the sample temperature of 10 – 30 K. By integrating the desorption signals, the coverage of the ortho and para hydrogen can be estimated. In the PSD method, only a small portion of adsorbed H_2 is photodesorbed followed by REMPI detection, which allows coverage estimation of the ortho and para species in real time. In the TPD method, on the other hand, the total amount of adsorbed H_2 is thermally desorbed from surfaces, hence repreparation of the sample is necessary to examine the time evolution of the ortho and para coverages.

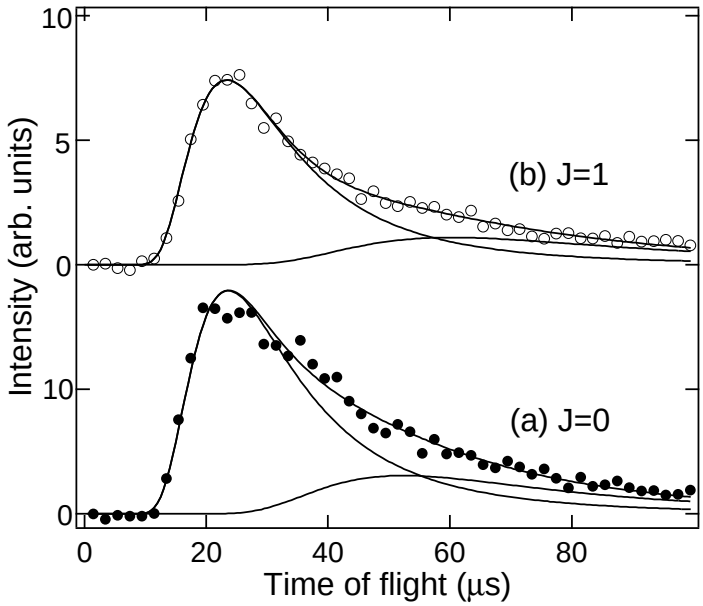

Figure 27: Time of flight spectra of H_2 in (a) $J = 0$ and (b) $J = 1$ states photodesorbed from an Ag surface at a pump laser wavelength of 193 nm (6.4 eV) as measured by REMPI-PSD. The spectra were collected by varying the delay of the probe REMPI laser pulse from the pump desorption laser. The solid curves denote fits with the Maxwell-Boltzmann distribution. Reproduced by permission from [25].

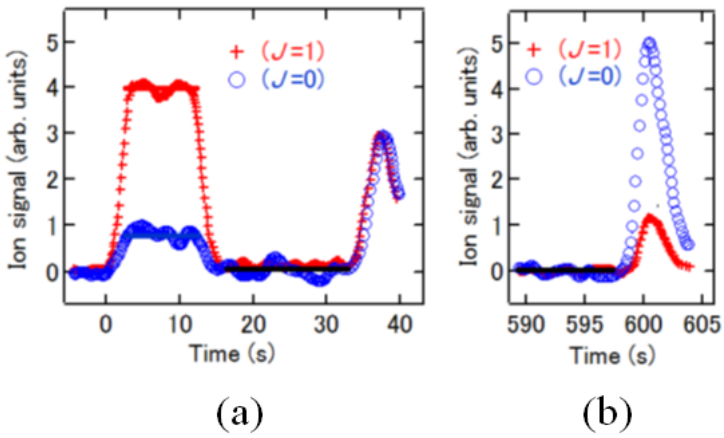

Figure 28: REMPI signals for H_2 during adsorption and desorption from amorphous ice surfaces in the $J = 0$ (blue open circle) and $J = 1$ (red cross) states. (a) n-H_2 was introduced at a pressure of 1.5×10^{-7} Pa into the chamber at t= 0 – 14 s, and subsequently the sample temperature was raised from t= 35 – 40 s. (b) the sample temperature was raised at t= 598 s after the n-H_2 dosage. Adapted by permission from [33].

5. Physisorption and ortho-para conversion on various surfaces: experimental studies

When hydrogen molecules are physisorbed on a surface, as shown in Fig. 9, the molecule is trapped in the well with a binding energy of about 30 meV, which is realized at a low temperature of about 10 K, and the rotational level is split due to the potential anisotropy. At this low temperature, all o-H_2 (p-D_2) molecules are in the ground state of the J=1 state, while all p-H_2 (o-D_2) molecules are in the J=0 state. While trapped in the physisorption well, o-H_2 (p-D_2) interacts with the electronic and nuclear (phonon and spin) systems of surfaces and neighboring molecules, and undergoes o-p (p-o) conversion relaxing to the J=0 state of p-H_2 (o-D_2), which is accompanied by the nuclear spin flip (ΔI=1) and rotational-state transition (ΔJ=1). The questions on the conversion mechanism are (1) the origin of the perturbation and (2) the energy dissipation channel. As described in Sec. 3, possible origins of the magnetic interaction are the magnetic dipole, external and internal Fermi contact and electron motion. In combination with these interactions, electron Coulomb interaction, Stark and Spin-orbit interaction may be taken into consideration when two- or multi-step processes are considered. On vari-

ous surfaces, the origin of the perturbation has been discussed on the basis of surface electronic properties. On the other hand, possible energy dissipation channels are the substrate phonon/electron, overlayer H_2 phonon, localized H_2 vibration in the z direction, kinetic energy in the parallel direction (surface diffusion), and magnon. While theoretical studies examine the energy dissipation channel so as to fit the experimental conversion time as exemplified for solid H_2 [149, 154, 157], little experimental information has been reported on the energy dissipation mechanism, which should be the subject in the future.

As introduced in Sec. 4, EELS and REMPI studies have clarified the physisorption and o-p conversion of hydrogen mainly on clean and impurity-adsorbed diamagnetic surfaces. The experimental studies on these surfaces are reviewed in this section. As compared to diamagnetic surfaces, fewer papers have been published on well-defined magnetic surfaces prepared in UHV with an exception of $Cr_2O_3(0001)$ [227], although a number of studies by using traditional methods were reported on the o-p conversion on magnetic materials until 60's, which are comprehensively reviewed by Ilisca [10]. One reason for this might be that the conversion mechanism was believed to be understood by the Wigner model. Nevertheless, the surface magnetic structure of magnetic materials has only been clarified by the recently developed surface-sensitive probes such as spin-polarized photoemission, spin-polarized STM, magnetic circular dichroism, spin-polarized LEEM and grazing-incidence nuclear resonant scattering. Therefore, the o-p conversion on various spin structures will be an interesting subject in the future.

5.1. Diamagnetic metal surface

5.1.1. Clean Cu surface

Andersson and Harris performed EELS experiments for H_2, D_2 and HD physisorbed on a single-crystal Cu(100) surface, and succeeded in observing the rotational and ro-vibrational excitation of molecular hydrogen [18]. The Cu(100) surface was cleaned by surface-science-based techniques in UHV, and exposed to normal H_2, D_2 or HD at 12 K. Figure 29 shows the EELS spectra taken for H_2, HD and D_2 at several experimental conditions. Taking account of the EELS cross section, the adsorbed hydrogen was considered to be in a monolayer regime. In the EELS spectra, in addition to the substrate Cu phonon at 28 meV (later assigned to contamination of water), loss features were observed at 45 and 72 meV for H_2, 22 meV and 37 meV for D_2, and 33 meV for HD. The features for H_2 were assigned to the transitions of J=0 $\rightarrow$

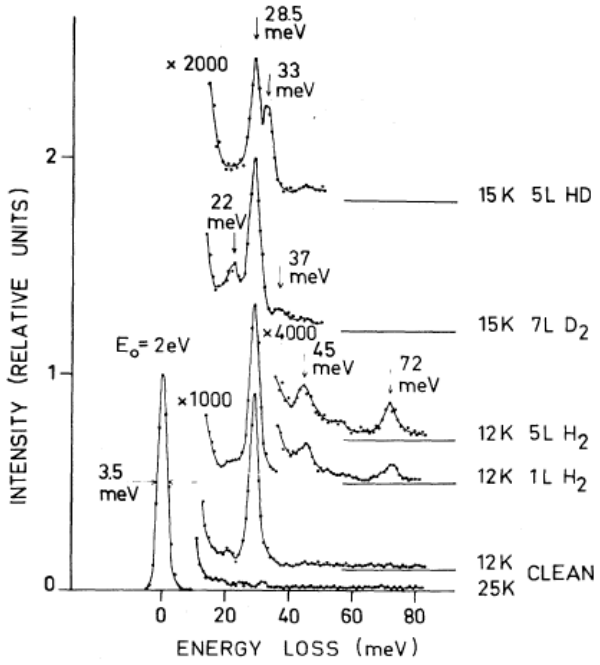

Figure 29: EELS spectra for H_2, HD and D_2 physisorbed on Cu(100) at low temperature. In addition to the elastic peak at a loss energy of 0 eV, loss features due to rotational excitation are observed at 45 meV (J=0→2) and 72 meV (J=1→3) for H_2, 22 meV (J=0→2) and 37 meV (J=1→3) for D_2, and 33 meV (J=0→2) for HD. Reproduced by permission from [18].

2 of p-H_2 and J=1 → 3 of o-H_2. Furthermore, vibrational excitations of v=0 → 1 were recognized at around 500 meV for H_2 and 350 meV for D_2 as shown in Fig. 30. In addition to the pure vibrational excitation at 518 meV for H_2 and 372 meV for D_2, combined excitations of vibration and rotation were also observed in the spectra. It is noted that the ortho and para species were not resolved in the pure vibrational excitation peak because the difference of the vibrational excitation energy between the ortho and para H_2 is smaller than the EELS resolution (Fig. 23(b) and Table 5).

The rotational excitation energies observed by EELS are close to the gas phase values (Table 5). If the potential is anisotropic, the rotational level degeneracy is lifted as discussed in Fig. 9, which is reflected in the EELS spectrum. Svensson and Andersson analyzed the spectral shape of the J=0 → 2 feature in detail to decompose it into two components as shown in

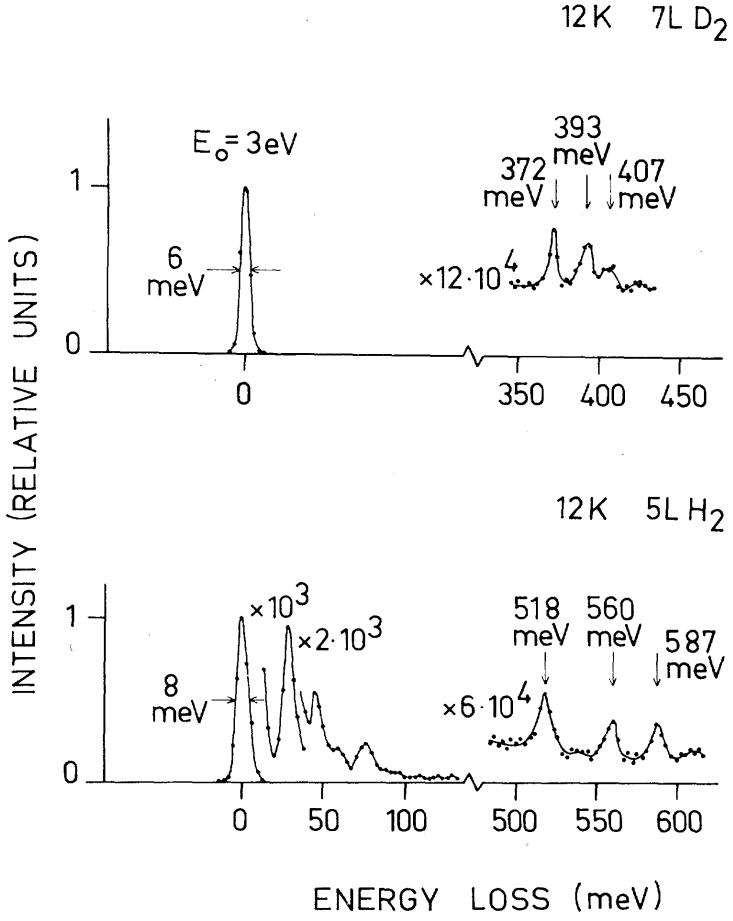

Figure 30: EELS spectra for H_2 and D_2 physisorbed on Cu(100) in the loss energy range for vibrational excitation. Loss features are observed at 518 (v=0→1), 560 ((v=0→1)+(J=0→2)), and 587 meV ((v=0→1)+(J=1→3)) for H_2, and 372 (v=0→1), 393 ((v=0→1)+(J=0→2)), and 407 meV ((v=0→1)+(J=1→3)) for D_2. Reproduced by permission from [18].

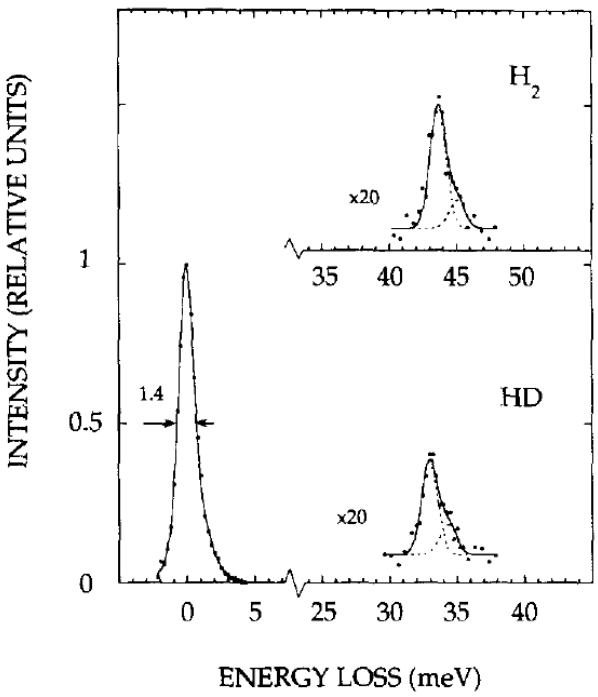

Figure 31: Analysis of the EELS spectra for H_2 and HD physisorbed on Cu(100). The loss peaks at 45 and 33 meV (J=0→2) are decomposed into two components corresponding to the rotational sublevels of $M = \pm 2$ and $M = 0$ in $J = 2$. Reproduced by permission from [73].

Fig. 31, which were ascribed to excitation to the (J=2, M=0) and (J=2, M=±2) states [73], the latter being more stable. From the obtained values, the anisotropic potential was evaluated to be +1.4 meV.

The EELS results definitely showed that both ortho and para species are present on the surface. The observed intensity ratio of the loss features corresponding to ortho and para H_2 obviously deviates from the gas-phase degeneracy of 3. This was initially attributed to the J-dependent sticking probability [99]. Nevertheless, the J-dependence of the sticking probability was later found to be small by a molecular-beam resonant sticking study [100, 53] and theoretical studies [104, 103]. The other point that should be clarified is the EELS cross section. The EELS cross section for the ortho and para H_2 was examined in detail by changing the relative coverage of ortho and para hydrogen on Cu(001) [73]. The cross section difference was then

not sufficient to explain the deviation of the J=1/J=0 intensity ratio from 3 observed in EELS. Therefore, it was concluded that o-p conversion takes place on the Cu(001) surface.

In the first publication by Andersson's group, it was reported that the intensity ratio corresponding to J=1 and J=0 does not change on the experimental timescale suggesting that the o-p conversion rate is smaller than 1 %/min. In a later publication, on the other hand, the conversion time scale is reported to be 1 ML in 5 min [73]. They suspected that some unidentified non-controllable active sites for o-p conversion are present on the surface.

In recent work, Svensson and Andersson investigated o-p conversion of H_2 on a stepped Cu(510) surface and compared with a flat surface of Cu(100) [228]. Figure 32 shows the EELS spectra taken for H_2 adsorbed on Cu(510) at different temperatures and H_2 background pressures. On this stepped surface, two adsorption states are clearly present as identified by the EELS features at 31 and 46 meV in Fig. 32(a). These loss features were attributed to the J=0 $\rightarrow$ 2 transition of p-H_2 in a strongly hindered-rotor state at a step site and nearly-free-rotor state at a flat terrace [59, 60]. Excitations corresponding to o-H_2 in the two rotor states are also observed at 61 and 79 meV in Fig. 32(b). Although they are designated 2D and 3D rotor states in the paper, respectively, we call them hindered-rotor and nearly-free-rotor in this article as mentioned in Sec. 2.2.1.

As seen in Fig. 32(b), the loss intensity of o-H_2 was enhanced as the temperature and H_2 pressure were increased. By assuming that adsorption from gas phase, desorption from the specific site of the surface and o-p conversion were in equilibrium, the o-p conversion time of H_2 at the step site was estimated to be as short as 1 s. Compared with a flat terrace, H_2 at a step site is more strongly bound at a shorter distance with a large potential anisotropy. The reason for the fast conversion was discussed that the short H_2–Cu distance enhances the interaction between H_2 and substrate electrons. They also extended their analysis to H_2 on a flat terrace and argued that the conversion mainly takes place at a special active site, which is likely to be step atoms.

Since Cu is a diamagnetic metal, no apparent magnetic moments are present on the surface except for nuclear spins. Since the magnetic moment due to nuclear spins is small, the conversion time due to nuclear spins is expected to be $\sim 10^5$ s. Yucel considered fluctuation of the electron spin density in the surface, and theoretically calculated the o-p conversion time of H_2 on Cu within a first-order perturbation on the basis of the magnetic

dipole, Fermi contact and electron orbital motion, which is shown in Fig. 18 [21]. The calculated conversion time is longer than 10 h at an adsorption distance of 3 Å[75, 173], which does not seem to be consistent with the experimental results. On the other hand, the conversion time calculated on the basis of the two-step XY and UY processes is 100 – 1000 s at a distance of ∼2.5 Å(Fig. 20), which might explain the experimental results. The conversion time of 1 s at step sites is, however, too short as the XY and UY processes, and further discussion is necessary for elucidation of the conversion mechanism on Cu.

5.1.2. Clean Ag surface

The EELS study for H_2 and D_2 physisorbed on Ag surfaces was performed by Avouris et al. [17]. Two samples, single-crystal Ag(111) and an *in-situ* evaporated Ag film, were prepared in UHV, and EELS spectra were taken after various dosages of H_2 and D_2 at ∼10 K, which are shown in Fig. 33. Three distinct energy loss features were observed at 49, 518 and 562 meV after H_2 dosage of 1 L, which were assigned to the rotational excitation of J=0 → 2, pure vibrational excitation of v=0 → 1, and rovibrational excitation of (v=0 → 1)+(J=0 → 2), respectively. With increasing H_2 dosage, these peaks were found to slightly shift to lower energies, and another loss feature was observed at 70 meV, which was attributed to the J=1 → 3 rotational excitation of o-H_2. These values are close to those of the gas phase H_2 (Table 5). It was also shown that the spectra taken for the Ag film and Ag(111) are similar. As for D_2, energy loss features were observed at 25, 370, 395, and 410 meV. These values are similar to the excitation energies of J=0 → 2, v=0 → 1, (v=0 → 1)+ (J=0 → 2), and (v=0 → 1)+ (J=1 → 3) of D_2, respectively. On this basis, it was argued that both H_2 and D_2 adsorbed on Ag surfaces are in the nearly-free rotor state. On the other hand, the loss feature observed in the EELS spectra was broader than 10 meV. It was argued that this broadening is caused by rotational sublevel splitting [229], which suggests potential anisotropy as shown in Fig. 9. The broadening, however, might be caused by combined excitation of rotational states with the surface-molecule vibration (n=0 → 1 in Fig. 9(a) and Fig. 10).

In the work by Avouris et al., the sticking probability of molecular hydrogen was considered to be unity, and a condensed multilayer was considered to be formed at a larger H_2 dosage. However, the sticking probability of molecular hydrogen is generally low as discussed in Sec. 2.2.3. Considering the vapor pressure of H_2 at 10 K [230, 231], furthermore, multilayer forma-

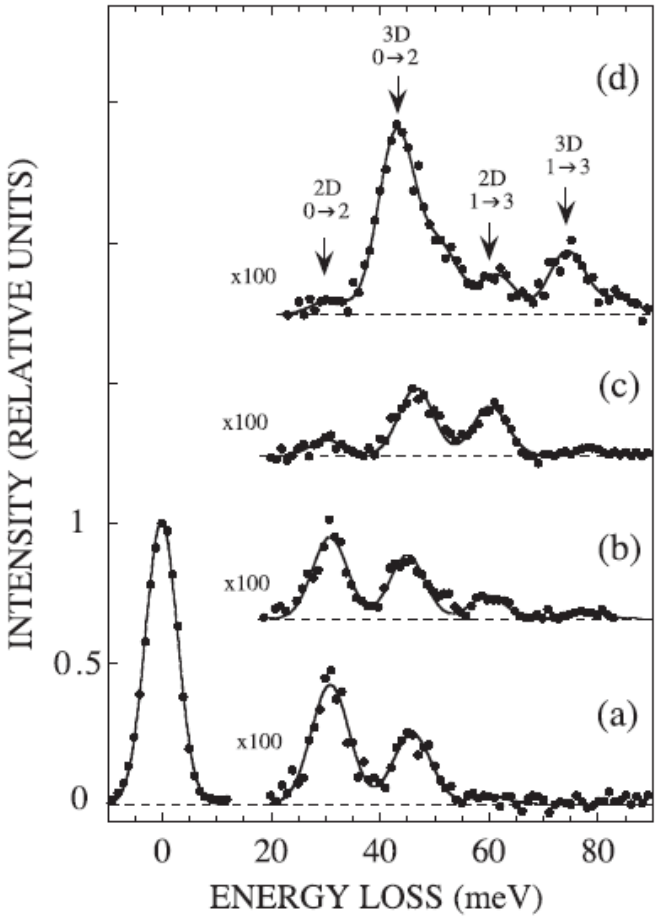

Figure 32: EELS spectra for H_2 physisorbed on Cu(510) taken at temperatures and H_2 pressures of (a) 14 K and 1.5 $\times 10^{-8}$ Torr, (b) 16 K and 1.5 $\times 10^{-7}$ Torr, (c) 17 K and 5 $\times 10^{-7}$ Torr, and (d) 14 K and 4×10^{-7} Torr. Two adsorption states are indicated by 2D and 3D, which correspond to the hindered rotor and nearly-free-rotor physisorbed at step and flat terrace sites, respectively. The rotational transitions relevant to the loss features are also shown in the figure. The relative intensities of the $J = 0$ and $J = 1$ states depend on the pressure and temperature reflecting the gas-phase exchange and o-p conversion kinetics. From the experimental data, the o-p conversion time is analyzed to be 1 s at step sites. Reproduced with permission from [228].

tion is unlikely to occur at 10 K in the UHV condition. Therefore, the EELS spectra correspond to those in the monolayer region. On the basis of the rotational excitation energy, the possibility of the contraction of the interatomic distance was discussed. Recent theoretical studies, however, showed that contraction of the interatomic distance is small in the physisorbed state [75, 173].

Similarly to Cu, both $J = 0$ and $J = 1$ corresponding to para and ortho species are present on Ag surfaces. Nevertheless, the intensity of $J{=}1 \rightarrow 3$ is considerably smaller than that of $J{=}0 \rightarrow 2$, indicating that the adsorbed H_2 is mostly in p-H_2. Avouris et al. suggested that o-p conversion takes place within 1–2 min on the surface or upon adsorption. Since the o-H_2 intensity is only recognized at a larger H_2 dosage, the o-p conversion time might be coverage-dependent [17].

The o-p conversion was later investigated by the REMPI-PSD method [25, 223, 224, 225]. Normal H_2 and D_2 were adsorbed on an Ag film surface prepared in UHV at 7 K, and the evolution of the ortho and para coverages were monitored by REMPI-PSD. Figure 34(a) shows the intensity ratio of H_2 in $J = 1$ and $J = 0$ as a function of time after H_2 dosage. This reflects the coverage loss of o-H_2 due to o-p conversion [25]. The intensity ratio decreased almost exponentially with increasing time, which suggests that o-p conversion takes place on the surface as a first-order reaction. From the analysis of the data, the o-p conversion time of H_2 and p-o conversion time of D_2 on Ag were evaluated to be $\sim$700 and $\sim$1000 s, respectively [25, 224].

It was furthermore recognized that there are photoexcitation effects on the o-p conversion, which is displayed in Fig. 34(b) and (c). Here, the o-p ratio was monitored at a higher PSD laser fluence. As the PSD laser fluence of 193 nm (6.4 eV) was increased, the $(J = 1)/(J = 0)$ ratio decreased faster. This suggests that photon irradiation accelerates the o-p conversion. Wavelength dependence of this photoexcitation effect is demonstrated in Fig. 35. While irradiation of photons at 6.4 eV accelerated the o-p conversion of H_2 on Ag (Fig. 35(b)), no significant effects were observed with irradiation of 2.3 eV photons (Fig. 35(c)) [224].

The surface of deposited Ag films contains defects such as vacancies and steps, which might affect the o-p conversion kinetics. As described above, however, the spectral features and intensities of EELS representing o-H_2 and p-H_2 were similar between on a single-crystal surface of Ag(111) and an Ag film surface [17]. The o-p conversion time measured for the Ag(111) surface with REMPI-TPD also showed the conversion time of about 700 s in

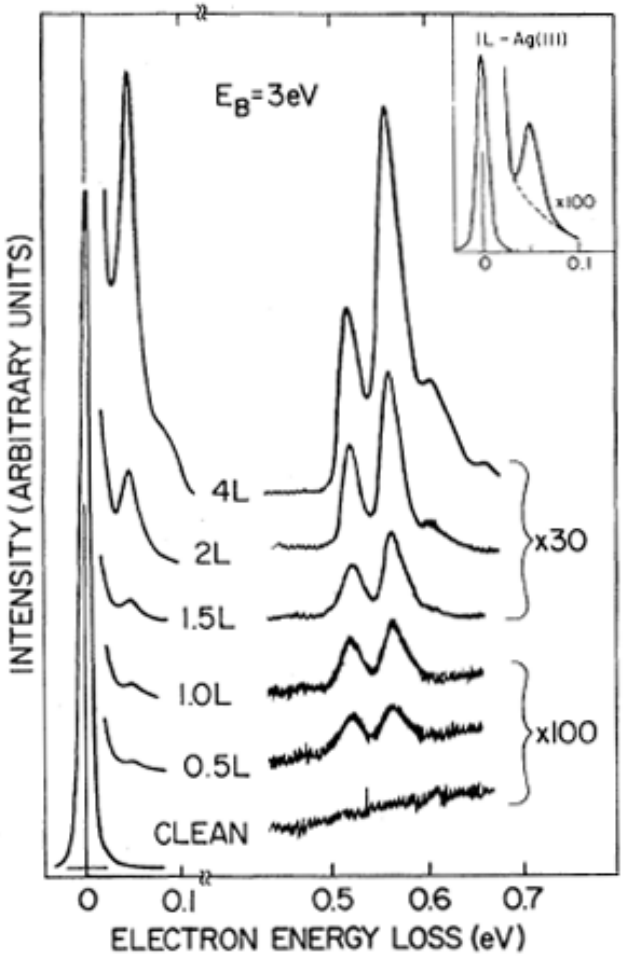

Figure 33: EELS spectra for H_2 physisorbed on Ag surfaces at $\sim$10 K after various H_2 dosages. Loss features develop at 49 (J=0$\rightarrow$2), 70 (J=1$\rightarrow$3), 518 (v=0$\rightarrow$1), and 562 meV ((v=0$\rightarrow$1)+(J=0$\rightarrow$2)) with increasing H_2 dosage. The loss intensity corresponding to J=1 is apparently smaller than that of J=0. Reproduced with permission from [17].

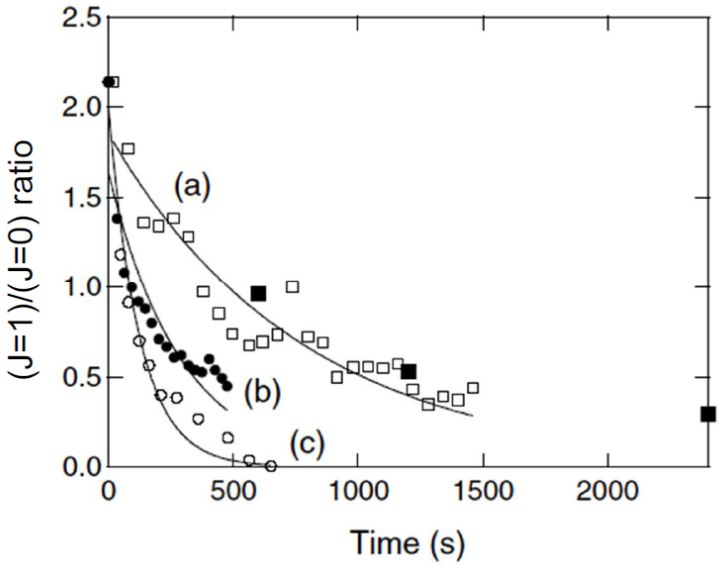

Figure 34: The (J=1)/(J=0) ratio of H_2 on an Ag surface at 7 K as a function of time probed by REMPI-PSD with a pump laser wavelength of 193 nm at laser fluences of (a) 10, (b) 150, and (c) 250 μJ /cm^2 / pulse. The (J=1)/(J=0) ratio decreases exponentially due to the o-p conversion, and the solid curves are fits with an exponential function. Filled squares denote the (J=1)/(J=0) ratios measured 600, 1200, and 2400 s after the H_2 dosage on a nonirradiated sample to avoid the laser irradiation effect. Reproduced with permission from [25].

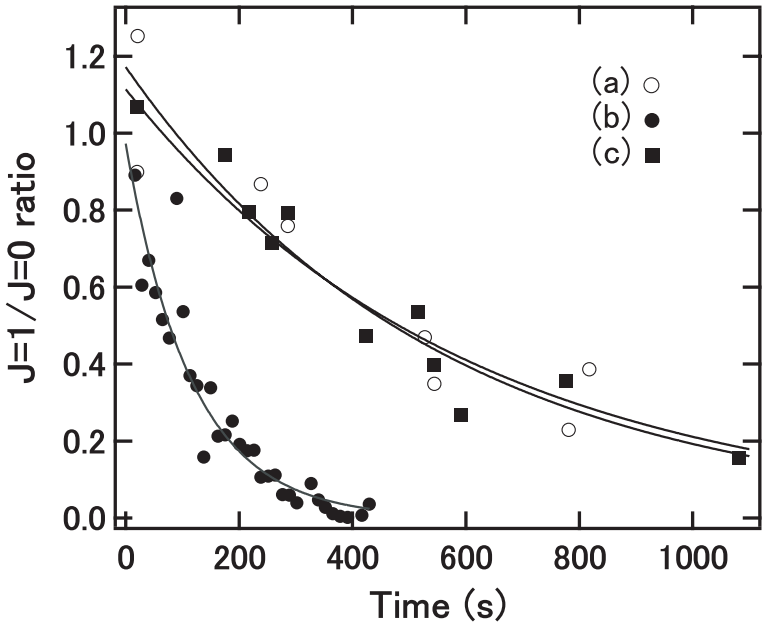

Figure 35: The (J=1)/(J=0) ratio of H_2 on an Ag surface at 6 K as a function of time probed by REMPI-PSD. (a) Probed every 250 s, (b) probed under laser irradiation at 193 nm with a fluence of 120 μJ/cm^2/pulse and a repetition rate of 10 Hz, (c) probed under laser irradiation at 532 nm with a fluence of 120 μJ/cm^2/pulse and a repetition rate of 10 Hz. While the laser irradiation of 193 nm accelerates the o-p conversion, that of 532 nm has little effect on the o-p conversion. Reproduced with permission from [224].

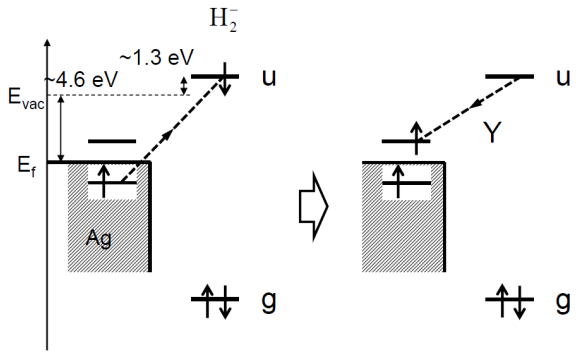

Figure 36: Electronic structure of H_2 physisorbed on Ag, and electronic processes for the two-step UY process. An electron in Ag is virtually excited to the $1\sigma_u$ orbital through the Coulomb interaction (C) forming H_2^-. The electron is transferred back to Ag through the Fermi contact interaction (Y) along with the nuclear-spin conversion.

agreement with the value obtained for the deposited film [96]. These results suggest that the defect sites formed on an Ag film surface do not play a major role in the o-p conversion on Ag surfaces, which is also supported by the experiment on Xe-covered Ag(111) as mentioned in the next section. This is in contrast to the fact that the step site is active for the conversion on Cu surfaces [228].

On the basis of the experimental data, the o-p conversion mechanism was discussed in terms of the two-step process (Sec. 3.4). Since Ag is an sp-metal with a diamagnetic character as Cu, where the d-band is fully filled with the Fermi level located within the sp-band, the o-p conversion time can be compared with the values calculated for Cu on the basis of the one-step process shown in Fig. 18 [21]. The values calculated on the basis of the interaction with substrate electrons are considerably larger than the experimentally obtained conversion time of ∼700 s by REMPI-PSD. On the other hand, the conversion times predicted by the two-step model are close to the experimental values as shown in Fig. 20 [162, 22].

The excitation energy for the intermediate state in the XY process (Fig. 19) is ∼10.5 eV considering the lowest neutral $^3\Sigma_u^+$ state of H_2 is $b^3\Sigma_u^+$ [232]. The excitation energy for the UY process, on the other hand, was estimated to be ∼6 eV, because the Fermi level (E_f) of Ag is located at ∼4.6 eV below the vacuum level [233] and the affinity level of H_2 is lowered from 2.3 eV

above the vacuum level in gas phase [194] by about 1 eV due to the image charge effect [234, 10], which is shown in Fig. 36.

Of these two processes, the two-step UY mechanism was furthermore rationalized by the results of photoacceleration. The experimental results showed that the o-p conversion is accelerated by 6.4 eV photons, but not at 2.3 eV. As discussed above, the intermediate state for the UY process (the H_2^- state) can be formed at a photon energy of 6.4 eV, while it is not accessible by photons at 2.3 eV. The neutral $^3\Sigma_u^+$ state in the XY process, on the other hand, can be excited by photons at neither 6.4 eV nor 2.3 eV. Therefore, the intermediate state responsible for the o-p conversion was argued to be the ionic H_2^- state.

The isotope difference between H_2 and D_2 was also discussed. The conversion time of D_2 is longer than that of H_2 by a factor of 1.7 [224]. The electronic structure is essentially the same for these two isotopes, which means the electron transfer process in Fig. 36 is expected to be similar for H_2 and D_2. On the other hand, the Fermi contact (Y) process for H_2 is more efficient than that of D_2 by a factor of 7.1, as described in Sec. 3.6, which is significantly larger than the experimental result of 1.7. This apparent discrepancy is discussed to be ascribed to the efficiency of the rotational-energy dissipation. The rotational energy of 7.1 meV for D_2 can be more efficiently accommodated by other degrees of freedom as compared to 14.7 meV for H_2 [224].

An important discussion was given on the energy dissipation mechanism. Whereas the o-p conversion time was derived by the REMPI-PSD method, the results showed no increase of the p-H_2 on the surface even after o-p conversion [25]. This suggested that the converted H_2 was desorbed from the surface upon o-p conversion. As shown in the previous section, the o-p conversion is accompanied by the rotational-energy release. A possible interpretation was that the rotational energy was transferred to the motion of the molecule center of mass, either the H_2–substrate vibration or H_2 translational motion in the surface parallel direction, and that desorption of the molecule was subsequently promoted. It is noticed, however, the rotational energy of o-H_2 in $J = 1$ is smaller than the typical physisorption energy, which means the rotational-energy transfer is not sufficient to induce desorption of H_2.

For such energy transfer, coupling between the rotational and translational (vibrational) motion is necessary, which originates from the potential anisotropy of physisorption. A recent theoretical study showed that the rotational sublevel splitting due to the anisotropy imposes steric effects and

accelerated o-p H_2 conversion [173, 172]. In the original two-step model, on the other hand, the rotational energy is expected to flow into the electronic system of the substrate causing electronic excitation. The mechanism of the o-p energy release is obviously the subject of further experimental and theoretical studies.

5.1.3. Impurity-adsorbed surface

Xe

Sakurai et al. investigated H_2 adsorbed on Xe-covered Ag(111) with EELS [20]. The substrate was kept at 6 K and exposed to a certain pressure of H_2 while measuring the EELS spectrum. Thus, the adsorbed H_2 layer at the surface was expected to be in equilibrium with the gas phase H_2, where the desorption rate is balanced with adsorption rate from the gas phase. The EELS spectra revealed energy loss features corresponding to rotational excitations and rovibrational excitations of H_2. From the analysis of the experimental data on clean Ag(111), the o-p ratio was estimated to be 0.2 – 0.4 at a low H_2 pressure and increase to 1.3 – 1.5 at a higher H_2 pressure. On the basis of this observation, it was concluded that o-p conversion takes place on Ag(111). Since the o-p conversion was suspected to occur on local active sites such as defects, the o-p ratio was examined on Xe-covered Ag(111) where Xe atoms were expected to occupy the active sites prior to H_2 adsorption. However, the o-p ratio did not change with and without the Xe preadsorption, which would rule against the o-p conversion mechanism originating from defect sites. The results suggest that the o-p conversion on Ag(111) takes place via the direct interaction with the flat substrate Ag.

N_2

The rotational spectrum was observed with EELS for H_2 co-adsorbed with N_2 on Ag(111) at a temperature of 20 K by Gruyters and Jacobi [235]. While H_2 was not adsorbed at 20 K on bare Ag(111), an appreciable amount of H_2 was adsorbed on the N_2-precovered surface. The loss peaks due to rotational excitations of 44 and 73 meV were observed in the spectra for H_2 of 2 L adsorbed on N_2–precovered Ag(111). The loss peak intensity at 73 meV corresponding to J=1 of o-H_2 was about a quarter of the J=0 intensity of p-H_2, which suggested o-p conversion on Ag(111). Although the precise conversion time was not given in the work, the o-p conversion seems to have

proceeded with the time scale comparable with the EELS acquisition time. It is also suggested that the o-p conversion takes place via the direct interaction with the substrate Ag as discussed for Xe-covered Ag.

O_2

The electronic term of the ground state O_2 is $^3\Sigma_g^-$, which means that O_2 is paramagnetic with an electron spin of 1 in contrast to Xe and N_2. When O_2 is chemisorbed on a surface, possible electron transfer between O_2 and the substrate changes the magnetic property of O_2. When O_2 is in the physisorption state, however, little electron transfer occurs, and the electronic spin state is expected to be unchanged. Such an electronic state of O_2 on metallic surfaces was identified on Cu and Pt by Near-edge X-ray absorption fine structure (NEXAFS) spectroscopy [236, 237]. Although the electronic spin of O_2 is retained on metal surfaces, the Kondo effect could screen the spin at low temperature [238]. On Ag surfaces, O_2 is physisorbed at low temperature [239], and the adsorption structure and magnetic property of O_2 were studied experimentally and theoretically [240, 241, 242]. Even in the chemisorbed state, dissociated O might have a magnetic moment as pointed out by a recent theoretical study [243].

Sakurai et al. investigated the effect of O_2 on the o-p ratio of H_2 physisorbed on Ag(111) in equilibrium with gas phase by EELS [20]. The o-p ratio of H_2 measured on O_2/Ag(111) was smaller than that on clean Ag(111), which was attributed to the magnetic effect of adsorbed O_2.

The effect of adsorbed O_2 on the o-p conversion of H_2 and p-o conversion of D_2 was investigated on Ag surfaces at 7 K by REMPI-PSD [225]. Figure 37 shows the change of the $(J{=}1)/(J{=}0)$ ratio as a function of time on O_2-adsorbed Ag surfaces with various O_2 coverages. As the O_2 coverage was increased, the decay rate of the $(J{=}1)/(J{=}0)$ ratio was found to be enhanced. A similar tendency was also observed for D_2. Adsorbed O_2 obviously promoted the H_2 o-p conversion and D_2 p-o conversion. Figure 38 shows the variations of the decay time constants for H_2 and D_2 as a function of the O_2 coverage. The time constants decreased with increasing O_2 coverage.

Because the O_2 coverage was in a submonolayer regime in the experiments, the o-p (p-o) conversion of adsorbed H_2 (D_2) was postulated to take place via two independent mechanisms: one near the paramagnetic O_2 and the other on the bare Ag surface. The conversion mechanism on Ag is, as described in Sec. 5.1.2, likely to be the two-step UY process with conversion times of $\sim$700 and $\sim$1000 s for H_2 and D_2, respectively. In the vicinity of

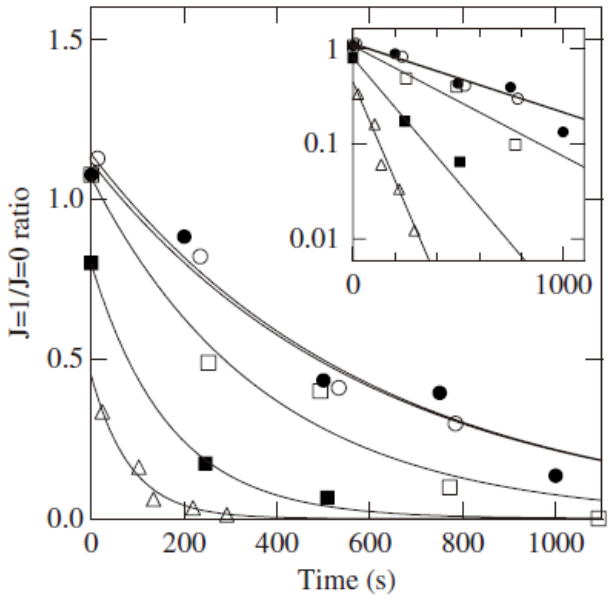

Figure 37: Time evolution of the $(J{=}1)/(J{=}0)$ ratio of H_2 physisorbed on O_2-adsorbed Ag surfaces probed by REMPI-PSD at 7 K. With increasing O_2 coverage from 0 (open circles) to 0.01 ML (open triangles), the $(J{=}1)/(J{=}0)$ ratio decreases faster, which indicates the o-p conversion is accelerated by adsorbed O_2. Reproduced with permission from [225].

the adsorbed O_2, on the other hand, the o-p conversion can be promoted by the O_2 paramagnetic spin. When such two mechanisms are operative, the entire conversion kinetics is governed by the diffusion of hydrogen molecules on the surface as was also discussed for o-p conversion in solid H_2 containing O_2 impurities [244, 245, 246]. The diffusion might proceed via quantum tunneling as well as thermal activation [247]. With the aid of Monte Carlo simulations, the hydrogen diffusion time between the adsorbed O_2 and bare Ag sites was found to be much faster than the o-p conversion time at either bare Ag site and in the vicinity of O_2 on the basis of the single-exponential feature observed by the experiments in Fig. 37. Figure 38 demonstrates the change of the relative contribution of the two conversion mechanisms. From the analysis of the data, the conversion times in the vicinity of adsorbed O_2 was estimated to be 8.3 ± 1.2 s and 53.4 ± 9.3 s for H_2 and D_2, respectively [225].

As discussed in the beginning of this section, adsorbed O_2 is expected to

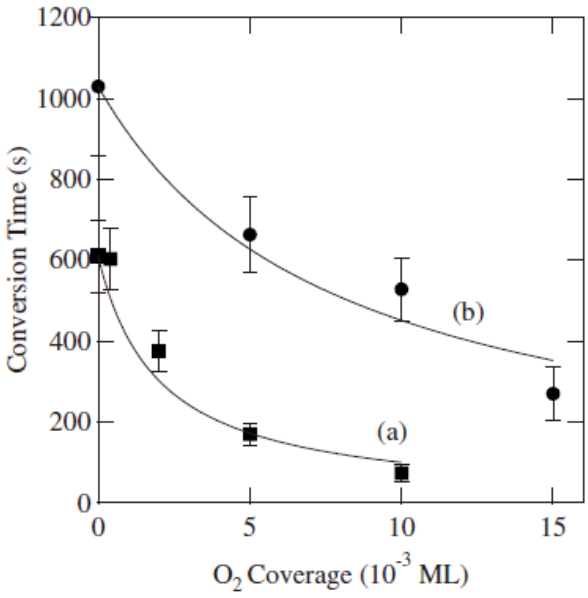

Figure 38: Decay time of the (J=1)/(J=0) ratio (nuclear-spin conversion time) of (a) H_2 and (b) D_2 on O_2-adsorbed Ag surfaces at 7 K estimated by REMPI-PSD as a function of the O_2 coverage. The o-p (p-o) conversion of H_2 (D_2) is promoted by adsorbed O_2. Reproduced with permission from [225].

possess paramagnetic electron spins. In the vicinity of O_2, there exists an inhomogeneous magnetic field as illustrated in Fig. 15. The magnetic dipole interaction in Eq. 15 then yields the nuclear-spin and position difference operators, which induce o-p conversion as a one-step process. As well as the magnetic dipole interaction, the direct Fermi contact interaction might also be important for the o-p conversion, because adsorbed O_2 has a finite electron density at the H_2 position. The o-p conversion time due to the magnetic dipole and Fermi contact interactions was theoretically evaluated by a recent study by Kunisada et al. [248]. Figure 39 shows the o-p conversion time calculated as a function of the H_2 distance from the Ag surface at two adsorption sites of O_2 on-top and beside O_2. The conversion time is strongly dependent on the H_2-Ag distance at both adsorption sites, and the conversion time at an distance of 3.5 Å is about 10 s at the on-top site of O_2 for both interactions. This is consistent with the experimentally observed value, suggesting that the conversion mechanism in the vicinity of O_2 is the one-step process via the magnetic dipole and/or Fermi contact interactions. It should be noted, however, that the contribution of the two-step XY process via the Coulomb and Fermi contact interactions (Sec. 3.4) could be operative competing with the one-step process as pointed out by Ilisca and Sugano [160].

Compared with the conversion through direct interaction with Ag (Sec. 5.1.2), the isotope dependence of the conversion time in the vicinity of adsorbed O_2 is larger with a relative ratio of 6.4. As described in Sec. 3.6, the magnetic interaction, either magnetic dipole or Fermi contact, is larger for H_2 than D_2 by a factor of 7.1, which is similar to the experimental result of 6.4. In contrast to the conversion on bare Ag, the overall conversion rate is mainly governed by the strength of the magnetic interaction and the efficiency of the rotational-energy dissipation seems to be similar for H_2 and D_2 [225].

5.1.4. Graphite

Compared with metallic surfaces, the graphite surface is inert and is likely to be free from contaminations as demonstrated by STM atomic imaging in an atmospheric condition. Moreover, the graphite sample can be easily cleaved providing a large surface area. Well-defined graphite surfaces are, therefore, expected to be prepared in an ordinary vacuum apparatus without UHV, and traditional non-surface-sensitive methods may be used for the o-p conversion study. The o-p conversion data on charcoal surfaces obtained in

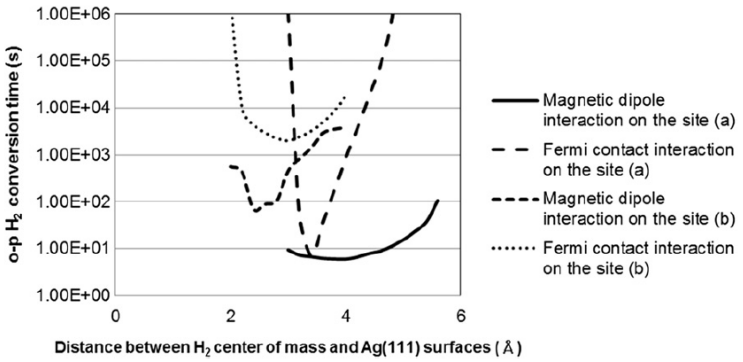

Figure 39: O-p conversion time calculated for H_2 on O_2-adsorbed Ag(111) as a function of the H_2 distance from Ag(111). O_2 is adsorbed at the bridge site of Ag with its molecular axis parallel to the surface, and the O atom is calculated to have a magnetic moment of 0.52 β_e (β_e: Bohr magneton). The o-p conversion time is evaluated on the basis of the one-step process with the magnetic dipole and Fermi contact interactions at (a) on-top of O_2 and (b) near O_2 sites. At the on-top O_2 site, the conversion time is about 10 s. Reproduced with permission from [248].

a traditional manner are available in literatures [1], which may be compared with the studies described below.

Kubik et al. investigated the H_2 layer physisorbed on graphite in order to examine the rotational ordering [249]. They prepared a stack of Grafoil sheets sandwiched with Teflon and Cu foils to ensure cooling of the sample, on which enriched o-H_2 and p-D_2 with a concentration of c>0.98 were adsorbed, and the relative ortho concentration on the sample was measured by NMR below 4.2 K. The absolute concentration o-H_2 and p-D_2 before adsorption was determined with Raman by probing the J=1 $\rightarrow$ 3 and J=2 $\rightarrow$ 4 transitions. The o-p conversion of H_2 was found to be a first-order process and the conversion rate was as slow as 0.4 %/h, although the raw data are not presented in the paper. The D_2 conversion was much slower than that of H_2, and the conversion rate was estimated to be 0.069 %/h on the assumption that the conversion is the first-order process. It is also reported that the o-p conversion during the adsorption process is much faster than these conversion rates. The authors suspect that there are some paramagnetic sites, which can be active for o-p conversion when H_2 is mobile on the surface during adsorption. According to the phase diagram of H_2 on graphite, a fluid phase exists above 10 – 20 K, where H_2 is mobile on the surface [250, 251].

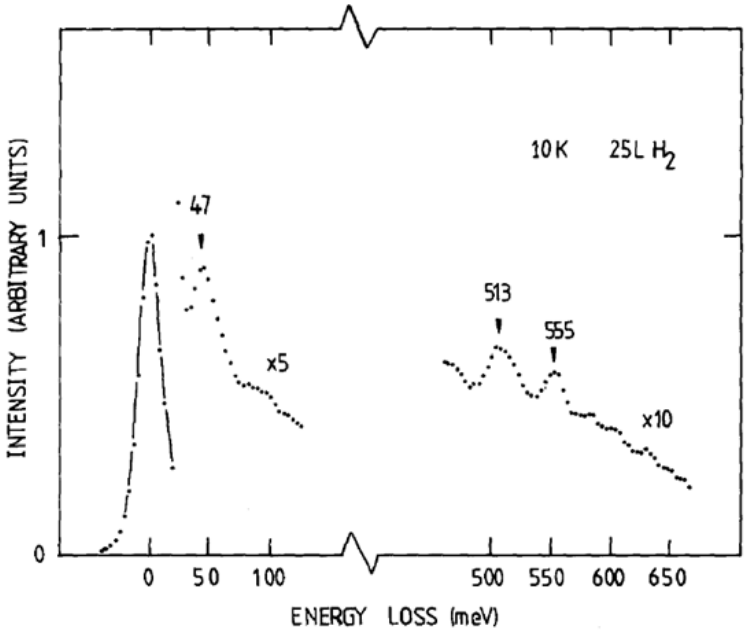

Figure 40: EELS spectrum for H_2 physisorbed on highly ordered pyrolitic graphite at 10 K. Loss features are observed at 47 (J=0→2), 513 (v=0→1), and 565 ((v=0→1)+(J=0→2)). No features originating from $J = 1$ (o-H_2) are observed. Reproduced by permission from [19].

Palmer and Willis investigated H_2 on highly ordered pyrolitic graphite (HOPG) at 10 K by EELS in UHV, which is shown in Fig. 40. Prior to the measurements, the sample was heated to 1300 K to remove contaminants. After adsorption of n-H_2, a loss feature was observed at 47 meV corresponding to J=0 → 2 of p-H_2 and no loss feature corresponding to o-H_2 was identified. The shoulder at 80–100 meV was assigned to double excitation of J=0 → 2, and the loss features at 513 and 555 meV were attributed to the pure vibrational excitation of v=0 → 1 and ro-vibrational excitation of (v=0 → 1) + (J=0 → 2). On the basis of the data, it was concluded that H_2 is in a nearly-free-rotor state and that the o-p conversion occurs on the graphite surface on a time scale of 1 min. The authors argued that there are paramagnetic spins on the surface and the mechanism is the one-step process via the magnetic dipole interaction as the O_2 impurity on Ag.

Yucel et al. investigated p-o conversion of D_2 on Grafoil at various temperatures by the thermal-conductivity method [252]. The grafoil disks were

sandwiched in copper foils to efficiently cool the sample. The p-D_2 concentration decreased exponentially against time indicating that the p-o conversion proceeds as a first-order reaction. The measured conversion time was almost constant up to a certain coverage followed by a linear increase with increasing D_2 coverage. This coverage was regarded as completion of a monolayer. In a monolayer regime, D_2 forms either a dense incommensurate layer or a relatively nondense commensurate layer. The temperature dependence of the conversion time was measured for these two phases, which are shown in Fig. 41. In the temperature range of 10 – 20 K, the conversion time was almost constant, and they increased below 10 K. No significant conversion was observed at 6.4 K. They argued that there are paramagnetic sites of less than 0.01 and the increase of the conversion time is due to limited diffusion of D_2 on the surface. Furthermore, the conversion time was theoretically estimated in terms of the energy dissipation into two-dimensional solid phonon and lateral vibration in the two-dimensional lattice gas, which were in a reasonable agreement with the experimental results. No unusual conversion during the adsorption process was observed in this work [252].

The three studies on graphite shown above all suggested presence of paramagnetic impurity sites on the surface promoting o-p conversion of H_2 or p-o conversion of D_2. Compared with metal surfaces, a graphite surface possibly has an edge site. The edge state of graphite was theoretically shown to possess a localized magnetic moment [253], which is being confirmed experimentally [254]. Such edge states could produce an inhomogeneous magnetic field and promote o-p conversion as O_2 on Ag. The o-p conversion data might provide information about the magnetism of the edge state of graphite. On the other hand, graphite is a zero-gap semiconductor, and there is a finite density of states near the Fermi level within the o-p energy [255]. This indicates that the two-step XY or UY mechanism may be operative as Cu and Ag. Nevertheless, the slow conversion rate when H_2 is solidified on the surface at lower temperatures suggests that the two-step mechanism is not effective possibly because of the low density of states near the Fermi level. It is noted that the electron density near the Fermi level of the graphene (single layer of graphite) can be controlled by the gate bias as demonstrated by the electrical conductivity measurement shown in Fig. 42 [255]. The band structure of graphene is described by the Dirac cone and the electron density at the Fermi level increases with increasing and decreasing bias with respect to the Dirac point. This suggests the two-step conversion process can be enhanced by applying the gate bias enabling us to electrically control the o-p

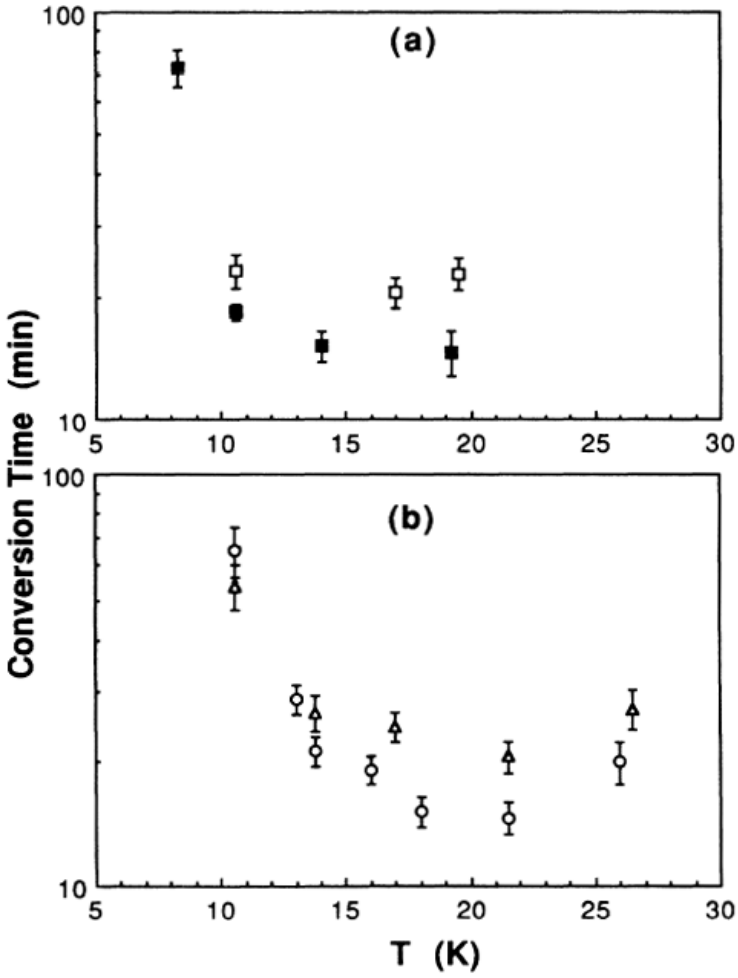

Figure 41: The p-o conversion time of D_2 on Grafoil measured by the thermal-conductivity method as a function of sample temperature. (a) High H_2 coverage incommensurate phase (open and solid symbols: first and second series) and (b) low H_2 coverage commensurate phase (circle and triangle symbols: low and high coverages). Reproduced by permission from [252].

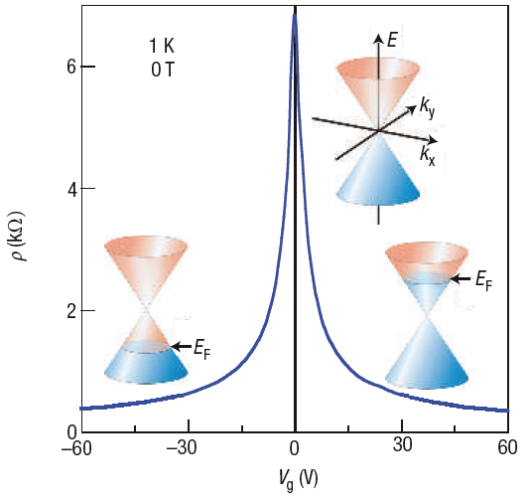

Figure 42: Electric conductivity of a graphene as a function of the gate bias voltage. Insets show the Dirac cone band structure and change of the Fermi level at different bias voltages. Reproduced by permission from [255].

conversion.

5.2. Diamagnetic insulator surface

5.2.1. Ice surfaces

The o-p conversion proceeds on diamagnetic metal surfaces via the two-step process accompanied by virtual electronic excitation. On diamagnetic insulator surfaces, on the other hand, the two-step process seems not operative. As illustrated in Fig. 19(b) and (c), the final state of the surface in the two-step process is a spin triplet state. Whereas a diamagnetic metal requires no excitation energy for the transition from the electron spin singlet to triplet, a large energy corresponding to the band gap is necessary for the transition on a diamagnetic insulator. O-p conversion was investigated on some oxides and a D_2O-covered oxide in a traditional manner, where the conversion was clearly recognized [256]. While the fast conversion on oxide surfaces was attributed to paramagnetic impurities due to oxygen vacancies, the origin of the conversion on a D_2O surface was discussed to originate from an induced dipole moment, although detailed physical mechanism was not given [256].

As stated in Sec. 6, amorphous solid water (ASW) is a dominant interstellar medium, and a diamagnetic insulator. H_2 on ASW was investigated with IRAS by Hixson et al. [198]. Microporous amorphous ice with a thickness of $2 - 4$ μm was formed on a substrate at 12 K, and H_2 was admitted in the ASW sample either during the water deposition or by exposure of ASW to H_2 gas after ASW formation. Figure 43 shows the IR spectra taken for H_2 adsorbed on amorphous D_2O at 12 K under a high vacuum environment. Two absorption features were observed at 4132 and 4141 cm^{-1}. After careful examination of the spectra, the two features were ascribed to vibrational excitation of o-H_2 and p-H_2, respectively, which are slightly shifted from the gas phase values of 4153 and 4159 cm^{-1} listed in Table 5. As stated in Sec. 4, these signals are induced absorption due to the surface electric field. As the adsorption time was increased from 10 to 600 min, the absorption intensity corresponding to o-H_2 decreased whereas that due to p-H_2 increased noticeably. This suggests o-p conversion on the ice surface, and the effective conversion half-life time was estimated to be $\sim$40 min. It was also noticed that the absorption intensity due to o-H_2 was recovered upon annealing at 16 K, which was ascribed to enhanced mobility of H_2 in ASW. It was argued that there are several binding sites for H_2, some of which are active for induced IR absorption [198]. Upon annealing, unconverted o-H_2 migrated to such active sites. Hixson et al. also theoretically examined the binding site of H_2 in the amorphous ice. There were several binding geometries identified and the estimated vibrational frequencies of H_2 were in agreement with the experimental observation. As to the kinetics of the o-p conversion in ASW, the purity of the sample was questioned in this work, and the conversion was suspected to be induced by some paramagnetic impurities incorporated during the ice sample preparation [198].

The o-p conversion on ASW was recently investigated by the REMPI technique. While the p-o conversion rate of D_2 was found to be slow and negligible [26], Watanabe et al. suggested o-p conversion of H_2 taking place on an ASW surface [257]. Sugimoto and Fukutani investigated the o-p conversion of H_2 and p-o conversion of D_2 on ASW in a UHV condition. ASW films of sixty layers were grown on a clean Ag(111) single-crystal surface at 13 K by dosing D_2O molecules. Prior to the conversion experiments, the ice film was annealed up to 55 K to avoid any structural changes during the conversion experiments and to confirm the sample is free from O_2, which desorbs below 50 K [258]. After exposing the ASW film at 10 K to n-H_2 (D_2), the coverages of the ortho and para species were measured by REMPI-TPD.

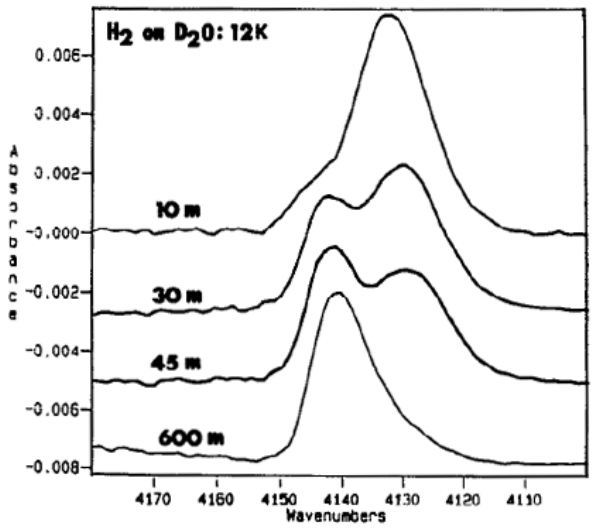

Figure 43: Infrared absorption spectra of H_2 on porous amorphous ice at 12 K as a function of time after H_2 adsorption from 10 to 600 min. The absorption features at 4132 and 4141 cm^{-1} correspond to vibrational excitation of o-H_2 and p-H_2, respectively, and the absorption intensities change as a function of time. Reproduced by permission from [198].

Figure 44 shows the time evolution of the H_2 and D_2 in J=0 and J=1. As the residence time on the ASW surface increased, the intensity of J=1 decreased and that of J=0 increased. Fitting a single exponential function to the J=1 data gave decay time constants of 370^{+340}_{-140} s for H_2 and 1220^{+2980}_{-580} s for D_2 (the numbers in the subscripts and superscripts denote the upper and lower limits of uncertainty). In contrast to the conversion on a flat Ag surface [25], the sum of the intensities of these two species was constant within the experimental accuracy. This is probably because the ASW sample was porous: even if the converted H_2 was desorbed from the surface of ASW pores, the H_2 was readsorbed on the pore surface. The conversion time of D_2 is also reported to be as slow as 15 %/h [226], which is in rough agreement with the above value.

A possible mechanism for the o-p conversion of H_2 and p-o conversion of D_2 was discussed in detail [33]. On an ice surface, there exists a strong electric field originating from the electric dipole moment of H_2O (1.85 D). When water molecules are condensed in a solid, the dipole moment is possibly enhanced to about 3 D [259, 260], which would also enhance the electric field on the surface of ASW. The electric field on an ice surface was simulated to be $\sim 10^{10}$ V/m [261, 262], which could produce an electric field gradient of 10^{20-21} V/m^2. Since the deuteron nucleus has a quadrupole moment (Table 4), the nuclear quadrupole interaction can be significant for the p-o conversion of D_2. Under an electric-field gradient, as discussed in Sec. 3, the spin-state transition and rotational-state transition can be induced as a one-step process. With this electric field gradient, the quadrupole interaction energy leads to $\sim 10^{-11}$ eV. This value was compared with the theoretical estimation for solid D_2 [139]. In solid D_2, there exists an electric field of $\sim 10^8$ V/m and field gradient of $\sim 10^{18}$ V/m^2 at a neighboring site due to the quadrupole moment of hydrogen molecules (0.48 au) [3]. With this electric field gradient, the p-o conversion time was theoretically evaluated to be $\sim 10^8$ s [139]. If the electric field gradient is 10^{20-21} V/m^2, the conversion time is expected to be $\sim 10^3$ s, which is in agreement with the experimental value on ASW.

The effects of nuclear spins should be considered, as hydrogen (deuteron) of H_2O (D_2O) has a nuclear spin, which produces an inhomogeneous magnetic field causing the conversion as a one-step process. The conversion time due to the nuclear spins, however, was roughly evaluated to be the order of 10^6 and 10^8 s for H_2 and D_2, respectively [149, 139]. Therefore, the magnetic interaction with nuclear spins of water is not significant for the H_2 o-p

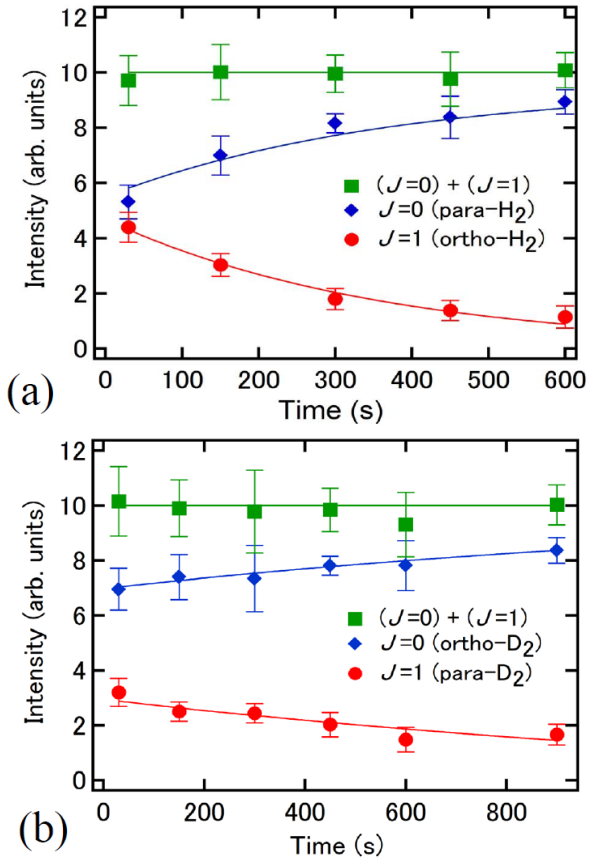

Figure 44: Time evolution of the intensities of J=0 and J=1 and the sum of them measured by REMPI-TPD. (a)H_2 and (b) D_2 on the porous amorphous ice at 10K. The J=1 intensity decreases, while that of J=0 increases with the sum kept constant. Reproduced by permission from [33].

conversion and D_2 p-o conversion on ice surfaces observed in Fig. 44.

Since proton has no quadrupole moment, on the other hand, the quadrupole interaction is not responsible for the o-p conversion of H_2 on ASW. As a possible conversion mechanism, a multi-step process has been proposed [33]. As mentioned in Sec. 3.3.2, different I states are intrinsically mixed with each other through the intra-molecular Fermi contact interaction in the electronically excited state. It should be noted that the mixed state is the electron spin triplet (S=1) state with the same rotational state. For the o-p conversion, both the electron spin state and rotational states must be changed. When the spin-orbit coupling (SOC) is taken into consideration, the S=0 state can be mixed with the S=1 state as shown in Fig. 21.

Without external perturbation, the ortho and para states are not mixed with each other. Under the surface electric field, however, the Stark coupling mixes gerade and ungerade states leading to ΔJ=1. With these multi-step processes, the ortho and para states can be mixed. As described in Sec. 3.3.2, SOC is considerably enhanced for the near-degenerate $r^3\Pi_g$ and $R^1\Pi_g$ states because of weak electron exchange-correlation. The intra-molecular Fermi contact strength was also shown to be enhanced when the vibrational level was taken into consideration for the $a^3\Sigma_g^+$ and $B^1\Sigma_u^+$ states: the energy levels of a (v=6) and B (v=8) are near-degenerate, which results in strong o-p coupling of these states [263]. On the basis of a possible electric field of as large as 10^{10-11} V/m on the ice surface, the overall conversion time of H_2 was roughly estimated to be 10^2 s, which were in agreement with the experimental results of REMPI-TPD. It was also pointed out that the SOC may be enhanced with an external electric field [33]. As discussed in Sec. 3.6, the magnetic interaction is weaker for D_2 because of the smaller nuclear g factor. It is discussed that the conversion time due to the multi-step process for D_2 is comparable or longer than the conversion time evaluated on the basis of the quadrupole interaction described above [33]. Therefore, the dominant channel of the D_2 p-o conversion on ASW might be the one-step process via the quadrupole interaction.

As another form of a solid water, clathrate has ice-like frameworks composed of H_2O molecules having a regular array of cages, in which small molecules can be encapsulated. O-p conversion of H_2 encapsulated in clathrate was examined at 20 K by NMR [264]. The NMR signal due to o-H_2 was monitored as a function of time over 200 h, which revealed a slight decrease in intensity. Although the conversion kinetics was not unambiguously determined because of the small intensity change, the conversion rate was evaluated to

be 6×10^{-4} /h on the assumption of the first-order kinetics. O-p conversion of H_2 in clathrate hydrates was also investigated with Raman at 20 K [265], which revealed the conversion rate of $\sim 7\times10^{-3}$ /day. These values are much smaller than the value reported on an ASW surface described above. Since the cage has a symmetrical structure, the electric field at the inner surface of the clathrate might be weakened, and the electric-field induced conversion mechanism is not operative. Dependence of the conversion on the ice surface structure will be an important future subject.

5.2.2. Si

Although the o-p conversion has not been studied on well-defined Si surfaces, recent studies with Raman [188, 266, 189] and IRAS [203] reported the o-p conversion in bulk Si, which is briefly described in this section. In the work by Hiller et al., H_2 was admitted into Si with the RF plasma treatment at 220 °C where H_2 was incorporated into the interstitial site of Si. The o-p conversion rate at 77 K was evaluated to be 0.015 /h, and p-o back conversion time at 300 K was evaluated to be 0.18 /h. By comparing the samples with different oxygen concentrations and dopant concentrations, it was concluded that these impurities were not responsible for the o-p conversion in Si. On the basis of the experimental findings, the origin of the o-p conversion was attributed to the nuclear spin of 4.7 % abundant ^{29}Si, and the conversion mechanism was considered to be the one-step process via the magnetic dipole interaction (Sec. 3.3). Since the H_2 diffusion at 77 K is negligibly slow, the o-p conversion kinetics was analyzed by considering the distance distribution of H_2 from the magnetic moment of ^{29}Si, and the o-p conversion time in the nearest neighbor site was evaluated to be 65 h [188]. On the other hand, Peng et al. investigated the o-p conversion of H_2 and p-o conversion of D_2 with IRAS. While the o-p conversion time at 77 K and p-o back conversion at 300 K of H_2 were 229 h and 8.1 h, respectively, the p-o conversion time at 77 K and o-p back conversion time at 300 K of D_2 were 213 h and 25 h, respectively. In contrast to the multi-component exponential decays expected from the mechanism proposed by Hiller et al., the conversion kinetics measured by IRAS revealed a single-exponential behavior. As discussed in Sec. 3.6, the magnetic interaction for H_2 is stronger than that of D_2 due to the difference of the magnetic g factor. The experiments, however, revealed that the conversion times for H_2 and D_2 are similar. The IRAS study proposed a conversion mechanism where the coupling between the nuclear spins and rotational motion of the molecule center of mass induces ortho-to-para

conversion [203], which needs further verification.

5.2.3. Metal-organic framework

Metal-organic framework (MOF) compounds are a class of materials consisting of inorganic clusters connected by organic ligands, which have a periodic well-ordered structure. MOF's have micropores, in which H_2 is expected to be stored with a high binding energy. In relation to the hydrogen storage, the binding property of H_2 to the inner surface of MOF's and the o-p conversion on the surface have recently been investigated with IRAS [267, 204, 205], although the pore surface is not characterized with surface science techniques. As MOF's without magnetic cations are non-magnetic insulators, the experimental work performed for $Zn_2(C_8H_2O_6)$ named MOF-74 is shown in this section [204].

The MOF-74 sample has a periodic array of micropore with a diameter of 1.1 nm and parallel channels. The inner surface of the pore is lined with Zn^{2+} ions, and the Zn-O electric dipole is exposed at the pore surface. After the powder sample was fixed to a cold head and H_2 was introduced into the chamber at 30 – 50 K, the (ro)vibrational spectra for H_2 physisorbed on the sample were obtained with IRAS. Figure 45 shows the time evolution of the IRAS spectrum taken for H_2 on MOF-74. Two pairs (labeled 1° and 2°) of absorption bands corresponding to v=0→1 are observed. Each pair consists of two distinct peaks, which were attributed to Q(1)(J=1→1) of o-H_2 and Q(0)(J=0→0) of p-H_2. As described in Sec. 4, o-H_2 in J=1 and p-H_2 in J=0 are clearly distinguished. The two pairs with different vibrational frequencies are H_2 bound to different sites. The spectral change shown in the figure, furthermore, represents time evolution of the IRAS. Evidently, Q(1) of o-H_2 is reduced in intensity, while the intensity of p-H_2 increases with increasing time indicating o-p conversion. The o-p conversion time is estimated to be the order of minutes. As the o-p conversion mechanism, the authors suspect presence of magnetic impurities, which induce o-p conversion as the one-step process via the magnetic dipole or Fermi contact interaction (Sec. 3.3). The authors also point out that the o-p conversion time on a different type of MOF (MOF-5) is 25 %/h much slower than that on MOF-74. No further analysis and discussion are given in the paper at present. It should be noted that the Zn-O electric dipole is exposed at the pore surface, which is similar to the amorphous ice surface. Therefore, the multi-step o-p conversion process as discussed for the ice surface might be operative on the MOF surface.

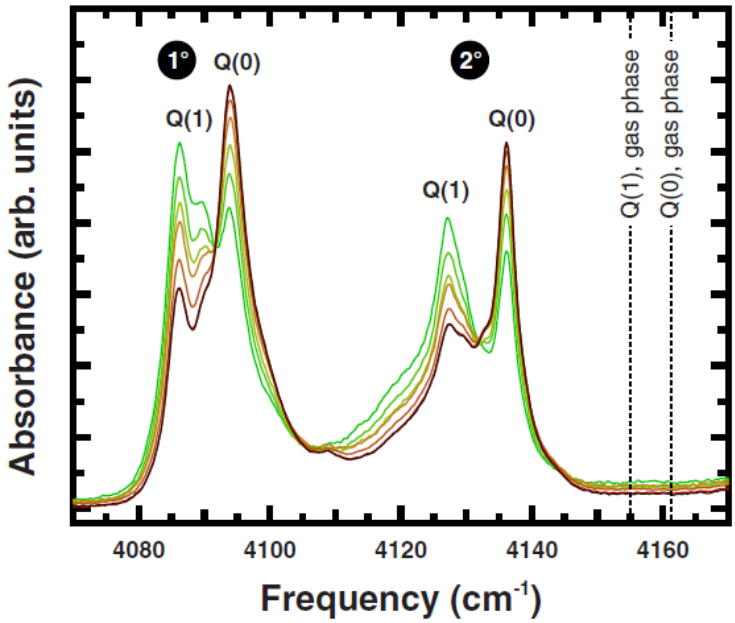

Figure 45: IRAS spectra taken for H_2 physisorbed on the pore surfaces of MOF-74 at 30 K. The absorption bands labeled 1° and 2° are assigned to different adsorption sites. Q(1) and Q(0) correspond to o-H_2 and p-H_2, respectively. Traces from green to brown are collected at t=55, 95, 135, 175, 280, 600, and 2700 s after H_2 loading. Q(1) is reduced in intensity, while the intensity of Q(0) increases with increasing time. Reproduced by permission from [204].

The IRAS spectra also revealed absorption bands corresponding to the S(0)(J=0→2) and S(1)(J=1→3) transitions. These bands are observed to be split due to the lifting of the rotational-state degeneracy under the anisotropic potential. The number of the splitting and relative absorption intensity are not consistent with the theoretical formula of Eq. 7, which are ascribed to possible ΔM selection in the IRAS observation [204]. The IRAS data for MOF-5 are compared with the recent theoretical work based on the first-principles calculations [65, 206].

5.2.4. Impurity-adsorbed Ice surfaces

Chehrouri et al. investigated o-p conversion of H_2 and p-o conversion of D_2 on an amorphous solid water (ASW) surface co-adsorbed with O_2 at 10 K by the REMPI-TPD method [226]. ASW samples were prepared by two

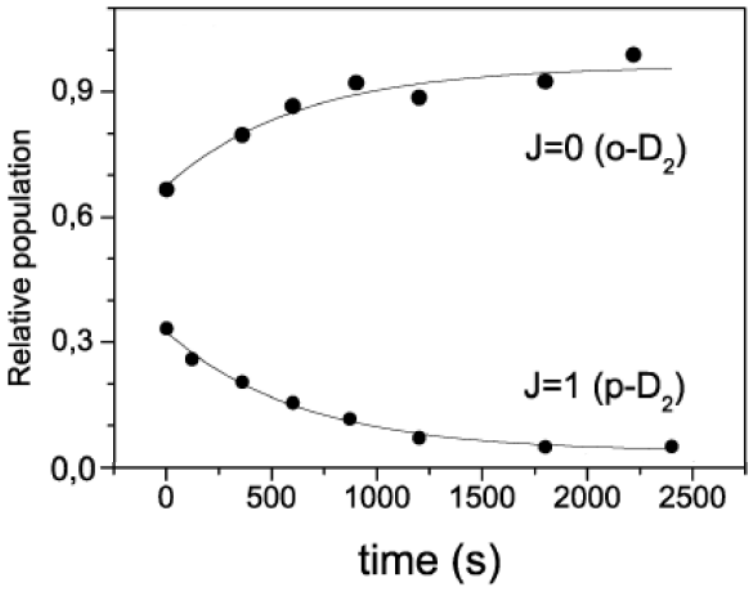

Figure 46: Time evolution of D_2 in p-D_2 ($J = 1$) and o-D_2 ($J = 0$) on porous ASW with 0.012 ML of co-adsorbed O_2 measured by REMPI-TPD. The J=1 intensity decreases while the J=0 intensity increases with increasing time. Adapted by permission from [226].

steps: the initial condensation of 250 ML of water on a Cu block at 120 K leading to compact non-porous ice film formation, and subsequent 12 ML porous ASW deposition at 10 K. After exposing the sample to O_2 at 25 K allowing sufficient diffusion of O_2 in porous ASW, n-H_2 was dosed to the sample at 10 K.

Figure 46 shows the time evolution of the J=0 and J=1 of D_2 on ASW with O_2 of 0.012 ML. The J=0 intensity increased while the J=1 intensity decreased with increasing residence time. By fitting a function of $A + B\exp(-t/\tau)$, the p-o conversion time of D_2 and o-p conversion time of H_2 at this O_2 coverage were estimated to be 600 ± 50 and 220 ± 50 s, respectively. Since the effective surface area of the ASW sample is larger than the flat surface by a factor of >5, the O_2 concentration was estimated to be as low as 0.2 %. The conversion times were similar to those observed on an O_2-adsorbed Ag surface [225], suggesting that the mechanism originating from the O_2 spin, as discussed in Sec 5.1.3, is operative on the O_2-adsorbed ASW.

It was pointed out that the asymptotic value (A) of J=1/J=0 for D_2 might be higher than the thermal-equilibrium value in gas phase (3×10^{-4}).

The origin of this difference was discussed to be the rotational-sublevel splitting of the J=1 state as shown in Fig. 9. The energy separation between the J=1 and 0 states gets smaller in the adsorption state compared to that of the gas phase due to the potential anisotropy, which results in enhanced population in $J = 1$ in thermal equilibrium compared to the gas phase. This is an interesting suggestion, and more accurate estimation of the asymptotic value is strongly required. On the other hand, the asymptotic value for H_2 was recognized to be too high and its possible origins were discussed to be either backconversion during TPD, presence of non-converting species, and background adsorption. At a low H_2 coverage, some molecules are trapped at a large-binding site because of a distribution of binding energies on ASW [55, 268], which suppresses the diffusion of H_2/D_2 to the neighboring site and hinders the spin conversion.

6. Astronomical relevance

Hydrogen is astronomically important, because it constitutes a significant fraction of the Universe, which includes stars and interstellar media (ISM). While the stars are hot and dense, ISM are cold and dilute with a typical density and temperature of 1 cm^{-3} and 100 K, respectively. The density and temperature of ISM are not uniform but dynamically changing spatially and temporally. Density fluctuation might cause further gravitational contraction eventually leading to star formation. Therefore, spatially-resolved observation of the density and temperature of ISM is of considerable importance for astronomical physics [27, 28].

6.1. Hydrogen in Molecular clouds: importance of surface processes

ISM consists of gas and dust, and the original main constituent of gas is atomic hydrogen. Figure 47(a) shows the main three steps of the evolution of hydrogen. As the first step, atomic hydrogen undergoes recombinative reaction forming molecular hydrogen on dust surfaces. This eventually leads to formation of molecular clouds with a temperature of about 30 K as the second step, which are regarded as a precursor state of star formation [28, 269]. Although the temperature of the molecular cloud is as low as 30 K, the surface part of the cloud is heated up to $\sim 10^3$ K by either radiation or particles incident to the molecular clouds in the astronomical environment as schematically shown in Fig. 47(c).

Figure 47(b) schematically illustrates the molecular processes taking place on the dust surfaces. It is worth emphasizing that the reaction of $H + H \rightarrow H_2$ is slow in gas phase and only occurs on solid surfaces. Two possible reaction paths for H_2 formation are the Eley-Rideal (ER) reaction where an impinging H atom directly reacts with adsorbed H or the Langmuir-Hinshelwood (LH) reaction where a weakly physisorbed H atom diffuses on the surface recombining with another H atom either physisorbed or chemisorbed on surfaces. H_2 molecules are vibrationally and rotationally excited upon H_2 formation because of the exothermic character of the reaction. An important question is the rotational-state distribution and OPR (ortho-para ratio) of nascent H_2 formed on the surfaces [270]. These would strongly depend on the dust surface structure, the adsorption site of H, the temperature, and so on.

When the H_2 molecules are cooled, they possibly interact with dust surfaces and undergo o-p conversion, which modifies the OPR of the molecular cloud. The time scale of the o-p conversion should depend on the magnetic and electronic structure of the dust surfaces and the sticking probability and residence time of H_2 on the dust surfaces. During the heating process of the surface part of molecular clouds, furthermore, H_2 might undergo o-p conversion again. During heating by radiation of either X-rays or far-ultraviolet radiation (FUV)), H_2 is once electronically excited and decays into the electronic ground state with simultaneous population of vibrationally and rotationally excited states [271]. The electronic excitation sometimes leads to dissociation of H_2, therefore this heated region is called photo-dissociated region or photon-dominated region (PDR). On the other hand, particles at a high velocity emitted from young stars and supernovae as called shocks are incident to molecular clouds and cause collisions with hydrogen molecules inducing excitation. As described in Sec. 3, o-p conversion does not occur by simple collision with other H_2 or excitation by radiation. The o-p conversion only occurs through interaction with dust surfaces or H^+ (and possibly H_3^+) in gas phase (Sec. 3.1). It should be noted that the chemical o-p conversion process on dust surfaces described in the introduction section could be important at high temperature as well as the physical o-p conversion.

As described in Sec. 2.1, the rotational-state distribution and OPR in a thermal equilibrium are expressed by the partition functions. Since the line intensity reflects the population of each rovibrational state, the temperature of the gas can be inferred from the spectral observation. On the other hand, the populations in the ortho and para states are not necessarily in thermal equilibrium with the environment, because the timescale of the o-p conversion

might be significantly longer than the timescale of the thermal change. The OPR therefore reflects the thermal history of the astronomical object [27, 28]. Spectroscopic measurements of molecular clouds are therefore highly required in the astronomical community, which are shown in the next section.

6.2. Astronomical observation

6.2.1. Light emission of H_2

The spectrum and line intensities of H_2 serve as a probe of the density and temperature. As detailed in Sec. 2.1, molecular hydrogen in the electronically ground state has no electric dipole moment. Therefore, light emission or absorption due to rotational and vibrational motion of hydrogen molecules is not induced by the electric dipole transition but originates from the electric quadrupole moment with a low oscillator strength. The quadrupole moment Q_m of an axially symmetric molecule is generally described as [272]

$$Q_m(R, \theta, \phi) = Q(R) Y_{2m}(\theta, \phi), \tag{28}$$

where the angular part is expressed by the spherical harmonics Y_{2m} with respect to the angle of the molecular axis. By considering the matrix element of Q_m with respect to two rotational states, the selection rule for the rotational transition is obtained as $\Delta J = 0, \pm 2$. When Q is expressed in the Taylor expansion of the intramolecular distance R, furthermore, the zero-th and first terms lead to the selection rule of $\Delta v = 0$ and ± 1, respectively. The energies and wavelengths for these transitions are listed in Table 5. From the viewpoint of astronomical observation, the emission due to vibrational de-excitation ($\Delta v = -1$) is transparent through air, whereas pure rotational transition ($\Delta v = 0$, $\Delta J = -2$) is air-opaque.

However, the rotational-excitation energy of molecular hydrogen is as large as 540 K (the J=0 $\rightarrow$ 2 transition energy). Most of the H_2 molecules in molecular clouds are therefore in the rotationally ground states and no emission is expected at a typical molecular cloud temperature of 30 K. This is in contrast to atomic H, which has a hyperfine splitting due to coupling of the nuclear spin and electron spin. Transition between the hyperfine levels yields emission with a wavelength of 21 cm, which has allowed a variety of astronomical observation. Although H_2 in molecular clouds is generally invisible, the surface part of molecular clouds at a temperature of $\sim 10^3$ K shown in Fig. 47(c) yields emission of H_2. The emission spectra of H_2 originating from the rotational and vibrational levels have been reported

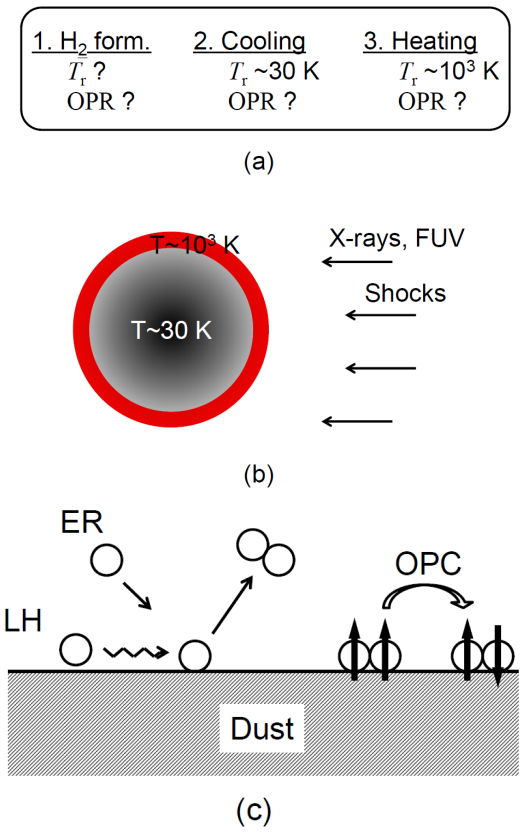

Figure 47: Schematic illustration of (a) evolution of hydrogen, (b) cross-section of a molecular cloud and heating of the cloud surface and (c) molecular processes on dust surfaces, during formation of molecular clouds. In the first step, H_2 is formed from atomic hydrogen on dust surfaces via the either Eley-Rideal (ER) reaction or Langmuir-Hinshelwood (LH) reaction. In the next steps, H_2 is cooled to about 30 K forming molecular clouds, while the surface part of the clouds are heated by radiation or collision. The OPR in these processes are of interest and importance, the dust surfaces playing a role to induce the o-p conversion.

for a variety of heated regions of molecular clouds. The observation results relevant to OPR are reviewed in the next subsection.

6.2.2. Observational spectra

The rotational spectra of the vibrationally excited states were first reported for a molecular cloud named the NGC2023 nebula [273]. The emission lines originating from the vibrational transitions, which lie in the air-transparent region, were detected by the ground-based infrared telescope in Hawaii. As described in Sec. 2.1, the vibrational wavefunction of H_2 does not change its sign with respect to the two-nuclei permutation, which means the ortho and para species can be defined in the same way as the vibrational ground state. Figure 48 shows the Boltzmann plot of the rovibrational-state intensities often designated as a (ro)vibrational-energy diagram, where the intensity divided by the nuclear-spin and rotational degeneracy is plotted as a function of the rovibrational energy. From the relative population of the v=1 and 2 states, the vibrational temperature of 3600 K was derived. In the v=2 state, while the relative populations of J=2 and 4 and J=3 and 5 reveal a rotational temperature of 1500 K, the ortho (J=odd) and para (J=even) populations are evidently not in equilibrium with each other. The OPR was estimated to be 1.4 – 2.0, which corresponds to a nuclear-spin temperature of 95 – 120 K in Fig. 7. If the ortho and para states were in equilibrium with a temperature of 1500 K, the OPR should be 3. Following this work, the OPR value was investigated for several nebulas through observation of the S branches ($\Delta J = -2$) of $v = 1 \rightarrow 0$, i.e. $J = 2 \rightarrow 0$ and $J = 3 \rightarrow 1$ transitions. The OPR values evaluated from the line intensities ranged from 1 to 2.5 [274, 275, 276, 277, 278, 279, 280, 281].

Additionally, in a dense and cold region of a molecular cloud, absorption of the background light due to vibrational excitation (v=0 - 1) of J=0 (para) and J=1 (ortho) was observed toward a nebula of NGC2024. The J=1 to J=0 ratio was smaller than 0.8, which is roughly consistent with the molecular temperature of $\sim$ 30 K [282] (Fig. 7).

In later work, however, it was pointed out that the OPR in the vibrationally excited state possibly deviates from the real OPR of the molecular cloud because of the different optical depth of the ortho and para species [284].

To that end, the air-opaque IR emission corresponding to the pure rotational transitions has been observed to probe the OPR in the vibrationally ground state. The Orion bar region was first studied by a ground-based

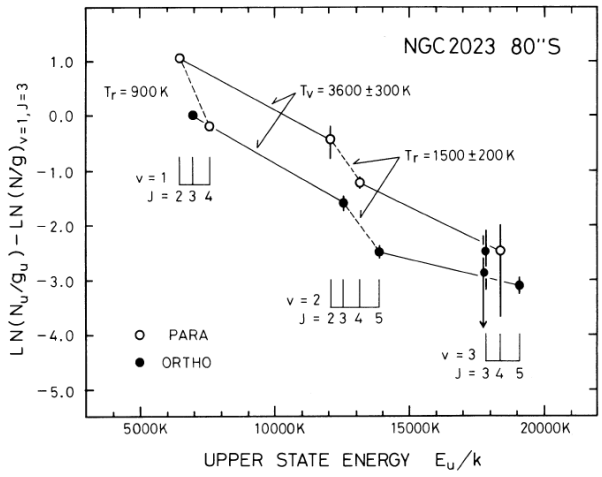

Figure 48: Boltzmann plot of the rovibrational-level population of H_2 observed for the NGC2023 nebula by a ground-based infrared telescope. The rotational temperatures obtained from the dashed lines and vibrational temperatures evaluated from the solid lines are shown in the figure. The populations of o-H_2 and p-H_2 are not in thermal equilibrium with the rotational temperatures, and the OPR is 1.4 – 2.0. Adapted with permission from [273].

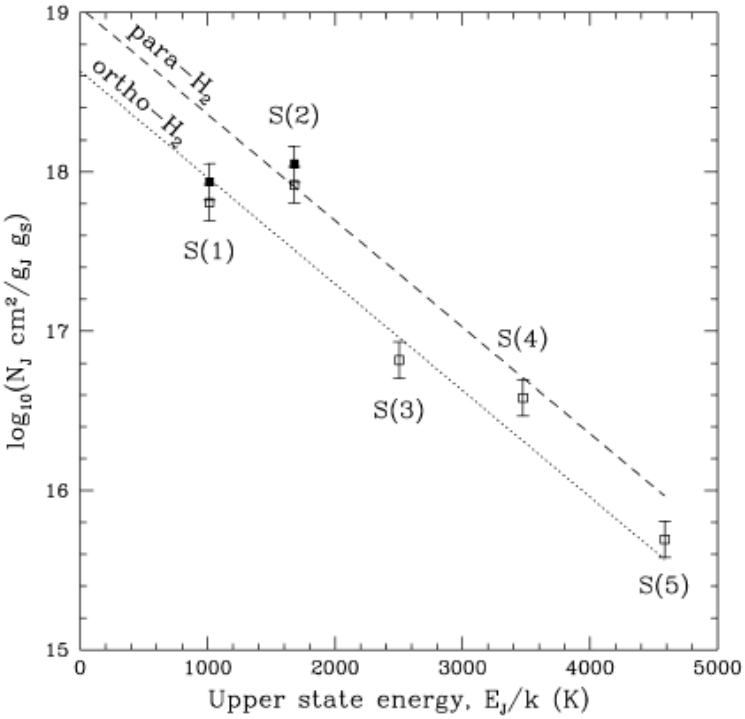

Figure 49: Boltzmann plot of the rotational-level population of H_2 in J=3–7 for a Herbig Hallo object of HH54 as observed by ISO. Straight lines show the fit for a gas temperature of 650 K and an OPR of 1.2 [283].

infrared telescope, and the ratio of J=3 and J=4 was reported to be 0.5 – 3.6 [285, 286] though the sensitivity was limited. Owing to the infrared astronomical satellite named the Infrared Space Observatory (ISO), which was launched in 1995, the pure rotational emission lines of H_2 in v=0 were successfully measured with a high sensitivity [287]. An overview of the data acquired by ISO for a plenty of heated regions of molecular clouds such as shocked regions and PDR's of nebulas are given in a review article by Habart et al. [28]. Some of the typical results are briefly shown in the following.

Figure 49 shows the rotational-energy diagram observed for a Herbig Hallo object named HH54 [283]. Herbig Hallo objects are shock-heated ISM's near newly-born stars. The straight line represents a rotational temperature of 650 K. As clearly seen in the figure, the ortho and para state populations are not on the same line, indicating that the two species are not in thermal equilibrium with the rotational temperature. The OPR value was estimated to be 1.2, which corresponds to a nuclear-spin temperature of lower than 90 K (Fig. 7).

A comprehensive set of the rotational and rovibrational lines in the wavelength range of 2.4 – 45 μm was observed for the Orion molecular cloud, OMC-1 [288], which is shown in Fig. 50(a). In addition to the H_2 lines for v=0 – 2 and J=1– 25, emission lines due to other elements such as Si, S, and Ne were identified. Figure 50(b) shows the rovibrational energy diagram of H_2, where the level population was well described by a sum of five Boltzmann distributions with temperatures of about 600 – 3000 K as shown by the dotted curve. Since all rovibrational states are on the same curve, the OPR of this cloud was concluded to be 3.

While another shock-heated region of HH2 was found to have an OPR of 1.2–1.6 [289], most shocked regions are reported to have an OPR value of 3 [290, 291, 292, 293, 294]. The H_2 spectra were also observed for a PDR named the ρ Ophiuchi molecular cloud [295]. The spectrum was measured in a spatial-resolved manner, and revealed a rotational temperature of about 300 K. It was also shown that the OPR was significantly smaller than 3. Smaller OPR values were similarly observed for NGC7023 [296] and galactic center [297].

After ISO completed its mission, Spitzer Space Telescope (SST) was launched in 2003, and has reported H_2 spectral data with higher spatial resolution from various molecular clouds. Figure 51 shows the rotational-energy diagram observed towards the shock-heated regions of HH54 and HH7–11 [298]. The diagram revealed a zigzag feature indicating that the ortho and

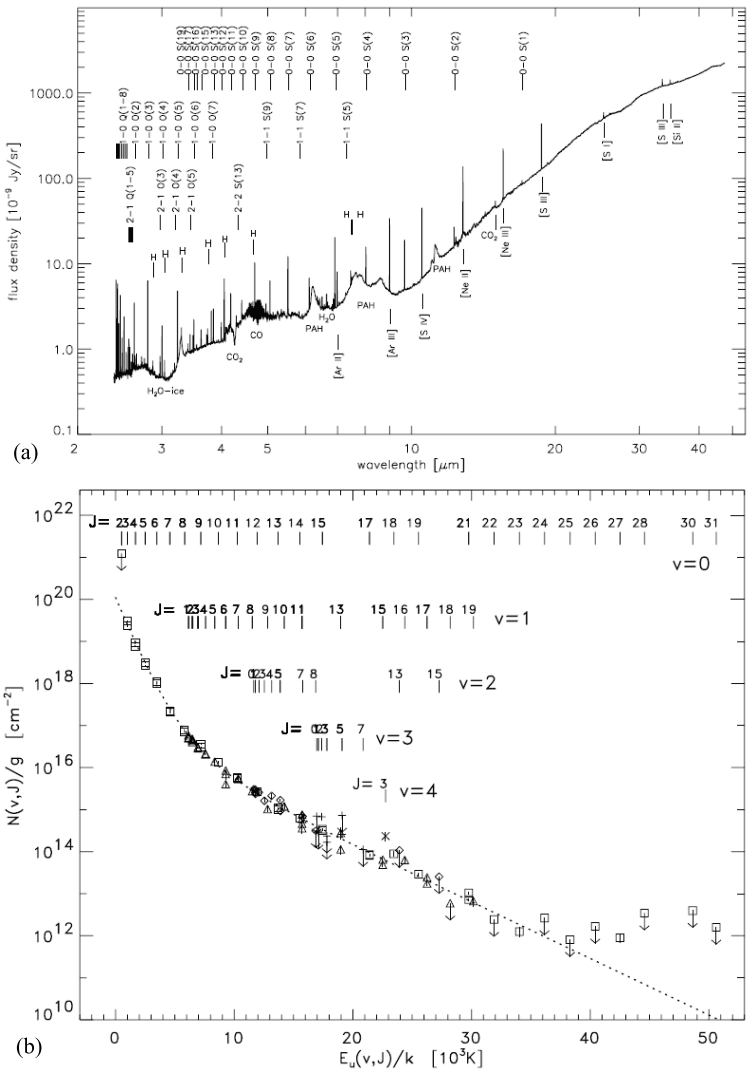

Figure 50: (a) Spectrum in the wavelength range of 2.4 – 45 μm observed for the Orion molecular cloud of OMC-1 by ISO. (b) Boltzmann plot of the extinction-corrected rovibrational-level intensity obtained from (a). Rovibrational-energy positions for the v=0–4 and various J states are shown in the figure. The OPR is evaluated to be 3. Reproduced with permission from [288].

para states are not in equilibrium with the gas temperature. The rotational-state distribution was well expressed by two components with temperatures of 400 – 550 K and OPR of 1.5 – 2. The rotational temperature and OPR value derived from the J=4 –7 intensities were two-dimensionally mapped for the two directions as shown in Fig. 52(a). It is apparent that the rotational temperature and OPR value vary depending on the position in the object. While the rotational temperature is 600 – 1000 K, the OPR changes from 0.5 – 3. Figure 52(b) displays the correlation between the OPR and rotational temperature obtained from two-component fits, where the OPR was plotted as a function of the rotational temperature. The OPR values tend to increase as the rotational temperature increases. The orange curve represents the thermal equilibrium, and the black curve displays the simulated result on the assumption of the initial OPR of 0.4 (HH54) and 0.25 (HH7) followed by o-p conversion via the proton exchange mechanism (Sec. 3.1).

HH 7-11 are Herbig-Haro objects in the Perseus molecular cloud, and associated with the NGC 1333 star-forming region. The NGC 1333 region was also investigated by Spitzer in detail [299]. The measured rotational-energy diagrams were analyzed with two components. While the obtained rotational temperatures were 300 – 600 K and 1000 – 1500 K, the OPR's were 0.3 – 0.7 and 1.4 –2, respectively. The rotational temperature and OPR were precisely mapped in detail similarly to Fig. 52. The outflows associated with star formation were also analyzed in detail. Whereas the OPR of L1448, BHR71, NGC2071, and L1157 [300, 301, 302] were significantly smaller than 3, those of IRAS 16253-2429 protostar and HH211 were found to be 3 [303, 304].

The rotational temperature and OPR were also investigated for photon-heated PDR regions of molecular clouds. The PDR is characterized by the strength of the radiation field, and six galactic PDR's named L1721, California, N7023E, Horsehead, ρ Oph and N2023N at different excitation conditions were analyzed in detail [269]. As demonstrated for shock-heated regions, the rotational-energy diagram was expressed by two temperature components, where the temperatures for the low-J and high-J regions were 200 – 300 K and 300 – 700 K, respectively. The OPR value of the low-J and high-J regions was 1 – 1.6 and 2.6, respectively. The rotational temperature was confirmed to be higher than the value expected from a model calculation, which was also observed for a reflection Nebula of NGC2023 with a low OPR of 1.68 [305]. The rotational spectrum was further investigated for a lower excitation condition [306]. The next generation Herschel Space Observatory

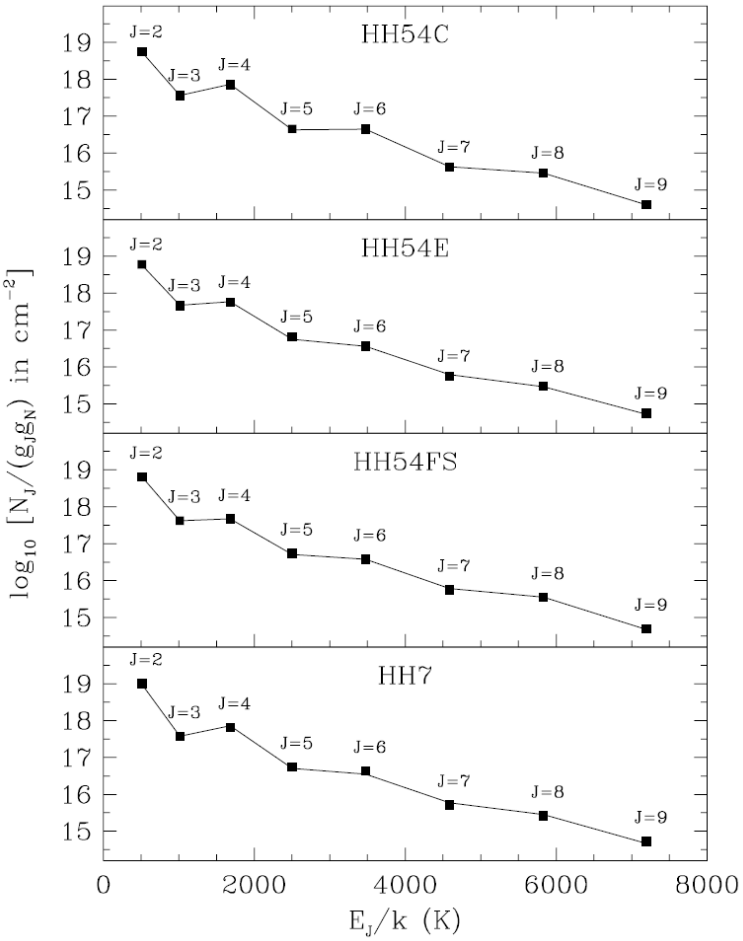

Figure 51: Boltzmann plot of the rotational-level population observed toward different directions of HH54 and HH7. The solid lines show the two-component fit to the observations, and the OPR is estimated to be 1.5 – 2. Reproduced with permission from [298].

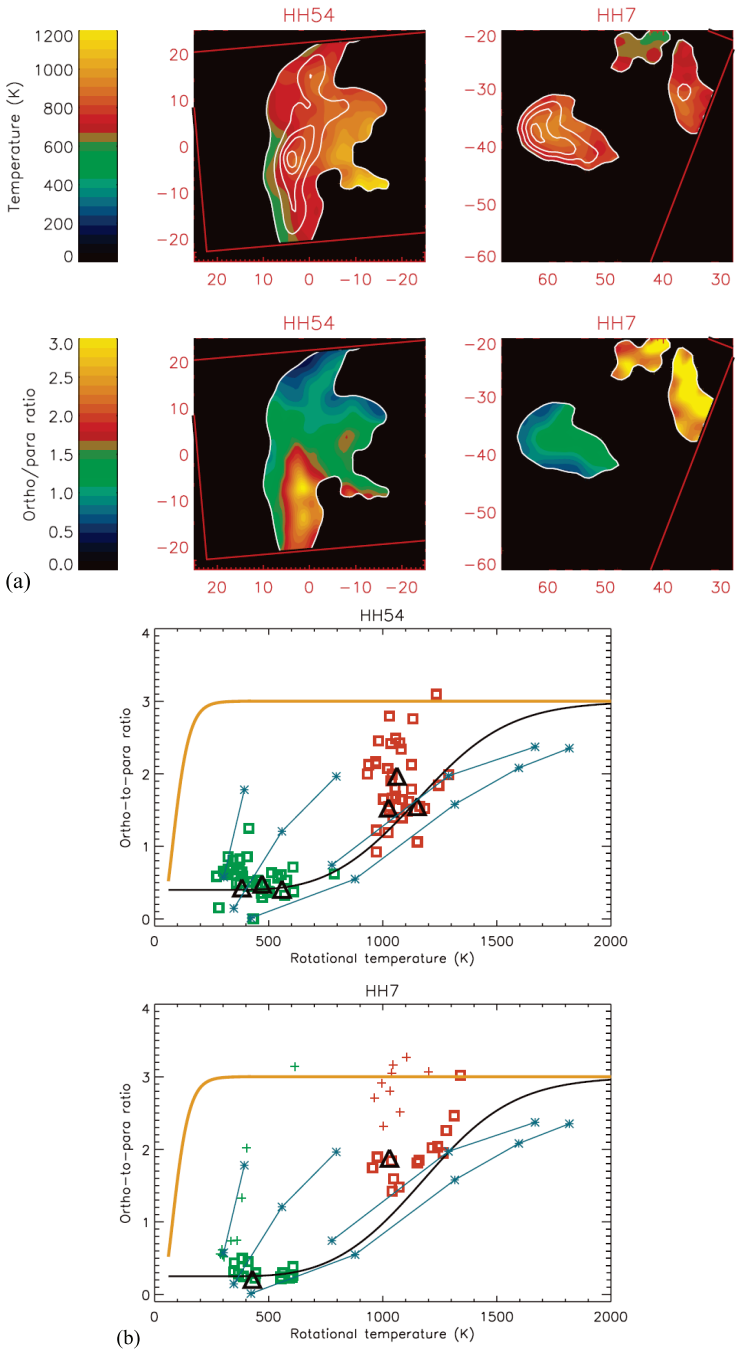

Figure 52: (a) Mapping of the rotational temperature and OPR towards HH54 and HH7. The horizontal and vertical axes are the right ascension and declination offsets in arcseconds relative to a certain direction. (b) Correlation of the OPR and rotational temperature. Triangles are from a two-component fit to the rotational-level population shown in Fig. 51. Other data points apply to 5"×5" square subregions within the source regions shown in (a), green and red referring, respectively, to the warm and hot gas components. The orange curve represents the thermal equilibrium, and the black curve displays the simulated result on the assumption of the initial OPR of 0.4 (HH54) and 0.25 (HH7) followed by o-p conversion via the proton exchange mechanism. Reproduced with permission from [298].

will provide us with new observation data.

6.3. Ortho-para ratio of nascent H_2 and ortho-para conversion

As discussed for Fig. 47, the initial OPR value when H_2 is formed is of particular importance. Since the formation of H_2 molecules is an exothermic process, part of the energy released in the chemical bond formation is partitioned in the internal energy of nascent H_2. In recent years, the rotational-state distribution and OPR have been investigated by laboratory experiments and theoretical studies, which are reviewed along with discussion on possible o-p conversion in an astronomical environment.

6.3.1. H_2 formation

Most H_2 is thought to be produced on surfaces of interstellar grains [307, 308]. We first discuss why H_2 formation is slow in gas phase. In gas phase, two possible configurations when two hydrogen atoms come closer are the electron spin triplet and singlet states. The triplet state of $b^3\Sigma_u^+$ is a repulsive state, and the radiative-transition to the ground state $X^1\Sigma_g^+$ is spin-forbidden with a lifetime of much longer (by a factor of 10^8 – 10^{10}) than the ordinary dipole allowed transition of $\sim 10^{-9}$ s [309, 307]. The spin singlet configuration, on the other hand, corresponds to a vibrationally continuum unbound state in the electronically ground state. As H_2 in the $X^1\Sigma_g^+$ state has no electric dipole, the radiative transition probability should be small. The vibrational period of $\sim 10^{-14}$ s is much shorter than the lifetime of these states, hence, the recombination efficiency becomes extremely small [310].

Recombinative desorption and its reverse process of dissociative chemisorption of H_2 on metal surfaces have been a topic of intensive studies in the last decades in Surface Science. Hydrogen atoms are chemisorbed on most metals with a typical chemisorption energy of 0.5 eV, and the dynamics of recombinative desorption/ dissociative adsorption was investigated on the basis of multi-dimensional potential energy surfaces. As detailed in the Surface Science textbooks and several review articles [311, 312, 313, 314, 315, 316, 317], a considerable progress has been made for the understanding of the dynamics of desorption and adsorption on metal surfaces. Since the chemisorption energy is large, the recombinative desorption occurs at temperatures of higher than 100 K, which is not of direct relevance to the astronomical condition.

When two H atoms encounter, four possible nuclear-spin configurations are

$$|\frac{1}{2}\rangle + |\frac{1}{2}\rangle,\ |-\frac{1}{2}\rangle + |-\frac{1}{2}\rangle,\ |\frac{1}{2}\rangle + |-\frac{1}{2}\rangle,\ |\frac{1}{2}\rangle + |-\frac{1}{2}\rangle.$$

Very naively, it is expected that the former two configurations lead to o-H_2 formation, whereas the latter two result in o-H_2 and p-H_2 with the same probability. When there is no particular $J-$selection in H_2 formation and the rotational-state is described by a Boltzmann distribution with a certain temperature, the OPR becomes in thermal equilibrium with the rotational temperature. If there were some tricks operative to polarize or select the proton nuclear-spin during H_2 formation, the OPR would be affected in favor of o-H_2 formation. It should be noted, however, that the electron spin of an H atom is coupled through hyperfine interaction with the proton spin forming either total spin singlet or triplet states. Hence, the H_2 formation process should be described as the four-spin dynamics. This might strongly depend on the adsorption state of H, because the H electron spin is retained in the physisorbed state while it tends to form a singlet state through chemical bond formation with substrate electrons in the chemisorbed state.

As an experimental approach, the H_2 formation rate and its mechanism on the surfaces of ISM such as graphite, amorphous ice and silicate have been investigated as reviewed in the articles by Williams et al. [318] and Watanabe and Kouchi [319]. Recent studies on the OPR and internal-state distribution of H_2 from physisorbed states on surfaces are briefly reviewed below.

The OPR of the newly formed H_2 from spin-polarized H atoms was investigated by NMR. It is known that the NMR spin relaxation time is a function of the ortho concentration of solid H_2, which allowed to measure the OPR of H_2 recombined on liquid He surfaces. According to this study, the OPR formed from H atoms with random spin orientation was estimated to be 0.2, while the spin-polarized H atoms yielded 100 % pure o-H_2 [320].

By applying the rotational-state-resolved techniques, the internal-energy distribution was measured for molecular hydrogen formed on graphite [321, 322, 323]. Atomic H and D beams were supplied to the surface at 15 – 50 K, and resultant H_2 and HD molecules formed on the surface were state-selectively detected. The product molecules were in the vibrationally excited states of v=1 – 7. For v=1 and 2, the rotational distribution in J=0 – 4 revealed a rotational temperature of about 300 K, which was furthermore found to be independent of the surface temperature of 15 – 50 K [321]. The rotational temperature of higher v states was also examined experimentally, which were similar to those of v=1 and 2 states [322, 323]. In these studies, the rotational-state distribution seemed to be described by a Boltzmann distribution, which suggests no particular selection between even and odd J

states. The OPR of H_2 formed on graphite, therefore, was considered to be 3.

The internal-state distribution of nascent H_2 was also investigated on amorphous ice surfaces [324, 325, 257, 326]. During atomic H dosage onto amorphous ice at 8 K, H_2 formed on the surface in J=1 and 0 was detected by REMPI, and the ratio of these species was consistent with an OPR value of 3 [257]. The OPR was also examined for both H_2 and D_2 formed on amorphous ice at 10 K [326]. In this work, either atomic H or D was supplied to the sample surface and product H_2 or D_2 formed on the ice surface was detected by REMPI. By comparing the populations in J=1 and 0, the OPR of H_2 and D_2 was evaluated to be 2.91 $\pm$ 1.23 and 1.44 $\pm$ 0.43, respectively. Although the experimental uncertainty was large due to the background signal and experimental difficulty, these OPR values were claimed to be consistent with the high-temperature limit of 3 (H_2) and 2 (D_2).

Theoretically, the rotational-state distribution upon H_2 formation was first simply assumed to be in thermal equilibrium with the surface temperature or the effective temperature corresponding to the energy released in the rotational degree of freedom [327, 328]. An interesting theoretical approach was application of the resonance theory for atom recombination. The highest vibrational level of H_2 is the v=14 state. At high vibrational levels, the total internal energy goes beyond the dissociation energy with high rotational states, referred to as quasibound states or orbiting resonances because of the bound nature within the centrifugal limit [329]. The orbiting resonance theory for atom recombination considers that two atoms are scattered into such quasibound states followed by rotational deexcitation to bound states [330, 331, 332]. This idea was also applied to hydrogen recombination for physisorbed systems on Xe crystal surfaces [333], where two hydrogen atoms were assumed to move freely on the surface and undergo collisions forming quasibound states. The surface serves to conserve the energy and momentum of the system while H_2 falls into a true bound state. The surface corrugation is important providing coupling between different degrees of freedom. Two dominant resonances are the (v=14, J=5) and (v=13, J=8) states, which correspond to the ortho and para states. The resonance probabilities then determine the OPR of H_2 formed on surfaces.

A more elaborate theoretical approach is being conducted in recent years. As successfully performed on metal surfaces, the hydrogen recombinative reaction is essentially governed by the multidimensional potential energy surface (PES) and dynamics of atoms on the PES. Description of PES and clas-

sical or quantum dynamics of hydrogen atoms have recently been performed on the surface of graphite. As an LH reaction illustrated in Fig. 47(b), PES for two physisorbed H atoms on graphite was described semiempirically or by first-principles calculations, and the H_2 formation probability and rovibrational state distribution in the final state were quantum-mechanically simulated as a function of the collision energy [334, 335, 336, 337]. It was shown that the product H_2 is strongly excited in the vibrational motion and the rotational motion is moderately excited with an OPR value of around 3. The reaction dynamics of the ER type was also investigated in detail. The PES was obtained by first-principles density functional theory (DFT) [338, 339, 340, 341, 342, 343], and model potentials were occasionally used by fitting to the DFT potential [344]. On the basis of these PES's, the reaction dynamics was investigated at a variety of conditions [345, 346, 339, 347, 348, 340, 349, 344, 350, 341, 351, 352, 353, 342], e.g., the initial state of the preadsorbed H, either chemisorbed [344], physisorbed [350], or paired with another H on graphite [348, 341], the substrate relaxation effect [340], relation with other reaction paths of collision-induced desorption and trapping as well as the ER reaction [349], and isotope effects [347]. All these studies showed the product H_2 is strongly excited vibrationally, sometimes occupying a particular vibrational state. Although the rotational-state distribution has not been thoroughly investigated as vibrational excitation, the reaction probability to form ortho and para species was similar in the ER reaction [345]. Further theoretical studies are expected to clarify the final-state distribution and resultant OPR on various ISM surfaces in the near future.

6.3.2. Ortho-para conversion

The H_2 molecules in molecular clouds are cooled to $\sim$30 K from the nascent hot condition, yet the surface part of the clouds is heated by radiation or collision (Fig. 47). Without o-p conversion during cooling and heating processes, the OPR in the nascent condition would be retained. During the thermal processes, however, H_2 interacts with the surfaces of cosmic dusts consisting of carbon, water, silicates and so on, and possibly undergoes o-p conversion.

In considering the o-p conversion on dust surfaces, the collision rate γ, sticking coefficient S_t and residence time t_R of H_2 on the surfaces are important. Since the typical desorption temperature of H_2 is lower than 30 K, t_R might be shorter than the o-p conversion time τ. The number of the

physisorbed o-H_2 decreases by either desorption from the dust surface with a probability of t_R^{-1} or o-p conversion with a probability of τ^{-1}. Therefore, the overall conversion probability P is described as

$$P = S_t \gamma \frac{\tau^{-1}}{t_R^{-1} + \tau^{-1}}. \tag{29}$$

As discussed in Sec. 2.2.3, S_t is typically of the order of 0.1. On the other hand, t_R changes exponentially as $t_R = t_0 \exp(E_d/kT)$ (t_0 $\sim 10^{-11}$ s), and might be as short as 10^{-6} s at 30 K and a physisorption energy of 30 meV. As described in Sec. 5, the microscopic o-p conversion times of H_2 in the physisorption state of amorphous ice and graphite were obtained to be $\sim 10^3$ s or shorter (Secs. 5.1.4 and 5.2.1). Although the conversion data on oxides like silicates are not available to date, the electric-field induced multi-step mechanism could be operative on those surfaces. On the other hand, the collision rate is described by the product of the dust size σ, mean velocity of H_2 and dust density [37]. On the assumption of the dust size of $\sim 10^{-12}$ cm^2, the mean velocity of $\sim 10^5$ cm s^{-1} , and dust density of ~ 1 cm^{-3} [269], γ leads to 10^{-7} s^{-1}, and the overall o-p conversion probability is roughly estimated to be 10^{-17} s^{-1} for ASW. If some magnetic impurities like O_2 and H are present on the surfaces, the overall o-p conversion probability could be enhanced to 10^{-14} s^{-1}. Since the physisorption energy depends on the local atomic structure, as discussed by Bourlot [29], the overall conversion probability is strongly temperature-dependent and might be further enhanced if H_2 is strongly bound and the residence time is longer. As these timescales are similar to the timescale of the thermal process of molecular clouds ($\sim 10^{15}$ s), the o-p conversion on surfaces might have significant effects on the OPR of the molecular clouds.

Another important o-p conversion channel in the heated region is the $H_2 + H^+$ reaction via proton exchange described in Sec. 3.1. The o-p conversion rate via the proton exchange was roughly evaluated to be $\sim 10^{-16}$ s^{-1} for a particular condition [354], and analysis has been performed for various astronomical parameters [354, 355, 356, 357]. Proper modeling on the basis of these time scales of the microscopic molecular processes would elucidate the origin of the astronomical data and dynamical evolution of molecular hydrogen.

7. Concluding remarks

We have reviewed recent progress on the physisorption and o-p conversion of molecular hydrogen along with basic concepts of the ortho-para conversion of molecular hydrogen. In spite of the recent advances, experimental data on various surfaces are still missing and quantitative verification of the conversion theory including magnetic interaction and energy dissipation is strongly required. We have also tried to provide astronomical observation data relevant to ortho-para conversion, which will hopefully be understood on the basis of the microscopic knowledge acquired in Surface Science.

8. Acknowledgement

The authors thank T. Okano, K. Niki and K. Yamakawa for fruitful discussion, and support by a Grant-in-Aid for Scientific Research by Japan Society for the Promotion of Science.

Appendix A. Matrix element of $\vec{i}$

$$
\begin{aligned}
< \chi_n(I=0)| \;\; i^- \;\; |\chi_n(I=1,I_z=+1)> & \\
&= \frac{1}{\sqrt{2}}(<\frac{1}{2}\;-\frac{1}{2}|-<-\frac{1}{2}\;\frac{1}{2}|)(i_a^- - i_b^-)|\frac{1}{2}\;\frac{1}{2}> \\
&= \frac{1}{\sqrt{2}}(<\frac{1}{2}\;-\frac{1}{2}|-<-\frac{1}{2}\;\frac{1}{2}|)(|-\frac{1}{2}\;\frac{1}{2}>-|\frac{1}{2}\;-\frac{1}{2}>) \\
&= -\sqrt{2} \qquad \text{(A.1)}
\end{aligned}
$$

$$
\begin{aligned}
< \chi_n(I=0)| \;\; i^z \;\; |\chi_n(I=1,I_z=0)> & \\
&= \frac{1}{2}(<\frac{1}{2}\;-\frac{1}{2}|-<-\frac{1}{2}\;\frac{1}{2}|)(i_a^z - i_b^z)(|\frac{1}{2}\;-\frac{1}{2}>+|-\frac{1}{2}\;\frac{1}{2}>) \\
&= \frac{1}{2}(<\frac{1}{2}\;-\frac{1}{2}|-<-\frac{1}{2}\;\frac{1}{2}|)(|\frac{1}{2}\;-\frac{1}{2}>-|-\frac{1}{2}\;\frac{1}{2}>) \\
&= 1 \qquad \text{(A.2)}
\end{aligned}
$$

Appendix B. Fermi contact interaction

The matrix element of the Fermi contact interaction for the XY and UY processes is considered. In the XY process, the intermediate and final states are electron triplet ($^3\Sigma_u^+$) and singlet ($^1\Sigma_g^+$) states, which correspond to $(1s\sigma_g)^1(2p\sigma_u)^1$ and $(1s\sigma_g)^2$ electron configurations, respectively. The orbital part of the wavefunction is described as

$$\begin{aligned} |^1\Sigma_g^+\rangle &= \chi_e(S=0)\phi_g(\vec{r}_1)\phi_g(\vec{r}_2) \\ |^3\Sigma_u^+\rangle &= \chi_e(S=1)\frac{1}{\sqrt{2}}(\phi_g(\vec{r}_1)\phi_u(\vec{r}_2)-\phi_g(\vec{r}_2)\phi_u(\vec{r}_1)), \end{aligned} \tag{B.1}$$

where ϕ_g and ϕ_u represent the orbitals of $1s\sigma_g$ and $2p\sigma_u$, respectively, and $\chi_e(S=1)$ and $\chi_e(S=0)$ denote the electron spin triplet and singlet functions, respectively.

Since the H_2 molecule has two electrons, the orbital integral must be done for the two electron position vectors.

$$\begin{aligned} \langle ^3\Sigma_u^+|H_{FC}|^1\Sigma_g^+\rangle &= \langle\frac{1}{\sqrt{2}}(\phi_g(\vec{r}_1)\phi_u(\vec{r}_2)-\phi_g(\vec{r}_2)\phi_u(\vec{r}_1))| \\ &\quad \sum_{j=1,2\ K=a,b} \vec{s}_j\cdot\vec{i}_K\delta(\vec{r}_j-\vec{R}_K)|\phi_g(\vec{r}_1)\phi_g(\vec{r}_2)\rangle \end{aligned} \tag{B.2}$$

Among the four terms of the Fermi contact Hamiltonian, integration of $\vec{s}_1\cdot\vec{i}_a\delta(\vec{r}_1-\vec{R}_a)$ over $\vec{r}_1$ and $\vec{r}_2$ leads to λ_{IFC} by using the relation of $\langle\phi_g(\vec{r})|\phi_u(\vec{r})\rangle = 0$ as

$$\begin{aligned} \lambda_{IFC} &= -\int\phi_g(\vec{r})\delta(\vec{r}-\vec{R}_a)\phi_u(\vec{r})d\vec{r} \\ &= -\phi_u(\vec{R}_a)\phi_g(\vec{R}_a) \end{aligned} \tag{B.3}$$

On the other hand, integration of the term $\vec{s}_1\cdot\vec{i}_b\delta(\vec{r}_1-\vec{R}_b)$ results in $-\phi_u(\vec{R}_b)\phi_g(\vec{R}_b)$. While $\phi_g(\vec{R}_a)=\phi_g(\vec{R}_b)$ because of the gelade character, $\phi_u(\vec{R}_a)=-\phi_u(\vec{R}_b)$ due to the ungelade nature. Therefore, the sum of the two terms leads to $\lambda_{IFC}\vec{s}_1\cdot(\vec{i}_a-\vec{i}_b)$. Similarly, $-\lambda_{IFC}\vec{s}_2\cdot(\vec{i}_a-\vec{i}_b)$ is obtained by calculation of the other two terms, hence Eq. 26 is obtained.

In the UY process, the intermediate and final states are electron triplet and singlet states with configurations of $(1s\sigma_u)^1(k)^1$ and $(k)^1(k')^1$, respectively, where k and k' denote the substrate states. The orbital part of the

wavefunction is described as

$$|^1I\rangle = \chi_e(S=0)\frac{1}{\sqrt{2}}(\phi_k(\vec{r}_1)\phi_u(\vec{r}_2)+\phi_k(\vec{r}_2)\phi_u(\vec{r}_1)) \quad \text{(B.4)}$$

$$|^3f\rangle = \chi_e(S=1)\frac{1}{\sqrt{2}}(\phi_k(\vec{r}_1)\phi_{k'}(\vec{r}_2)-\phi_k(\vec{r}_2)\phi_{k'}(\vec{r}_1)). \quad \text{(B.5)}$$

Although integration of the Fermi contact Hamiltonian is more complicated than the intramolecular case, the surface-molecule Fermi contact coefficient λ_{SFC} proportional to the $(\vec{s}_1-\vec{s}_2)\cdot(\vec{i}_a-\vec{i}_b)$ term is given by

$$\begin{aligned}\lambda_{SFC} = & -\phi_u^*(\vec{R}_a)(\phi_{k'}(\vec{R}_a)+\phi_{k'}(\vec{R}_b))/2 \\ & +\phi_u^*(\vec{R}_a)(\phi_k(\vec{R}_a)+\phi_k(\vec{R}_b))/2\int\phi_k^*(\vec{r})\phi_{k'}(\vec{r})d\vec{r} \\ & +(|\phi_k(\vec{R}_a)|^2-|\phi_k(\vec{R}_b)|^2)/2\int\phi_u^*(\vec{r})\phi_{k'}(\vec{r})d\vec{r} \\ & -(\phi_k^*(\vec{R}_a)\phi_{k'}(\vec{R}_a)-\phi_k^*(\vec{R}_b)\phi_{k'}(\vec{R}_b))/2\int\phi_u^*(\vec{r})\phi_k(\vec{r})d\vec{r}. \quad \text{(B.6)}\end{aligned}$$

When this term is integrated over the rotational wavefunctions, only the first and second terms in B.6 are significant by using the relation of $\langle Y_{J,m}|\phi_k(\vec{R}_a)|Y_{J,m}\rangle = \langle Y_{J,m}|\phi_k(\vec{R}_b)|Y_{J,m}\rangle$ and $\langle Y_{J,m}|\phi_{k'}(\vec{R}_a)|Y_{J,m}\rangle = \langle Y_{J,m}|\phi_{k'}(\vec{R}_b)|Y_{J,m}\rangle$.

Appendix C. Spin-orbit interaction

When the two electrons in H_2 are in the $(1s\sigma_g)^1(nl\pi)^1$ configuration, the resulting state can be either a singlet ($|^1\Pi\rangle$) or triplet ($|^3\Pi\rangle$) state, of which orbital part of the wavefunctions are described in a first approximation as,

$$|^1\Pi\rangle = \frac{1}{\sqrt{2}}(\phi_\sigma(\vec{r}_1)\phi_\pi(\vec{r}_2)+\phi_\sigma(\vec{r}_2)\phi_\pi(\vec{r}_1))$$

$$|^3\Pi\rangle = \frac{1}{\sqrt{2}}(\phi_\sigma(\vec{r}_1)\phi_\pi(\vec{r}_2)-\phi_\sigma(\vec{r}_2)\phi_\pi(\vec{r}_1)) \quad \text{(C.1)}$$

$$, \quad \text{(C.2)}$$

where $\phi_\sigma(\vec{r})$ and $\phi_\pi(\vec{r})$ represent the orbitals of $1s\sigma_g$ and $nl\pi$. Since $\phi_\sigma(\vec{r})$ and $\phi_\pi(\vec{r})$ have the axial component of the orbital angular momentum of 0 and 1, $\langle\phi_\sigma|\ell_z|\phi_\sigma\rangle = 0$ and $\langle\phi_\pi|\ell_z|\phi_\pi\rangle = 1$, which leads to

$$\langle^3\Pi|\ell_1^z s_1^z+\ell_2^z s_2^z|^1\Pi\rangle = s_2^z - s_1^z \quad \text{(C.3)}$$

$$. \quad \text{(C.4)}$$

As described in Sec. 3.2,

$$\langle \chi_e(S=1, S_z=0) | s_2^z - s_1^z | \chi_e(S=0) \rangle = 1 \tag{C.5}$$

hence, the spin-orbit coupling mixes the electron singlet and triplet states.

References

[1] A. Farkas, Orthohydrogen, Parahydrogen, and Heavy Hydrogen, Cambridge University Press, Cambridge, 1935.

[2] G. B. Field, W. B. Somerville, K. Dressler, Annu. Rev. Astro. Astrophys. 4 (1966) 207.

[3] I. F. Silvera, Rev. Mod. Phys. 52 (1980) 39.

[4] D. M. Dennison, Proc. Roy. Soc. (London) 115 (1927) 483.

[5] F. Hund, Z. Phys. 40 (1927) 93.

[6] W. Heisenberg, Z. Phys. 41 (1927) 239.

[7] T. Hori, Z. Phys. 44 (1929) 834.

[8] K. F. Bonhoeffer, P. Harteck, Naturewiss. 17 (1929) 182.

[9] A. H. Larsen, F. E. Simon, C. A. Swenson, Rev. Sci. Instr. 19 (1948) 266.

[10] E. Ilisca, Prog. Surf. Sci. 41 (1992) 217.

[11] Y. L. Sandler, J. Phys. Chem. 58 (1954) 58.

[12] Y. L. Sandler, J. Chem. Phys. 29 (1958) 97.

[13] C. M. Cunningham, D. S. Chapin, H. L. Johnston, J. Am. Chem. Soc. 80 (1958) 2382.

[14] Y. Ishii, Prog. Surf. Sci. 21 (1986) 163.

[15] E. Ilisca, S. Paris, Phys. Rev. Lett. 82 (1999) 1788.

[16] S. Paris, E. Ilisca, J. Phys. Chem. A 103 (1999) 4964.

[17] P. Avouris, D. Schmeisser, J. E. Demuth, Phys. Rev. Lett. 48 (1982) 199.

[18] S. Andersson, J. Harris, Phys. Rev. Lett. 48 (1982) 545.

[19] R. Palmer, R. Willis, Surf. Sci. 179 (1987) L1.

[20] M. Sakurai, T. Okano, Y. Tuzi, Appl. Surf. Sci. 33/34 (1988) 245.

[21] S. Yucel, Phys. Rev. B 39 (1989) 3104.

[22] E. Ilisca, J. Phys. I France 1 (1991) 1785.

[23] H. Kasai, W. Diño, R. Muhida, Prog. Surf. Sci. 72 (2003) 53.

[24] T. Magome, K. Fukutani, T. Okano, Shinku 42 (1999) 286.

[25] K. Fukutani, K. Yoshida, M. Wilde, W. Diño, M. Matsumoto, T. Okano, Phys. Rev. Lett. 90 (2003) 096103.

[26] L. Amiaud, A. Momeni, F. Dulieu, J.-H. Fillion, E. Matar, J. L. Lemaire, Phys. Rev. Lett. 100 (2008) 056101.

[27] F. Combes, G. P. des Forêts (Eds.), Molecular hydrogen in space, Cambridge University Press, 2000.

[28] E. Habart, M. Walmsleya, L. Verstraete, S. Cazaus, R. Maiolino, P. Cox, , F. Boulanger, G. P. des Forêts, Space Sci. Rev. 119 (2005) 71.

[29] J. L. Bourlot, Astron. Astrophys. 360 (2000) 656.

[30] W. F. Thi, Nature 409 (2001) 60.

[31] T. Fouchet, E. Lellouch, H. Feuchtgruber, Icarus 161 (2003) 127.

[32] L. Fletcher, P. Irwin, N. Teanby, G. Orton, P. Parrish, R. de Koka, C. Howett, S. Calcutt, N. Bowles, F. Taylor, Icarus 189 (2007) 457.

[33] T. Sugimoto, K. Fukutani, Nature Phys. 7 (2011) 307.

[34] T. E. Sharp, At. Data 2 (1971) 119.

[35] L. Wolniewicz, K. Dressler, J. Chem. Phys. 82 (1985) 3292.

[36] L. Wolniewicz, K. Dressler, J. Chem. Phys. 88 (1988) 3861.

[37] K. Niki, M. Fujiwara, Y. Motoshima, T. Kawauchi, K. Fukutani, Chem. Phys. Lett. 504 (2011) 136.

[38] G. Herzberg, Molecular spectra and molecular structure, I. Spectra of diatomic molecules, 2nd ed., Krieger, Florida, 1950.

[39] K. P. Huber, G. Herzberg, Molecular spectra and molecular structure, IV. Constants of Diatomic Molecules, Van Nostrand Reinhold, New York, 1979.

[40] K. Christmann, Surf. Sci. Rep. 9 (1988) 1.

[41] G. Vidali, G. Ihm, H.-Y. Kim, M. W. Cole, Surf. Sci. Rep. 12 (1991) 133.

[42] Y. G. Ptushinskii, Low Temp. Phys. 30 (1991) 1.

[43] L. W. Bruch, R. D. Diehl, J. A. Venables, Rev. Mod. Phys. 79 (2007) 1381.

[44] K. Svensson, S. Andersson, Phys. Rev. Lett. 78 (1997) 2016.

[45] P. Nordlander, C. Holmberg, J. Harris, Surf. Sci. 152 (1985) 702.

[46] P. Nordlander, C. Holmberg, J. Harris, Surf. Sci. 175 (1986) L753.

[47] H. Hoinkes, Rev. Mod. Phys. 52 (1980) 933.

[48] J. Perreau, J. Lapujoulade, Surf. Sci. 122 (1982) 341.

[49] C.-F. Yu, K. B. Whaley, C. S. Hogg, S. J. Sibener, Phys. Rev. Lett. 51 (1983) 2210.

[50] C.-F. Yu, K. B. Whaley, C. S. Hogg, S. J. Sibener, J. Chem. Phys. 83 (1985) 4217.

[51] U. Harten, J. P. Toennies, C. Woll, J. Chem. Phys. 85 (1986) 2249.

[52] S. Andersson, L. Wilzen, Phys. Rev. B 38 (1988) 2967.

[53] S. Andersson, L. Wilzen, M. Persson, J. Harris, Phys. Rev. B 40 (1989) 8146.

[54] S. Andersson, M. Persson, Phys. Rev. B 48 (1993) 5685.

[55] L. Amiaud, J.-H. Fillion, S. Baouche, F. Dulieu, A. Momeni, J. L. Lemaire, J. Chem. Phys. 124 (2006) 094702.

[56] L. Amiaud, F. Dulieu, J.-H. Fillion, A. Momeni, J. L. Lemaire, J. Chem. Phys. 127 (2007) 144709.

[57] S. Iwata, Y. Sato, K. Nakai, S. Ogura, T. Okano, M. Namura, A. Kasuya, K. Tohji, K. Fukutani, J. Phys. Chem. C 111 (2007) 14937.

[58] A.-S. Mårtensson, C. Nyberg, S. Andersson, Phys. Rev. Lett. 57 (1986) 2045.

[59] K. Svensson, L. Bengtsson, J. Bellman, M. Hassel, M. Persson, S. Andersson, Phys. Rev. Lett. 83 (1999) 124.

[60] L. Bengtsson, K. Svensson, M. Hassel, J. Bellman, M. Persson, S. Andersson, Phys. Rev. B 61 (2000) 16921.

[61] P. K. Schmidt, K. Christmann, G. Kresse, J. Hafner, M. Lischka, A. Groß, Phys. Rev. Lett. 87 (2001) 096103.

[62] J. Wang, C. Y. Fan, Q. Sun, K. Reuter, K. Jacobi, M. Scheffler, G. Ertl, Ang. Chem. Int. Ed. 42 (2003) 2151.

[63] K. Svensson, J. Bellman, A. Hellman, S. Andersson, Phys. Rev. B 71 (2005) 245402.

[64] J. Bellman, K. Svensson, S. Andersson, J. Chem. Phys. 125 (2006) 064704.

[65] L. Kong, G. Román-Pérez, J. M. Soler, D. C. Langreth, Phys. Rev. Lett. 103 (2009) 096103.

[66] K. Lee, A. K. Kelkkanen, K. Berland, S. Andersson, D. Langreth, E. Schroder, B. I. Lundqvist, P. Hyldgaard, Phys. Rev. B 84 (2011) 193408.

[67] J. Harris, P. Feibelman, Surf. Sci. 115 (1982) L133.

[68] R. Zare, Angular Momentum, Wiley, New York, 1988.

[69] D. White, E. N. Lasserttre, J. Chem. Phys. 32 (1960) 72.

[70] M. Chiesa, L. Mattera, R. Musenich, C. Salvo, Surf. Sci. 151 (1985) L145.

[71] R. Schinke, V. Engel, H. Voges, Chem. Phys. Lett. 104 (1984) 279.

[72] L. Wilzen, F. Althoff, S. Andersson, M. Persson, Phys. Rev. B 43 (1991) 7003.

[73] K. Svensson, S. Andersson, Surf. Sci. 392 (1997) L40.

[74] G. Cilpa, G. Chambaud, Surf. Sci. 601 (2007) 320.

[75] G. Cilpa, M. Guitou, G. Chambaud, Surf. Sci. 602 (2008) 2894.

[76] I. F. Silvera, M. Nielsen, Phys. Rev. Lett. 37 (1976) 1275.

[77] A. J. Ramirez-Cuesta, P. C. H. Mitchell, Catal. Today 120 (2007) 368.

[78] J. Z. Larese, T. Arnold, L. Frazier, R. J. Hinde, A. J. Ramirez-Cuesta, Phys. Rev. Lett. 101 (2008) 165302.

[79] F. G. Brickwedde, R. B. Scott, H. S. Taylor, J. Phys. Chem. 3 (1935) 653.

[80] A. van Itterbeek, R. Hellemans, W. van Dael, Physica 30 (1964) 324.

[81] H. Imao, K. Ishida, N. Kawamura, T. Matsuzaki, Y. Matsuda, A. Toyoda, P. Strasser, M. Iwasaki, K. Nagamine, Rev. Sci. Instrum. 79 (2008) 053502.

[82] A. A. Evett, J. Chem. Phys. 31 (1959) 565.

[83] A. A. Evett, J. Chem. Phys. 33 (1960) 789.

[84] A. Katorski, D. White, J. Chem. Phys. 40 (1964) 3183.

[85] W. R. Moore, H. R. Ward, J. Am. Chem. Soc. 80 (1958) 2909.

[86] P. L. Gant, K. Yang, Science 129 (1958) 1548.

[87] W. J. Haubach, C. M. Knobler, A. Katorski, D. White, J. Phys. Chem. 71 (1967) 1398.

[88] J. King, S. W. Benson, J. Chem. Phys. 44 (1966) 1007.

[89] E. M. Mortensen, H. Eyring, J. Phys. Chem. 64 (1960) 433.

[90] T. B. MacRury, J. R. Sams, Mol. Phys. 19 (1970) 337.

[91] T. B. MacRury, J. R. Sams, Mol. Phys. 19 (1970) 353.

[92] T. B. MacRury, J. R. Sams, Mol. Phys. 20 (1971) 57.

[93] E. L. Pace, A. R. Siebert, J. Phys. Chem. 63 (1959) 1398.

[94] J. Heidberg, N. Gushanskaya, O. Schonekas, R. Schwarte, Surf. Sci. 331-333 (1995) 1473.

[95] T. Sugimoto, K. Fukutani, in preparation.

[96] T. Sugimoto, K. Fukutani, submitted 00 (2012) 00.

[97] A. Schutte, D. Bassi, F. Tommasini, A. Turelli, J. Chem. Phys. 64 (1976) 4135.

[98] J. C. Tully, Annu. Rev. Phys. Chem. 51 (2000) 153.

[99] S. Andersson, J. Harris, Phys. Rev. B 27 (1983) 9.

[100] S. Andersson, L. Wilzen, J. Harris, Phys. Rev. Lett. 55 (1985) 2591.

[101] S. Andersson, L. Wilzen, J. Harris, Phys. Rev. Lett. 57 (1986) 1603.

[102] G. Armand, J. R. Manson, Phys. Rev. B 43 (1991) 14371.

[103] A. E. DePristo, C.-Y. LEE, J. M. Hutson, Surf. Sci. 169 (1986) 451.

[104] M. D. Stiles, J. W. Wilkins, Phys. Rev. Lett. 54 (1985) 595.

[105] B. Gumhalter, Phys. Rep. 351 (2001) 1.

[106] A. Sanz, S. Miret-Artés, Phys. Rep. 451 (2007) 37.

[107] R. F. C. Jr., J. V. V. Kasper, K. S. Pitzer, J. Chem. Phys. 46 (1967) 3220.

[108] P. L. Chapovsky, L. J. F. Hermans, Annu. Rev. Phys. Chem. 50 (1999) 315.

[109] P. L. Chapovsky, Phys. Rev. A 43 (1999) 3624.

[110] Z.-D. Sun, K. Takagi, F. Matsushima, Science 310 (2005) 1938.

[111] C. Bechtela, E. Eliasb, B. F. Schramm, J. Mol. Struct. 741 (2005) 97.

[112] Y. Miyamoto, M. Fushitani, D. Ando, T. Momose, J. Chem. Phys. 128 (2008) 114502.

[113] K. Tanaka, M. Hayashi, M. Ohtsuki, K. Harada, T. Tanaka, J. Chem. Phys. 131 (2009) 111101.

[114] P. Cacciani, J. Cosleou, M. Khelkhal, Phys. Rev. A 85 (2012) 012521.

[115] K. F. Bonhoeffer, P. Harteck, Z. Phys. Chem. B 4 (1929) 113.

[116] D. E. Osterbrock, Astrophys. J. 136 (1962) 359.

[117] H. A. Bethe, E. E. Salpeter, Quantum Mechanics of One- and Two-Electron Atoms, Dover, New York, 2008.

[118] J. C. Raich, J. R. H. Good, Astrophys. J. 139 (1964) 1004.

[119] S. Dodelson, J. Phys. B 19 (1986) 2871.

[120] Y. Sun, A. Dalgarno, Astrophys. J. 427 (1994) 1053.

[121] K. Pachucki, J. Komasa, Phys. Rev. A 77 (2008) 030501(R).

[122] D. L. Huestis, Planetary and Space Science 56 (2008) 1733.

[123] D. G. Truhlar, R. E. Wyatt, Ann. Rev. Phys. Chem. 27 (1976) 1.

[124] A. Dalgarno, J. H. Black, J. C. Weisheit, Astrophys. J. 14 (1973) L77.

[125] F. C. Fehsenfeld, D. B. Dunkin, E. E. Ferguson, D. L. Albritton, Astrophys. J. 183 (1973) L25.

[126] D. Smith, N. G. Adams, E. Alge, Astrophys. J. 263 (1982) 123.

[127] D. Gerlich, J. Chem. Phys. 92 (1990) 2377.

[128] P. Honvault, M. Jorfi, T. González-Lezana, A. Faure, L. Pagani, Phys. Rev. Lett. 107 (2011) 023201.

[129] P. Honvault, M. Jorfi, T. González-Lezana, A. Faure, L. Pagani, Phys. Chem. Chem. Phys. 13 (2011) 19089.

[130] D. R. Flower, G. P. des Forêts, C. M. Walmsley, Astron. Astrophys. 449 (2006) 621.

[131] A. I. Boothroyd, P. G. Martin, W. J. Keogh, M. J. Peterson, J. Chem. Phys. 116 (2002) 666.

[132] K. G. Petzinger, D. J. Scalapino, Phys. Rev. B 8 (1973) 266.

[133] K. Makoshi, M. Rami, E. Ilisca, J. Phys. Condens. Matter 5 (1993) 7325.

[134] M. Rami, K. Makoshi, E. Ilisca, Surf. Sci. 68 (1993) 197.

[135] E. Ilisca, Chem. Phys. Lett. 168 (1990) 289.

[136] L. D. Landau, E. M. Lifshitz, Quantum Mechanics- Nonrelativistic Theory, 2nd Edition, Pergamon, Oxford, 1965.

[137] M. Hamermesh, Phys. Rev. 73 (1948) 638.

[138] Y. L. Sandler, J. Chem. Phys. 20 (1952) 1050.

[139] K. Motizuki, J. Phys. Soc. Jpn. 12 (1957) 163.

[140] E. Wigner, Z. Phys. Chem. B 23 (1933) 28.

[141] L. G. Harrison, C. A. McDowell, Proc. Roy. Soc. A 220 (1953) 77.

[142] A. J. Leffler, J. Chem. Phys. 43 (1965) 4410.

[143] In ref. [142], it is pointed out that the indistinguishability principle of identical particles might be broken under spatially inhomogeneous potential. As stated in Sec. 2.2, however, the rotational motion is modified in an inisotropic potential with the eigen state described by linear combination of other rotational states, and the symmetry of the rotational wavefunction is strictly maintained with respect to the particle exchange.

[144] C. F. Ng, Surf. Sci. 79 (1979) 470.

[145] E. Ilisca, Phys. Rev. Lett. 24 (1970) 797.

[146] E. Ilisca, A. P. Legrand, Phys. Rev. B 5 (1972) 4994.

[147] Y. Ishii, S. Sugano, Surf. Sci. 127 (1983) 21.

[148] Y. Ishii, S. Sugano, J. Phys. C. Solid State Phys. 17 (1984) 2094.

[149] K. Motizuki, T. Nagamiya, J. Phys. Soc. Jpn. 11 (1956) 93.

[150] F. Schmidt, Phys. Rev. B 10 (1974) 4480.

[151] Y. Y. Milenko, R. M. Sibileva, Sov. J. Low Temp. Phys. 1 (1975) 382.

[152] A. Honig, M. Lewis, Z.-Z. Yu, S. Yucel, Phys. Rev. Lett. 56 (1986) 1866.

[153] P. Pedroni, H. Meyer, F. Weinhaus, D. Haase, Solid State Commun. 14 (1974) 279.

[154] A. Driessen, E. van der Poll, I. F. Silvera, Phys. Rev. B 30 (1984) 2517.

[155] M. G. Pravica, I. F. Silvera, Phys. Rev. Lett. 81 (1998) 4180.

[156] M. A. Strzhemechny, R. J. Hemley, Phys. Rev. Lett. 85 (2000) 05595.

[157] M. A. Strzhemechny, R. J. Hemley, H. k. Mao, A. F. Goncharov, J. H. Eggert, Phys. Rev. B 66 (2002) 014103.

[158] A. J. Berlinsky, W. N. Hardy, Phys. Rev. B 8 (1973) 5013.

[159] Y. Li, X. Lei, R. G. Lawler, Y. Murata, K. Komatsu, N. J. Turro, J. Phys. Chem. Lett. 2 (2011) 741.

[160] E. Ilisca, S. Sugano, Phys. Rev. Lett. 57 (1986) 2590.

[161] E. Ilisca, S. Paris, Surf. Sci. 363 (1996) 347.

[162] E. Ilisca, Phys. Rev. Lett. 66 (1991) 667.

[163] E. Ilisca, Surf. Sci. 242 (19916) 470.

[164] E. Ilisca, Opt. Commun. 89 (1992) 399.

[165] R. Muhida, H. Setiyanto, M. M. Rahman, W. Diño, H. Nakanishi, H. Kasai, K. Fukutani, T. Okano, Eur. Phys. J. D 38 (2006) 99.

[166] R. Muhida, M. David, M. M. Rahman, W. Diño, H. Nakanishi, H. Kasai, K. Fukutani, T. Okano, Eur. Phys. J. D 38 (2006) 99.

[167] R. Muhida, W. Diño, A. Fukui, H. Kasai, H. Nakanishi, A. Okiji, K. Fukutani, T. Okano, Surf. Sci. 493 (2001) 285.

[168] R. Muhida, W. Diño, A. Fukui, H. Kasai, H. Nakanishi, A. Okiji, K. Fukutani, T. Okano, J. Phys. Soc. Jpn. 70 (2001) 3654.

[169] R. Muhida, W. Diño, Y. Miura, H. Kasai, H. Nakanishi, A. Okiji, K. Fukutani, T. Okano, Surf. Sci. 514 (2002) 273.

[170] R. Muhida, W. Diño, Y. Miura, H. Kasai, H. Nakanishi, K. Fukutani, T. Okano, A. Okiji, J. Vac. Soc. Jpn. 45 (2002) 448.

[171] R. Muhida, Y. Miura, W. Diño, H. Kasai, H. Nakanishi, A. Okiji, K. Fukutani, T. Okano, J. Appl. Phys. 93 (2003) 644.

[172] Y. Kunisada, H. Kasai, J. Phys. Soc. Jpn. 82 (2013) 023601.

[173] Y. Kunisada, H. Nakanishi, W. A. Diño, H. Kasai, J. Vac. Soc. Jpn. 55 (2012) 115.

[174] E. Ilisca, S. Sugano, Chem. Phys. Lett. 149 (1988) 20.

[175] L. Wolniewicz, J. Mol. Spec. 169 (1995) 329.

[176] W. Kolos, J. Rychlewski, Comp. Methods Sci. Technol. 5 (1999) 39.

[177] A. Abragam, The principles of nuclear magnetism, Oxford University Press, Oxford, 1961.

[178] A. B. Harris, Phys. Rev. B 2 (1970) 3495.

[179] N. S. Sullivan, R. V. Pound, Phys. Rev. A 6 (1972) 1102.

[180] E. R. Grilly, Rev. Sci. Instrum. 24 (1952) 72.

[181] T. W. Bradshaw, J. O. W. Norris, Rev. Sci. Instrum. 58 (1986) 83.

[182] M. Nielsen, Phys. Rev. B 7 (1973) 1626.

[183] D. W. Brown, P. E. Sokol, S. A. FitzGerald, Phys. Rev. B 59 (1999) 13258.

[184] S. A. FitzGerald, T. Yildirim, L. J. Santodonato, D. A. Neumann, J. R. D. Copley, J. J. Rush, F. Trouw, Chem. Phys. Lett. 329 (2000) 311.

[185] C. M. Brown, T. Yildirim, D. A. Neumann, M. J. Heben, T. Gennett, A. C. Dillon, J. L. Alleman, J. E. Fischer, Chem. Phys. Lett. 329 (2000) 311.

[186] A. J. Horsewill, K. S. Panesar, S. Rols, M. R. Johnson, Y. Murata, K. Komatsu, S. Mamone, A. Danquigny, F. Cuda, S. Maltsev, M. C. Grossel, M. Carravetta, M. H. Levitt, Phys. Rev. Lett. 102 (2009) 013001.

[187] K. Sumida, S. Horike, S. S. Kaye, Z. R. Herm, W. L. Queen, C. M. Brown, F. Grandjean, G. J. Long, A. Dailly, J. R. Long, Chem. Sci. 1 (2010) 184.

[188] M. Hiller, E. V. Lavrov, J. Weber, Phys. Rev. Lett. 98 (2007) 055504.

[189] M. Hiller, E. V. Lavrov, J. Weber, Phys. Rev. B 80 (2009) 045306.

[190] V. Plotnichenko, S. Vasiliev, A. Rybaltovskii, V. Koltashev, V. Sokolov, S. Klyamkin, O. Medvedkov, A. Rybaltovskii, A. Malosiev, E. Dianov, J. Non-Cryst. Solids 351 (2005) 3677.

[191] K. A. Williams, B. K. Pradhan, P. C. Eklund, M. K. Kostov, M. W. Cole, Phys. Rev. Lett. 88 (2002) 165502.

[192] A. Centrone, L. Brambilla, G. Zerbi, Phys. Rev. B 71 (2005) 245406.

[193] A. Centrone, J. Raman Spectrosc. 42 (2011) 2165.

[194] G. J. Schulz, Rev. Mod. Phys. 45 (1973) 423.

[195] J. E. Demuth, D. Schmeisser, P. Avouris, Phys. Rev. Lett. 47 (1981) 1166.

[196] M. Folman, Y. Kozirovski, J. Colloid Int. Sci. 38 (1972) 51.

[197] T. E. Huber, C. A. Huber, Phys. Rev. Lett. 59 (1987) 1120.

[198] H. G. Hixson, M. J. Wojcik, M. S. Devlin, J. P. Devlin, V. Buch, J. Chem. Phys. 97 (1992) 753.

[199] V. Buch, J. P. Devlin, J. Chem. Phys. 98 (1993) 4195.

[200] S. A. FitzGerald, S. Forth, M. Rinkoski, Phys. Rev. B 65 (2002) 140302.

[201] S. A. FitzGerald, H. O. H. Churchill, P. M. Korngut, C. B. Simmons, Y. E. Strangas, Phys. Rev. B 73 (2006) 155409.

[202] S. Mamone, M. Ge, D. Hüvonen, U. Nagel, A. Danquigny, F. Cuda, M. C. Grossel, Y. Murata, K. Komatsu, M. Levitt, T. Rõõm, M. Carravetta, J. Chem. Phys. 130 (2009) 081103.

[203] C. Peng, M. Stavola, W. B. Fowler, M. Lockwood, Phys. Rev. B 80 (2009) 125207.

[204] S. A. FitzGerald, J. Hopkins, B. Burkholder, M. Friedman, Phys. Rev. B 81 (2010) 104305.

[205] S. A. FitzGerald, B. Burkholder, M. Friedman, J. B. Hopkins, C. J. Pierce, J. M. Schloss, B. Thompson, J. L. C. Rowsell, J. Am. Chem. Soc. 133 (2011) 20310.

[206] L. Kong, Y. J. Chabal, D. C. Langreth, Phys. Rev. B 83 (2011) 121402.

[207] G. Ricchiardi, J. G. Vitillo, D. Cocina, E. N. Gribovc, A. Zecchinaa, Phys. Chem. Chem. Phys. 9 (2007) 2753.

[208] M. Grunwald, G. E. Ewing, J. Chem. Phys. 109 (1998) 4990.

[209] J. Heidberg, A. Vosberg, M. Hustedt, M. Thomas, J. Chem. Phys. 110 (1999) 2566.

[210] E. Marinero, C. Rettner, R. Zare, Phys. Rev. Lett. 48 (1982) 1323.

[211] E. Marinero, R. Vasudev, R. Zare, J. Chem. Phys. 78 (1983) 692.

[212] K.-D. Rinnen, M. Buntine, D. Kliner, J. Chem. Phys. 95 (1991) 214.

[213] H. Rottke, K. H. Welge, Chem. Phys. Lett. 99 (1983) 456.

[214] W. Meier, H. Rottke, H. Zacharias, K. H. Welge, J. Chem. Phys. 83 (1985) 4360.

[215] F. J. Northrup, J. C. Polanyi, S. C. Wallace, J. M. Williamson, Chem. Phys. Lett. 105 (1984) 34.

[216] D. J. Kligler, C. Rhodes, Phys. Rev. Lett. 40 (1978) 309.

[217] D. Kligler, J. Bokor, C. Rhodes, Phys. Rev. A 21 (1980) 607.

[218] H. Pummer, H. Egger, T. Luk, T. Srinivasan, C. Rhodes, Phys. Rev. A 28 (1983) 795.

[219] Q. Wang, T. Sugimoto, K. Fukutani, Seisankenkyu 64 (2012) 911.

[220] H. Zacharias, Appl. Phys. A 47 (1988) 37.

[221] G. Pozgainer, L. Windholz, A. Winkler, Meas. Sci. Technol. 5 (1994) 947.

[222] J. S. A. Perry, J. M. Gingell, K. A. Newson, J. To, N. Watanabe, S. D. Price, Meas. Sci. Technol. 13 (2002) 1414.

[223] K. Fukutani, K. Niki, T. Ito, H. Tashiro, M. Matsumoto, M. Wilde, T. Okano, W. Diño, H. Kasai, Surf. Sci. 593 (2005) 229.

[224] K. Niki, T. Kawauchi, M. Matsumoto, K. Fukutani, T. Okano, Phys. Rev. B 77 (2008) 201403(R).

[225] K. Niki, S. Ogura, M. Matsumoto, T. Okano, K. Fukutani, Phys. Rev. B 79 (2009) 085408.

[226] M. Chehrouri, J.-H. Fillion, H. Chaabouni, H. Mokrane, E. Congiu, F. Dulieu, E. Matar, X. Michaut, J. Lemaire, Phys. Chem. Chem. Phys. 13 (2011) 2172.

[227] M. Fujiwara, K. Niki, T. Okano, K. Fukutani, J. Phys. Conf. Ser. 200 (2010) 022038.

[228] K. Svensson, S. Andersson, Phys. Rev. Lett. 98 (2007) 096105.

[229] A. J. Berlinsky, Phys. Rev. B 26 (1982) 443.

[230] C. Benvenuti, R. S. Calder, G. Passardi, J. Vac. Sci. Technol. 13 (1976) 1172.

[231] H. Schlichting, D. Menzel, Rev. Sci. Instrum. 64 (1993) 2013.

[232] T. Sharp, At. Data 2 (1971) 119.

[233] H. B. Michaelson, J. Appl. Phys. 48 (1977) 4729.

[234] M.-C. Desjonquères, D. Spanjaard, Concepts in Surface Physics, 2nd Edition, Springer, Berlin, 1996.

[235] M. Gruyters, K. Jacobi, Chem. Phys. Lett. 225 (1994) 309.

[236] W. Wurth, J. Stöhr, P. Feulner, X. Pan, K. R. Bauchspiess, Y. Baba, E. Hudel, G. Rocker, D. Menzel, Phys. Rev. Lett. 65 (1990) 2426.

[237] T. Yokoyama, D. Arvanitis, T. Lederer, M. Tischer, L. Tröger, K. Baberschke, G. Comelli, Phys. Rev. B 48 (1993) 15405.

[238] Y. Jiang, Y. N. Zhang, J. X. Cao, R. Q. Wu, W. Ho, Science 333 (2011) 324.

[239] F. Besenbacher, J. K. Nørskov, Prog. Surf. Sci. 44 (1993) 5.

[240] Y. Kazama, M. Matsumoto, T. Sugimoto, T. Okano, K. Fukutani, Phys. Rev. B 84 (2011) 064128.

[241] Y. Kunisada, H. Nakanishi, H. Kasai, J. Phys. Soc. Jpn. 80 (2011) 084605.

[242] M. Kurahashi, X. Sun, Y. Yamauchi, Phys. Rev. B 86 (2012) 245421.

[243] Y. Kunisada, M. C. Escaño, H. Kasai, J. Phys.: Condens. Matter 23 (2011) 394207.

[244] K. Motizuki, T. Nagamiya, J. Phys. Soc. Jpn. 11 (1956) 654.

[245] V. Shevtsov, A. Scherbakov, P. Malmi, E. Ylinen, M. Punkkinen, J. Low Temp. Phys. 104 (1996) 211.

[246] V. Shevtsov, P. Malmi, E. Ylinen, M. Punkkinen, J. Low Temp. Phys. 114 (1999) 431.

[247] V. Shevtsov, E. Ylinen, P. Malmi, M. Punkkinen, Phys. Rev. B 62 (2000) 12386.

[248] Y. Kunisada, H. Nakanishi, W. A. Diño, H. Kasai, Curr. Appl. Phys. 12 (2012) S115.

[249] P. R. Kubik, W. N. Hardy, H. Glattli, Can. J. Phys. 63 (1985) 605.

[250] H. Freimuth, H. Wiechert, Surf. Sci. 162 (1985) 432.

[251] H. Freimuth, H. Wiechert, Surf. Sci. 178 (1985) 716.

[252] S. Yucel, N. Alexander, A. Honig, Phys. Rev. B 42 (1990) 820.

[253] M. Fujita, K. Wakabayashi, K. Nakada, K. Kusakabe, J. Phys. Soc. Jpn. 65 (1996) 1920.

[254] e.g. J. Červenka, M. I. Katsnelson, C. F. J. Flipse, Nat. Phys. 5 (2009) 840.

[255] A. K. Geim, K. S. Novoselov, Nature Mater. 6 (2007) 183.

[256] Y. L. Sandler, J. Phys. Chem. 58 (1953) 54.

[257] N. Watanabe, Y. Kimura, A. Kouchi, T. Chigai, T. Hama, V. Pirronello, Astrophys. J. Lett. 714 (2010) 233.

[258] H. Mokrane, H. Chaabouni, M. Accolla, E. Congiu, F. Dulieu, M. Chehrouri, J. L. Lemaire, Astrophys. J. 705 (2009) L195.

[259] D. J. Adams, Nature 293 (1981) 447.

[260] E. R. Batista, S. S. Xantheas, H. Jonsson, J. Chem. Phys. 109 (1998) 4546.

[261] C. Toubin, S. Picaud, C. Girardet, Chem. Phys. 244 (1999) 227.

[262] C. Girardet, C. Toubin, Surf. Sci. Rep. 44 (2001) 159.

[263] T. Sugimoto, K. Fukutani, in preparation.

[264] L. Senadheera, M. S. Conradi, J. Phys. Chem. A 112 (2008) 8303.

[265] A. Giannasi, M. Celli, L. Ulivi, M. Zoppi, J. Chem. Phys. 129 (2008) 084705.

[266] M. Hiller, E. V. Lavrov, J. Weber, Phys. Rev. Lett. 99 (2007) 209901.

[267] S. A. FitzGerald, K. Allen, P. Landerman, J. Hopkins, J. Matters, R. Myers, Phys. Rev. B 77 (2008) 224301.

[268] J.-H. Fillion, L. Amiaud, E. Congiu, F. Dulieu, A. Momeni, J. L. Lemaire, Phys. Chem. Chem. Phys. 11 (2009) 4396.

[269] E. Habart, A. Abergel, F. Boulanger, C. Joblin, L. Verstraete, M. Compiègne, G. P. des Forêts, J. L. Bourlot, Astron. Astrophys. 527 (2011) A122.

[270] J. Takahashi, Astrophys. J. 561 (2001) 254.

[271] J. H. Black, E. F. van Dishoeck, Astrophys. J. 322 (1987) 412.

[272] C. G. Gray, Can. J. Phys. 46 (1968) 135.

[273] T. Hasegawa, I. Gatley, R. P. Garden, P. W. J. Brand, M. Ohishi, M. Hayashi, N. Kaifu, Astrophys. J. 318 (1987) L77.

[274] M. Tanaka, T. Hasegawa, S. S. Hayashi, P. W. J. L. Brand, I. Gatley, Astrophys. J. 336 (1989) 207.

[275] M. Tanaka, T. Hasegawa, I. Gatley, Astrophys. J. 374 (1991) 516.

[276] M. D. Smith, C. J. Davis, A. Lioure, Astron. Astrophys. 327 (1997) 1206.

[277] S. K. Ramsay, A. Chrysostomou, T. R. Geballe, P. W. J. L. Brand, M. Mountain, Mon. Not. R. Astr. Soc. 263 (1993) 695.

[278] J. L. Hora, W. B. Latter, Astrophys. J. 461 (1996) 288.

[279] A. Chrysostomou, P. W. J. L. Brand, M. G. Burton, A. Moorhouse, Mon. Not. R. Astr. Soc. 265 (1993) 329.

[280] D. L. Shupe, J. E. Larkin, R. A. Knop, L. Armus, K. Matthews, B. T. Soifer, Astrophys. J. 498 (1987) 267.

[281] L. E. Kristensen, T. L. Ravkilde, D. Field, J. L. Lemaire, G. P. des Forêts, Astron. Astrophys. 469 (2007) 561.

[282] J. H. Lacy, R. Knacke, T. R. Geballe, A. T. Tokunaga, Astrophys. J. 428 (1994) L69.

[283] D. A. Neufeld, G. J. Melnick, M. Harwit, Astrophys. J. 506 (1998) L75.

[284] A. Sternberg, D. A. Neufeld, Astrophys. J. 516 (1999) 371.

[285] P. S. Parmar, J. H. Lacy, J. M. Achtermann, Astrophys. J. 372 (1991) L25.

[286] K. N. Allers, D. T. Jaffe, J. H. Lacy, B. T. Draine, M. J. Richter, Astrophys. J. 630 (2005) 368.

[287] R. Timmermann, F. Bertoldi1, C. M. Wright, S. Drapatz, B. T. Draine, L.Haser, A. Sternberg, Astron. Astrophys. 315 (1996) L281.

[288] D. Rosenthal, F. Bertoldi, S. Drapatz, Astron. Astrophys. 356 (2000) 705.

[289] B. Lefloch, J. Cernicharo, S. Cabrit, A. Noriega-Crespo, A. Moro-Martín, D. Cesarsky, Astrophys. J. 590 (2003) L41.

[290] C. M. Wright, S. Drapatz, R. Timmermann, P. van der Werf, R. Katterloher, T. de Graauw, Astron. Astrophys. 315 (1996) L301.

[291] D. Cesarsky, P. Cox, G. P. des Forêts, E. F. van Dishoeck, F. Boulanger, C. M. Wright, Astron. Astrophys. 348 (1999) 945.

[292] M. Benedettini, T. Giannini, B. Nisini, E. Tommasi, D. Lorenzetti, A. D. Giorgio, P. Saraceno, H. Smith, G. White, Astron. Astrophys. 359 (2000) 148.

[293] B. Nisini, M. Benedettini, T. Giannini, C. Codella, D. Lorenzetti, A. D. Giorgio, J. Richer, Astron. Astrophys. 360 (2000) 297.

[294] S. Molinari, A. Noriega-Crespo, C. Ceccarelli, B. N. T. Giannini, D. Lorenzetti, E. Caux, , P. Saraceno, G. J. White, Astrophys. J. 538 (2000) 698.

[295] E. Habart, F. Boulanger, L. Verstraete, G. P. des Forêts, E. Falgarone, A. Abergel, Astron. Astrophys. 397 (2003) 623.

[296] A. Fuente, J. Martín-Pintado, N. Rodríguez-Fernández, A. Rodríguez-Franco, P. D. Vicente, Astrophys. J. 518 (1999) L45.

[297] N. J. Rodríguez-Fernández, J. Martín-Pintado, P. D. Vicente, A. Fuente, S. Hüttemeister, T. L. Wilson, D. Kunze, Astron. Astrophys. 356 (2000) 695.

[298] D. A. Neufeld, G. J. Melnick, P. Sonnentrucker, E. A. Bergin, J. D. Green, K. H. Kim, D. M. Watson, W. J. Forrest, J. L. Pipher, Astrophys. J. 649 (2006) 816.

[299] S. Maret, E. A. Bergin, D. A. Neufeld, J. D. Green, D. M. Watson, M. O. Harwit, L. E. Kristensen, G. J. Melnick, P. Sonnentrucker, V. Tolls, M. W. Werner, W. Michael, K. Willacy, Y. Yuan, Astrophys. J. 698 (2009) 1244.

[300] D. Neufeld, B. Nisini, T. Giannini, G. J. Melnick, E. A. Bergin, Y. Yuan, S. Maret, V. Tolls, R. Güsten, M. J. Kaufman, Astrophys. J. 706 (2009) 170.

[301] T. Giannini, B. Nisini, D. Neufeld, Y. Yuan, S. Antoniucci, A. Gusdorf, Astrophys. J. 738 (2011) 80.

[302] B. Nisini, T. Giannini, D. Neufeld, Y. Yuan, S. Antoniucci, E. A. Bergin, G. J. Melnick, Astrophys. J. 724 (2010) 69.

[303] M. Barsony, G. A. Wolf-Chase, D. R. Ciardi, J. O'Linger, Astrophys. J. 720 (2010) 64.

[304] O. Dionatos, B. Nisini, S. Cabrit, L. Kristensen, G. P. des Forêts, Astron. Astrophys. 521 (2010) A7.

[305] Y. Sheffer, M. G. Wolfire1, D. J. Hollenbach, M. J. Kaufman, M. Cordier, Astrophys. J. 741 (2011) 45.

[306] P. F. Goldsmith, T. Velusamy, D. Li, W. D. Langer, Astrophys. J. 715 (2010) 1370.

[307] R. J. Gould, E. E. Salpeter, Astrophys. J. 138 (1963) 393.

[308] D. Hollenbach, E. E. Salpeter, Astrophys. J. 163 (1971) 155.

[309] W. Lichten, Phys. Rev. 120 (1960) 848.

[310] S. Glasstone, K. J. Laidler, H. Eyring, The theory of rate processes: the kinetics of chemical reactions, viscosity, diffusion and electrochemical phenomena, McGraw-Hill, New York, 1941.

[311] A. Winkler, K. D. Rendulic, Int. Rev. Phys. Chem. 11 (1992) 101.

[312] K. Christmann, Prog. Surf. Sci. 48 (1995) 15.

[313] A. Groß, Surf. Sci. Rep. 32 (1998) 291.

[314] G.-J. Kroes, Prog. Surf. Sci. 60 (1999) 1.

[315] W. A. Dino, H. Kasai, A. Okiji, Prog. Surf. Sci. 63 (1998) 63.

[316] G.-J. Kroes, A. Gross, E.-J. Baerends, M. Scheffler, D. A. Mccormack, Acc. Chem. Res. 35 (2002) 193.

[317] D. Farías, R. Miranda, Prog. Surf. Sci. 86 (2011) 222.

[318] D. A. Williams, W. A. Brown, S. D. Price, J. M. C. Rawlings, S. Viti, Astron. Geophys. 48 (2007) 1.25.

[319] N. Watanabe, A. Kouchi, Prog. Surf. Sci. 83 (2008) 439.

[320] Y. M. Xiao, S. Buchman, L. Pollack, D. Kleppner, T. J. Greytak, J. Chem. Phys. 96 (1992) 4032.

[321] S. C. Creighan, J. S. A. Perry, S. D. Price, J. Chem. Phys. 124 (2006) 114701.

[322] F. Islam, E. R. Latimer, S. D. Price, J. Chem. Phys. 127 (2007) 064701.

[323] E. R. Latimer, F. Islam, S. D. Price, Chem. Phys. Lett. 455 (2008) 174.

[324] A. Yabushita, T. Hama, D. Iida, N. Kawanaka, M. Kawasaki, N. Watanabe, M. N. R. Ashfold, H.-P. Loock, Astrophys. J. 682 (2008) L69.

[325] A. Yabushita, T. Hama, D. Iida, N. Kawanaka, M. Kawasaki, Astrophys. J. 129 (2008) 044501.

[326] L. Gavilan, G. Vidali, J. L. Lemaire, M. Chehrouri, F. Dulieu, J.-H. Fillion, E. Congiu, H. Chaabouni, Astrophys. J. 760 (2012) 1.

[327] K. Takayanagi, K. Sakimoto, K. Onda, Astrophys. J. 318 (1987) L81.

[328] B. T. Draine, F. Bertoldi, Astrophys. J. 468 (1996) 269.

[329] T. G. Waech, R. B. Bernstein, J. Chem. Phys. 46 (1967) 4905.

[330] R. E. Roberts, R. B. Bernstein, C. F. Curtiss, J. Chem. Phys. 50 (1969) 5163.

[331] M. Menzinger, Chem. Phys. Lett. 10 (1971) 507.

[332] R. E. Roberts, J. Chem. Phys. 54 (1971) 1422.

[333] C. Schwartz, R. J. L. Roy, J. Chem. Phys. 81 (1984) 4149.

[334] S. Morisset, F. Aguillon, M. Sizun, V. Sidis, J. Chem. Phys. 121 (2004) 6493.

[335] S. Morisset, F. Aguillon, M. Sizun, V. Sidis, J. Chem. Phys. 122 (2005) 194702.

[336] B. Kerkeni, D. C. Clary, Chem. Phys. 338 (2007) 1.

[337] D. Bachellerie, M. Sizun, F. Aguillon, V. Sidis, J. Phys. Chem. A 113 (2009) 108.

[338] A. J. Farebrother, A. J. Meijer, D. C. Clary, A. J. Fisher, Chem. Phys. Lett. 319 (2000) 303.

[339] X. Sha, B. Jackson, J. Chem. Phys. 116 (2002) 7158.

[340] S. Morisset, F. Aguillon, M. Sizun, V. Sidis, J. Phys. Chem. A 105 (2004) 8571.

[341] D. Bachellerie, M. Sizun, D. Teillet-Billy, N. Rougeau, V. Sidis, Chem. Phys. Lett. 448 (2007) 223.

[342] M. Bonfanti, S. Casolo, G. F. Tantardini, R. Martinazzo, Phys. Chem. Chem. Phys. 13 (2011) 16680.

[343] N. Rougeau, D. Teillet-Billy, V. Sidis, Phys. Chem. Chem. Phys. 13 (2011) 17579.

[344] R. Martinazzo, G. F. Tantardini, J. Chem. Phys. 124 (2006) 124702.

[345] A. J. H. M. Meijer, A. J. Farebrother, D. C. Clary, A. J. Fisher, J. Phys. Chem. A 105 (2001) 2173.

[346] J. Ree, Y. Kim, H. Shin, Chem. Phys. Lett. 353 (2002) 368.

[347] A. J. H. M. Meijer, A. J. Farebrother, D. C. Clary, J. Phys. Chem. A 106 (2002) 8996.

[348] A. J. H. M. Meijer, A. J. Fisher, D. C. Clary, J. Phys. Chem. A 107 (2003) 10862.

[349] R. Martinazzo, G. F. Tantardini, J. Phys. Chem. A 109 (2005) 9379.

[350] R. Martinazzo, G. F. Tantardini, J. Chem. Phys. 124 (2006) 124703.

[351] H. M. Cuppen, L. Hornekar, J. Chem. Phys. 128 (2008) 174707.

[352] S. Casolo, R. Martinazzo, M. Bonfanti, G. F. Tantardini, J. Phys. Chem. A 113 (2009) 14545.

[353] M. Sizun, D. Bachellerie, F. Aguillon, V. Sidis, Chem. Phys. Lett. 498 (2010) 32.

[354] D. R. Flower, G. D. Watt, Mon. Not. R. Astr. Soc. 209 (1984) 25.

[355] D. R. Flower, G. P. des Forêts, Mon. Not. R. Astr. Soc. 316 (2000) 901.

[356] S. C. O. Glover, T. Abel, Mon. Not. R. Astr. Soc. 388 (2008) 1627.

[357] L. Pagani, C. Vastel, E. Hugo, V. Kokoouline, C. H. Greene, A. Bacmann, E. Bayet, C. Ceccarelli, R. Peng, S. Schlemmer, Astron. Astrophys. 494 (2009) 623.